Titre: Title:	Automated Analysis of Retinal and Choroidal OCT and OCTA Images in AMD
Auteur: Author:	Charles Bélanger Nzakimuena
Date:	2020
Type:	Mémoire ou thèse / Dissertation or Thesis
Référence: Citation:	Bélanger Nzakimuena, C. (2020). Automated Analysis of Retinal and Choroidal OCT and OCTA Images in AMD [Mémoire de maîtrise, Polytechnique Montréal]. PolyPublie. https://publications.polymtl.ca/5234/

Document en libre accès dans PolyPublie
Open Access document in PolyPublie

URL de PolyPublie: PolyPublie URL:	https://publications.polymtl.ca/5234/
Directeurs de recherche: Advisors:	Farida Cheriet, & Santiago Costantino
Programme: Program:	Génie biomédical

POLYTECHNIQUE MONTRÉAL

affiliée à l'Université de Montréal

Automated analysis of retinal and choroidal OCT and OCTA images in AMD

CHARLES BÉLANGER NZAKIMUENA

Institut de génie biomédical

Mémoire présenté en vue de l'obtention du diplôme de *Maîtrise ès sciences appliquées*

Génie biomédical

Avril 2020

POLYTECHNIQUE MONTRÉAL

affiliée à l'Université de Montréal

Ce mémoire intitulé :

Automated analysis of retinal and choroidal
OCT and OCTA images in AMD

présenté par **Charles BÉLANGER NZAKIMUENA**

en vue de l'obtention du diplôme de *Maîtrise ès sciences appliquées*

a été dûment accepté par le jury d'examen constitué de :

Julien COHEN-ADAD, président
Farida CHERIET, membre et directrice de recherche
Santiago COSTANTINO, membre et codirecteur de recherche
Renaud DUVAL, membre

DEDICATION

To Kari-Ann and Justin, and to my parents, Jocelyne and Jérôme.

ACKNOWLEDGEMENTS

REMERCIEMENTS

Je tiens à remercier mes directeurs de recherche, le professeur Santiago Costantino et la professeure Farida Cheriet, pour le privilège de mener un projet sous leur supervision. Je tiens également à remercier les membres et collaborateurs du laboratoire de biophotonique de l'Hôpital Maisonneuve-Rosemont, du Groupe Boutopoulos et du laboratoire LIV4D pour leur enthousiasme continu, et leurs commentaires très pertinents durant le projet de recherche.

Merci à ma famille et mes amis pour leur soutien tout au long de mes études. Je remercie le personnel de Polytechnique, et spécialement Mme. Amal Bennani pour ses conseils tout au long de mon cheminement académique. Merci aux membres de la société technique PolyCortex, aux autres étudiants de Polytechnique, de l'Université de Montréal et de l'Hôpital Maisonneuve-Rosemont pour les interactions et le grand honneur d'apprendre à leurs côtés.

RÉSUMÉ

La dégénérescence maculaire liée à l'âge (DMLA) est une maladie oculaire progressive qui se manifeste principalement au niveau de la rétine externe et de la choroïde. Le projet de recherche vise à déterminer si des mesures obtenues à partir d'images de tomographie par cohérence optique (OCT) et d'angiographie OCT (OCTA) peuvent être utilisées afin de fournir de nouvelles informations sur des biomarqueurs de la DMLA, ainsi qu'une méthode de détection précoce de la maladie. À cette fin, un appareil permettant l'OCT et l'OCTA a été utilisé pour imager des sujets DMLA précoces et intermédiaires, et des sujets témoins. À la configuration sélectionnée de l'appareil OCT, chaque acquisition d'un œil fournit un volume de données qui est constitué de 300 images transversales appelées B-scan. Au total, des acquisitions de 10 yeux de sujets atteints de DMLA précoce et intermédiaire (3000 images B-scan) et un cas de DMLA néovasculaire, 12 yeux de sujets âgés de plus de 50 ans (3600 images B-scan) et 11 yeux de sujets âgés de moins de 50 ans (3300 images B-scan) ont été obtenues. Cinq méthodes d'extraction de caractéristiques ont été reproduites ou développées afin de déterminer si des différences significatives au niveau de l'œil pouvaient être observées entre les sujets atteints de DMLA précoce et intermédiaire et les sujets témoins d'âge similaire. Grâce à des tests non paramétriques, il a été établi que deux méthodes connues d'extraction de biomarqueurs de la DMLA (analyse d'absence de signal de débit sanguin au niveau de la choriocapillaire et une méthode de segmentation des drusen) produisent des mesures qui montrent des différences significatives entre les groupes, et qui sont représentées de façon uniforme à travers le plan frontal de l'œil. Il a ensuite été souhaité de tirer parti des mesures et de générer un modèle de classification de la DMLA interprétable basé sur l'apprentissage automatique au niveau des B-scans. Des spectres de fréquence résultant de la transformé de Fourier rapide de séries spatiales dérivées de mesures considérées comme représentatives des deux biomarqueurs ont été obtenues, et utilisées comme caractéristiques pour former un classifieur de type forêt aléatoire et un classifieur de type forêt profonde. L'analyse en composantes principales (PCA) a été utilisée pour réduire la dimensionnalité de l'espace des caractéristiques, et la performance des modèles et l'importance des prédicteurs ont été évaluées. Une nouvelle méthode a été conçue qui permet une reconstruction 3D automatisée et une évaluation quantitative de la structure des signaux OCTA et ainsi des vaisseaux rétiniens. Des mesures représentatives des drusen et de la choriocapillaire ont été utilisées pour créer des modèles interprétables pour la classification de la DMLA précoce et intermédiaire. Alors que la prévalence mondiale de la DMLA

augmente et que les appareils OCT deviennent plus disponibles, un plus grand nombre de personnes hautement qualifiées est nécessaire pour interpréter les informations médicales et fournir les soins cliniques appropriés. L'analyse et le classement du niveau de sévérité de la DMLA par des experts par le biais d'images OCT sont coûteux et prennent du temps. Les modèles proposés pourraient servir à automatiser la détection de la DMLA, même lorsqu'elle est asymptomatique, et signaler à un ophtalmologue la nécessité de surveiller et de traiter la condition avant la survenue de pertes graves de la vision. Les modèles sont transparents et sont en mesure de fournir une classification à partir d'une seule image transversale. Par conséquent, l'outil diagnostic automatisé pourrait également être utilisé dans des situations où seules des données médicales partielles sont disponibles ou lorsque l'accès aux ressources de soins de santé est limité.

ABSTRACT

Age-related macular degeneration (AMD) is a progressive eye disease which manifests primarily at the outer retina and choroid. The research project aimed to determine whether measures obtained from optical coherence tomography (OCT) and OCT angiography (OCTA) images could be used to provide novel AMD biomarker insight and an early disease detection method. To that end, an OCT and OCTA enabled device was used to image AMD subjects and controls. At the selected device scan size, each scan of one eye gathered using an OCT device provides a volume of data which is constructed of 300 cross-sectional images termed B-scans. In total, scans of 10 eyes from subjects with early and intermediate AMD (3,000 B-scan images) and a case of neovascular AMD, 12 eyes from subjects over the age of 50 years old (3,600 B-scan images), and 11 eyes from subjects under the age of 50 years old (3,300 B-scan images) were obtained. Five feature extraction methods were either reproduced or developed in order to determine if significant differences could be observed between the early and intermediate AMD subjects and control subjects at the eye level. Through non-parametric testing it was established that two AMD biomarker extraction methods (choriocapillaris flow voids analysis and a drusen segmentation method) produced measures which showed significant differences between groups, and which were also uniformly represented across the frontal plane of the eye. It was then desired to leverage the measures and generate a B-scan level, interpretable machine learning-based AMD classification model. Frequency spectrums resulting from the fast Fourier transforms of spatial series derived from measures believed to be representative of the two biomarkers were obtained and used as features to train a random forest and a deep forest classifier. Principal component analysis was used to reduce dimensionality of the feature space, and model performance and predictor importance were assessed. A new method was devised which allows automated 3D reconstruction and quantitative evaluation of retinal flow signal patterns and incidentally of retinal microvasculature. Measures representative of drusen and choriocapillaris were leveraged to create interpretable models for the classification of early and intermediate AMD. As the worldwide prevalence of AMD increases and OCT devices are becoming more available, a greater number of highly trained personnel is needed to interpret medical information and provide the appropriate clinical care. Expert analysis and grading of AMD through OCT images are expensive and time consuming. The models proposed could serve to automate AMD detection, even when it is asymptomatic, and signal to an ophthalmologist the need to monitor and treat the condition before the occurrence of severe visual loss. The models

are transparent and provide classification from single cross-sectional images. Therefore, the automated diagnosis tool could also be used in situations where only partial medical data are available, or where there is limited access to health care resources.

TABLE OF CONTENTS

LIST OF TABLES

LIST OF FIGURES

LIST OF SYMBOLS AND ABBREVIATIONS

AMD	Age-related macular degeneration
BM	Bruch's membrane
CC	Choriocapillaris
CNV	Choroidal neovascularization
CNN	Convolutional neural network
DF	Deep forest
DL	Deep learning
eAMD	Early age-related macular degeneration
ETDRS	Early treatment diabetic retinopathy study
C1	ETDRS grid central 1 mm subfield
I1	ETDRS grid inner inferior subfield
N1	ETDRS grid inner nasal subfield
S1	ETDRS grid inner superior subfield
T1	ETDRS grid inner temporal subfield
ET	Extremely randomized trees
FV10000	Flow signal voids greater than 10,000 μm^2
FCN	Fully convolutional network
iAMD	Intermediate age-related macular degeneration
k-NN	k-nearest neighbours
ML	Machine learning
OCT	Optical coherence tomography
OCTA	Optical coherence tomography angiography
PCA	Principal component analysis
RF	Random forest
RCP	Retinal capillary plexuses
RPE	Retinal pigmented epithelium
RPEb	Retinal pigmented epithelium bottom
RVI	Retinal-vitreous interface
3D	Three-dimensional
2D	Two-dimensional

LIST OF APPENDICES

CHAPTER 1   INTRODUCTION

Age-related macular degeneration (AMD) is a degenerative eye condition with early manifestations localized in central regions of the human retina. Severe central visual acuity loss is associated most commonly with the neovascular, more advanced form of the condition featuring the abnormal growth of new vessels beneath and into the retinal space [1].

As its name indicates, age is one of the main risk factors and individuals who develop the condition are typically aged 50 years or above, whether or not visual symptoms are present [1]. The condition is also disproportionally prevalent in women and non-Hispanic White Europeans. AMD ranks first as a cause of severe, irreversible vision impairment in the developed world with its older populations [1], and macular degeneration ranks third globally after cataract and uncorrected refractive error [2]. Adding perspective to its pervasiveness in the industrialized world, the prevalence of AMD in the United States has been described as comparable to that of the combination of all invasive cancers, and more than twice more common than Alzheimer's disease [3]. Unlike AMD, cataract and uncorrected refractive error are both fully treatable. Global trends suggest that while the number of persons affected by uncorrected refractive error and cataract has been in decline over a 20 years period from 1990 to 2010, the prevalence of macular degeneration-associated vision loss has increased [2]. A little more than a decade ago, it was estimated that annually in Canada the number of new cases of non-neovascular AMD (also called non-exudative AMD) reached 180,000 [4]. The incidence of the neovascular form of the disease in Canada was estimated at 17,100 new cases annually. Besides the significant impact on the quality of life of those with AMD, the condition is believed to be responsible annually for approximately 2.6 billion in losses to the Canadian economy. The incidence of advanced AMD increases log-linearly with age [5]. As the ageing populations of the developed world increase, the costs associated with AMD are expected to increase in proportion [3].

AMD treatment options can slow the progression of intermediate AMD and provide short-term prevention from the abnormal growth of new vessels. In both instances, monitoring and early detection leads to a better visual outcome. At this time, clinical assessment of AMD often involves Optical Coherence Tomography (OCT) which unlike any other imaging method, can provide detailed cross-sectional images of the back of the eye. OCT measures the backscatter intensity of light and OCT beam behavior is a function of retinal tissue interactions. A more recent imaging

method called OCT angiography (OCTA) allows visualisation of the flow signal from the eye retinal vasculature and the choroid. The development of diagnostic methods which leverage OCTA and the implementation of the technology in clinical settings is ongoing.

The severity of adverse effects associated with AMD, the trends suggesting that the proportion of persons at risk is expected to continue to rise in Canada and worldwide, and the need to combine treatment options with effective detection methods justify the exploration and development of new diagnostic methods. Novel disease feature extraction and disease classification computer algorithms could further assist clinicians as part of the diagnostic process, automate parts of the process and provide new insight into the condition.

Given previously developed software, the availability of an OCTA-enabled device and the direction of ongoing research and clinical approaches, the research project was initiated with the overall goal of engineering specific features encompassing early, intermediate and advanced stages of the disease. It was also intended to leverage robust discriminators which were most uniformly represented across the frontal plane of the eye towards the development of a method which allows effective and interpretable classification of the early and intermediate stages.

As stated in the overall goal, the project was completed in two main steps. The first step consisted of extracting several spatial features from retinal and choroidal OCT and OCTA data and determining which of them showed a statistically significant difference between a group of control subjects, and a group composed of early and intermediate AMD subjects (eAMD and iAMD, respectively). The second step consisted of obtaining spectral features from retinal OCT and choroidal OCTA data which were uniformly represented at eye level and applying them at the cross-sectional image level. In this respect, Fourier transformation resulted in descriptors which yielded promising classification performance and machine learning (ML) model interpretability.

The present document begins with a review of the relevant literature surveying concepts and advances upon which the research project was constructed. Having described important concepts and advances, the review of literature ends with a detailed outline of the project objectives. Then, the methodology used is provided for each of the detailed objectives outlined. The methodology is followed by the results which each of the research project's key steps yielded. At the end of the document the results are discussed and a conclusion highlights some of the project's limitations and available avenues for future research.

CHAPTER 2   REVIEW OF LITERATURE

Several core concepts and scientific advances helped establish a direction for the research project. As part of the review of literature, first a brief overview of normal and AMD-associated eye anatomy and physiology is given. Then, a description of the devices and tools which supported the project or are closely related with the software development are given. Within the description of the devices and tools, basic principles behind OCT and OCTA imaging are provided as well as a survey of software approaches connected to the detailed objectives.

For eye planes and directions, the convention set forth in [6] is used throughout the document and a modified diagram of the nomenclature is shown in Figure 2-1(a). An OCT cross-sectional image with designated anatomical features is shown in Figure 2-1(b). Additional naming conventions pertaining to OCT images are elaborated upon in the OCT and OCTA sections.
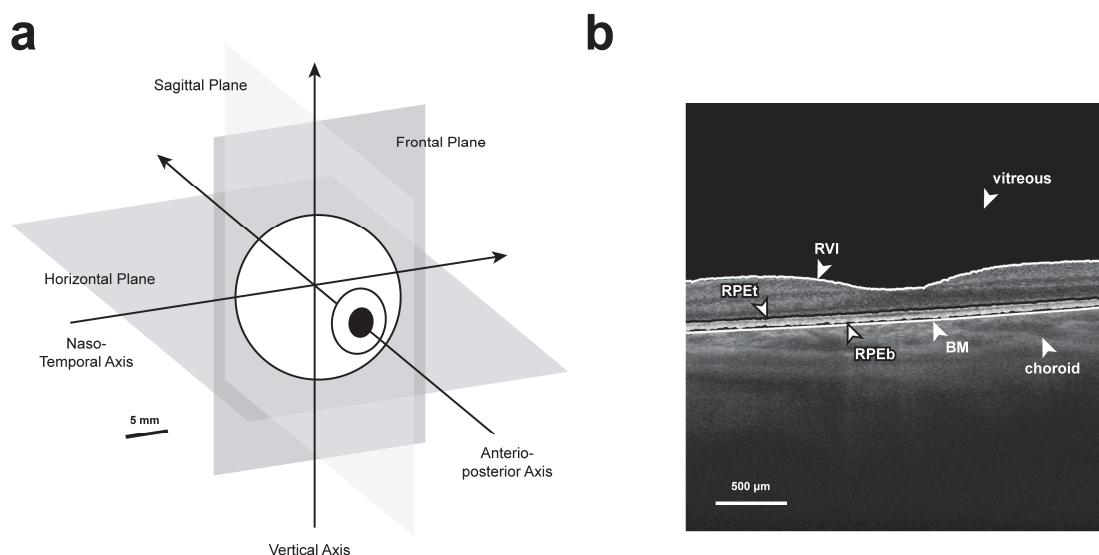
Figure 2-1 Eye planes and directions and OCT cross-sectional anatomy of the eye. (a) Diagram and nomenclature of the planes and axes of the human eye (modified from [6]). (b) OCT cross-sectional image with designated anatomical features.

2.1 Relevant eye anatomy and physiology

2.1.1 Bruch's membrane (BM), retinal pigment epithelium (RPE) and retinal-vitreous interface (RVI)

Bruch's membrane (BM) is a fine layer high in collagen and elastin connective tissue which is located between the capillary region of choroidal blood vessels (CC), and the retinal pigment epithelium (RPE). The BM is involved in the prevention of cellular migration as well as the passive diffusion of molecules, serum constituents and other elements across the retina and CC [7]. One such molecule is the vascular endothelial grow factor (VEGF) which is secreted by the RPE in order to maintain CC integrity. Geographic atrophy is defined as an area where the RPE is absent or severely attenuated [8]. In AMD diseased eyes affected by geographic atrophy, CC regions directly under areas of enduring RPE are unimpaired [9]. As the name indicates, the retinal-vitreous interface (RVI) represents the boundary between the retina and the vitreous body which is the gel that occupies the overlying space within the eyeball.

2.1.2 Retinal capillary plexuses (RCP) and choroid

Blood supply responsible for the delivery of nutrients and oxygen to retinal cells is provided in part by the central retinal artery and retinal vein, and also to a greater extent from larger vessels posterior to the retina, collectively referred to as the choroid [10]. The central artery and central retinal vein branch out into the retina and form layers of blood vessels called the superficial and deep retinal capillary plexuses [11]. The choroid vessels are the main or sole source of blood supply in central regions of the retina lacking blood vessels such as the fovea, and together they provide approximately 85% of retinal blood supply [12].

2.1.3 Choriocapillaris (CC)

The choriocapillaris (CC) is a specific layer of small vessels restricted to the inner fraction of the choroid. The layer is reported to be located at a distance varying between zero and 34 µm posterior to the BM in the axial direction, and to possess a thickness varying between 4.4 and 30 µm deep into the choroid [13]. It supplies oxygen and metabolites to the RPE and the outer retina and represents the only source of metabolic exchange to the foveal avascular zone. Vessel density within the CC layer decreases with age [7]. More broadly, physiological changes to it are

associated with a variety of retinal diseases including AMD. There is an interdependency between the CC and the RPE, and damages to either one will result in degeneration of the other. Drusen are known to manifest at areas of low choroidal blood flow and are therefore considered a marker for CC loss.

The Figure 2-2 shows a volume rendering of OCT and OCTA. The image situates the choroid layer below the retina. The OCTA flow signal (in blue) is slightly raised in the antero-posterior direction and structures corresponding to the RCP can be seen above the structural retinal surface. Dense regions of OCTA signal corresponding to the choroid, including CC appear below the RCP (also in blue).
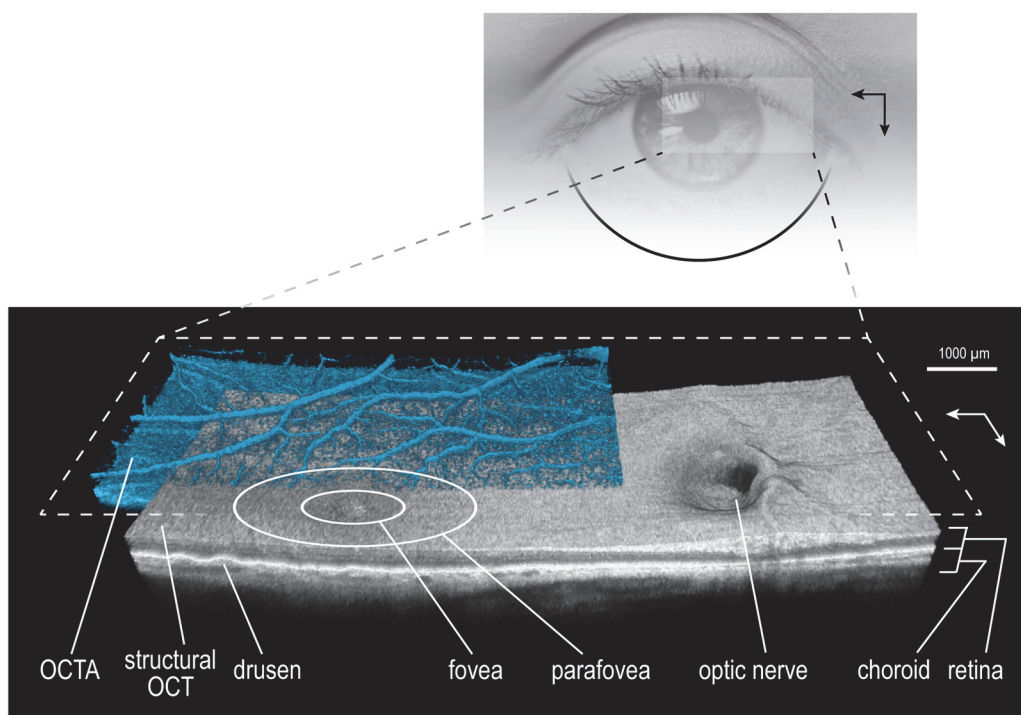
Figure 2-2 Volume rendering of structural OCT (grey) and OCTA (blue) of the retina and choroid.

2.1.4 Age-related macular degeneration (AMD)

Age-related macular degeneration (AMD) is a progressive eye disease which affects blood supply to the eye and is the most important cause of blindness in developed countries. AMD is mainly characterized by abnormalities in deeper layers of the retina including the RPE and the BM, and the choroid. These abnormalities include areas of thickening of the BM called drusen, and

abnormal proliferation of blood vessels which tend to appear under the retina and progressively spread into and within the retinal space [14-16]. Defining features of the disease also include RPE hypo- (associated with cell loss) and hyperpigmented regions [17]. An abnormal proliferation of blood vessels can be referred to as choroidal neovascularization (CNV) when it initially appears at the choroid level, and retinal angiomatous proliferation when it appears at the retinal level. Similarly as with drusen, CNVs develop in regions of compromised CC and are believed to arise in order to compensate for reduced CC blood circulation [13]. Two manifestations of AMD are differentiated through their attributes. The first type is called non-exudative, or 'dry' AMD, and is characterized by a decrease in vascular density and a decrease in the luminous intensity of the vessels. The second type is called exudative or neovascular AMD and differs from the first type through the presence and growth of CNV from the choroid.

Current diagnostic approaches for AMD can entail the injection of intravenous dyes such as fluorescein and indocyanine green to visualize normal and abnormal ocular vasculature. Unless stereoscopic viewing is used, the information obtained using contrast agents is of a 2D qualitative nature [18]. Contrast agents are also only effective for a limited time. The continued exploration of non-invasive methods that provide a greater amount of diagnostic information is further justified by the risks and side effects associated with the injection of contrast agent. A blood flow related pathogenesis model of AMD links the disease to increased rigidity of the sclera resulting from the accumulation of atherosclerotic plaque. According to the model, higher rigidity would promote resistance to blood circulation and prevent normal choroidal venous drainage. From reduced blood perfusion follows RPE functional changes occasioning the growth of drusen and damage to the neural retina [11].

Evidence supports the effectiveness of antioxidant vitamins and minerals as a means of slowing the progression from iAMD to advanced AMD [1]. At the neovascular advanced stage of the condition, the most successful means of managing the growth of new vessels involves the intravitreal injection of anti-vascular endothelial growth factor (VEGF). While the injection of anti-VEGF agents has been demonstrated to decrease legal blindness as much as 70 % over a span of two years [19], gains are mostly lost in two-thirds of persons with AMD which have been monitored for more than seven years [20]. The limitations of anti-VEGF agents reinforce the importance of early detection and management for persons at the iAMD level.

2.1.5 Drusen

Drusen are a defining clinical feature of AMD and occur early in its progression. Drusen are localised lipid, mineral and protein-containing extracellular deposits which are found between the BM and the basal lamina of the RPE (RPEb) [21, 22]. The accumulation of drusen is associated with a progressive decline in BM conductivity [23] and drusen in general can be responsible for macular-related dysfunctions such as a diminution in color contrast, central visual field or spatiotemporal sensitivity [21]. Drusen can be classified according to their location and morphology, and types include cuticular, soft and hard drusen, and subretinal drusenoid deposits [21, 23, 24]. Hard and cuticular drusen are yellow-white lesions spanning less than 63 μm in diameter and can be distinguished from each other by their lifecycle [21, 24]. In small numbers, neither type is considered a risk factor for developing AMD or for disease evolution to later stages of AMD. In great numbers however, hard drusen are associated with visual loss in AMD. Soft drusen are typically larger lesions with poorly defined edges. Like subretinal drusenoid deposits which are found at the inner extremity of the RPE, they are linked with progression to advanced stage AMD [23].

2.1.6 Age-related macular degeneration (AMD) clinical classification

AMD is commonly classified into dry (non-exudative) or wet (exudative, neovascular) type based on indicators of disease progression. Histopathological evidence has revealed that in eyes with a dry AMD diagnosis, there is a reduction in choroidal vessel density and vessel lumina. Wet AMD which may occur later in the disease timeline, is characterized by the appearance of CNVs originating from the choroid and which may proliferate under or through the BM as well as into the RPE and the broader retinal space. Complications which can arise from CNVs include serous or sanguineous detachment of the RPE or retina, pigment modeling, RPE tears, and lipid exudation [17].

A committee of AMD experts formed towards establishing a clear standard for AMD classification determined that the common classification of AMD into dry and wet type can result in inconsistencies. Specifically, the committee advised that like wet AMD, the term dry AMD should be restricted to describing an advanced manifestation of AMD. Dry type would be used to denote the presence of geographic atrophy. Under a novel, alternate classification scheme, the committee

recommended that AMD be instead classified into early, intermediate and late AMD. The eAMD stage refers to eyes where medium drusen (≥ 63–< 125 μm diameter, en-face view) can be identified and in the absence of pigmentary abnormalities associated with AMD. The iAMD stage refers to eyes in which large drusen, or where pigmentary abnormalities associated with at least medium drusen are found. Late AMD stage refers to eyes where GA or CNV lesions are present [15].

2.2 Optical coherence tomography (OCT), optical coherence tomography angiography (OCTA)

2.2.1 Optical coherence tomography (OCT)

OCT is a non-invasive imaging technique which allows in depth and in-vivo microscale visualisation of retinal and choroidal tissue. The OCT imaging device operates using low coherence light [25, 26] and allows the measurement of variations in backscatter intensity along the antero-posterior axis of the eye and its vicinity. The axial direction backscatter intensity profile is referred to as an A-scan and the grouping of a series of A-scans into a cross sectional image of the retina and choroid is referred to as a B-scan. The OCT acquisition gathers a series of B-scans, corresponding to a volume of the back of the imaged eye. The Figure 2-3 below shows the different types of OCT scans.
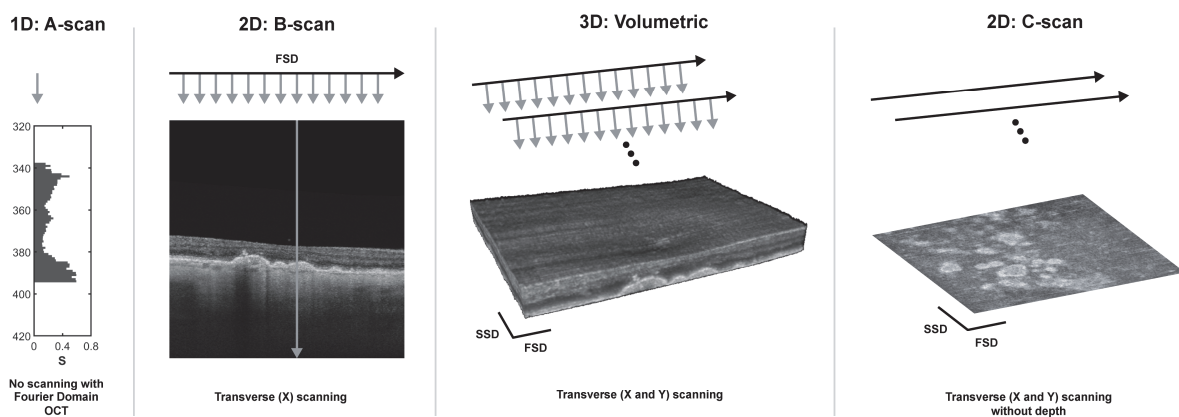
Figure 2-3 OCT types of scans. From left to right: A-scan, B-scan, volume rendering and C-scan (modified from [27])

2.2.2 Optical coherence tomography angiography (OCTA)

Through OCT, images of optical scattering from eye tissue are obtained [26]. When interacting with moving red blood cells, the optical signal which yields tissue spatial information varies over time [28]. OCTA designates a set of techniques which were developed towards isolating the variation in the OCT signal resulting from interactions with blood vessels. The B-scans generated through OCTA are motion-contrast images and enable visualization of a volume of the retinal and choroidal vasculature at near histology level resolution [10].

In comparison with fluorescein angiography (a dye based approach), better visualization of all blood vessel containing layers has been reported [29]. Currently, limitations of OCTA include smaller field-of-view, the fact that vessel leakage is not shown and the tendency for scans to be affected by movement artifacts [10, 29]. Lesions with slower blood flow, such as in microaneurysms or fibrotic CNVs, are not detected [29, 30]. With regard to CC imaging, OCTA analysis is typically performed using a representative en-face image [7]. While basic agreement is achieved between CC measurements obtained using devices equipped with different OCTA enabling algorithms, the measurements are not transferable. The visualisation of CC intervascular spaces is also limited [13]. The Figure 2-4 below provides a simplified schematic of a method of OCTA signal detection and construction, and Figure 2-5 below shows the different types of OCTA scans.
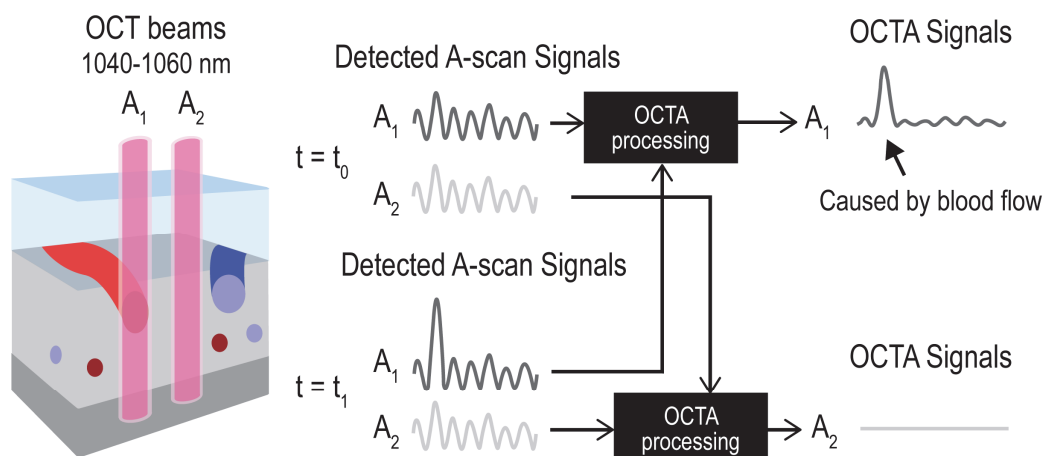
Figure 2-4 A schematic of OCT signal detection and OCTA signal construction (modified from [10])
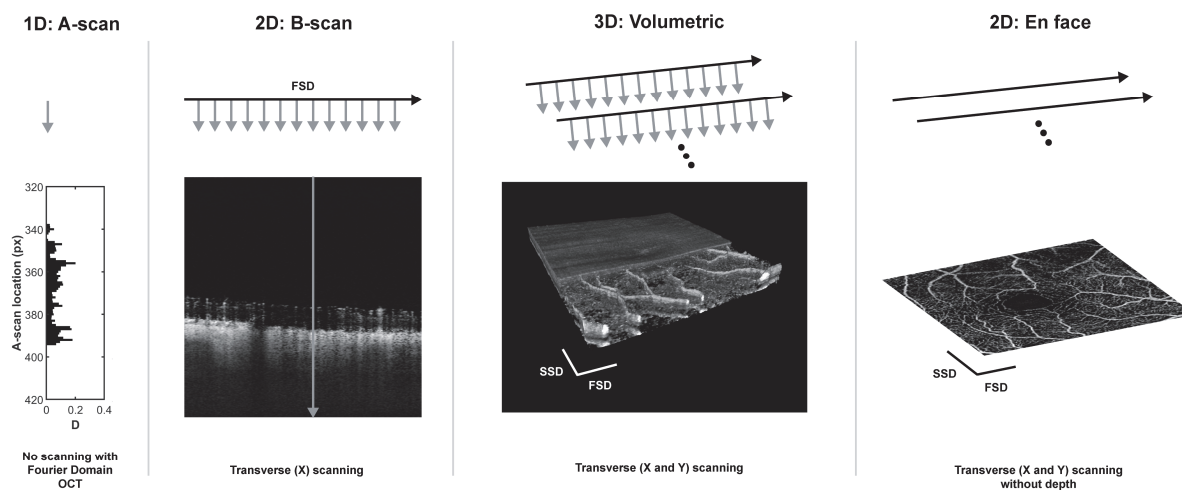
Figure 2-5 OCTA types of scans. From left to right: A-scan, B-scan, volume rendering and en face image.

2.3 OCT and OCTA images feature extraction methods

2.3.1 Retinal capillaries plexuses (RCP) network graph

Several approaches to the quantification of OCTA retinal flow signal patterns have been described [31-34]. Chu et al [31] evaluated the use of five indexes associated with the 2D segmentation of vessels and their skeletonization from maximum value projection en-face OCTA images. Leahy et al [35] have described techniques which allow 3D mapping of the rat inner retinal vascular network using OCTA. CNVs have been quantified in 2D from OCTA images [33, 36] and associations have been found between measures derived from them and treatment burden.

2.3.2 Choriocapillaris (CC) flow voids analysis

The maximum transverse resolution of images from OCTA enabled devices obtained through a single acquisition is situated at 15 μm (with a 20 μm upper range) [13, 37]. In comparison, CC diameter measurements are reported to reside in the 9.6-40.2 μm range [38]. The limited transverse resolution of OCTA images from a single scan prevents visualization of individual choroid capillaries from the CC layer, or of the very small spaces between them. Larger dark areas of absent flow signal, which do not necessarily reflect CC anatomic structure, can be observed and have been termed flow voids. The state of the CC has been quantitatively evaluated using statistical measures associated with flow voids [9, 37, 39]. The OCTA flow signal produced by the CC are spotted a few micrometers posterior to the actual anatomical location of CC in the axial direction [13]. A representative image of the voids can be isolated by sampling a CC slab 10 μm thick, starting at locations 31 to 34 μm deep into the choroid (depending on the device used). Thresholding is then performed on a maximum projection image of the CC slab and voids are quantified as areas greater than or equal to a selected size. In this manner, flow voids distribution, size and number in health and disease have been investigated and it was determined that the distribution of the number of flow voids versus size of the voids follows a power law. When logarithmically plotted, the data follow a linear association and trendline parameters can be obtained [37].

Notably, the difference between the distributions of signal voids greater than 10,000 μm^2, and greater than 40,000 μm^2 (FV10000 and FV40000, respectively) as well as the differences between the distributions of the slope, m, and the intercept, b, of the trendline have been identified as useful

means of discriminating between healthy and diseased eyes [9, 37]. At this time, adaptive local thresholding, the computation of logarithmically binned signal void sizes and the generation of a log-log plot are performed manually and the approach could benefit from further automation [9]. The presence of large drusen (>40 µm in height) may result in significant projection artifacts at the CC region of interest [37].

While the resolution of images following single OCTA acquisitions remains limited, evidence suggests that averaging registered en-face maximum projection images obtained from selected CC slabs provides superior results [38]. For a given subject, a morphologic pattern that is closer to the meshwork pattern seen on histology can be successfully attained [38]. Significant differences in flow voids measurements and trendline parameters were observed after the averaging was performed [38].

2.3.3 Drusen segmentation methods

Owing to their central role in the characterization of the early stages of AMD, several approaches to the segmentation of drusen from OCT scans have been proposed. The approaches can be categorized into layers-based and ML-based. From segmented drusen, it becomes possible to derive clinically meaningful quantitative measures which may include and are not limited to drusen thickness (or height), area, and volume [40, 41]. ML-based drusen segmentation methods are referenced with other methods used as part of subsequent section 2.4.

2.3.3.1 RPEb-BM drusen segmentation

As drusen lie within the space between the BM and RPE, layers-based drusen segmentation commonly depends on accurate segmentation of the BM and of one or both boundaries of the RPE layer. Once the BM and RPE boundaries have been established, drusen can simply be defined as the space between them. A potential drawback of layers-based segmentation is its vulnerability to BM and especially RPE segmentation errors. Noise and homogeneity with contiguous tissue anterior to the RPE can make it difficult to segment even in normal eyes [40]. The likelihood of errors may increase with AMD disease progression, as the RPE is increasingly deformed by the presence of drusen [21]. When compared with fundus image analysis, BM and RPE-based segmentation tends to overlook drusen with low elevation and subretinal drusenoid deposits [42, 43].

2.3.3.2 En face drusen segmentation

A layers-based method which circumvents segmentation of the pathologic RPE has recently been introduced [23]. The method consists of selecting two slabs, the first directly next to and anterior to the BM and the second, slightly anterior to the RPE and still using the BM as a reference. After the slabs have been selected, surfaces within each slab are put through a series of averaging and filtering processing steps towards isolation of the areas covered by drusen. The image processing results in an accurate en-face regional map of drusen. There is also a greater likelihood of detecting early, smaller drusen which do not cause very significant RPE basal membrane separation from the BM, as well as subretinal drusenoid deposits which appear at the top of the inner RPE boundary.

2.4 Classification in age-related macular degeneration (AMD) detection

Machine learning (ML) regroups a variety of algorithms which can be used to achieve data processing goals. The choice of the algorithm is driven by the desired outcome. Owing to the variety and complexity of the various algorithms included under the ML umbrella term, brief descriptions of architectures pertaining to the specific applications surveyed in the present section will be provided along with references directing to more detailed descriptions. A frequent goal of ML algorithm design is classification. At the learning (or training) stage, ML classification algorithms are constructed using features from a set of observations, with each observation belonging to a class. Once the learning has taken place, features from a newly introduced observation (of an unknow class) can then be fed as input to the algorithm, which will then output a predicted class. In the context of computer aided diagnostics, observations can be images of a human body organ such as eye images belonging to a number of individuals. The features of ML classification can consist of (and are not limited to) the measurements of known biomarkers extracted from a medical image, and also the pixels of a medical image. ML classification is supervised, and classes (or labels) belonging to observations, such as different eye diagnoses or the severity of an eye condition, have been determined and assigned to observations before the learning takes place.

As their use has been associated with increased ML classification performance and clear advantages especially with regard to image processing, a growing number of computer aided

diagnostics applications implement deep learning methods. Deep learning (DL) constitutes a subset of machine learning [44-46] and two types of DL algorithms, convolutional neural networks (CNNs) and fully convolutional networks (FCNs) are particularly well suited for computer vision tasks [47, 48]. A strength of CNNs and FCNs lies in the way in which an image can be transformed into useful representations. The representations can in turn be used as features for classification, or as a starting point for additional operations leading to the classification of targeted image areas, respectively. In contrast with DL, which is more recent, more established ML classification methods can be referred to as conventional ML. Under this scheme, conventional ML classification methods include support vector machines (SVM), which in their simplest form find a hyperplane in the input feature space which effectively separates observations belonging to each class [49]. They also include non-layered tree-based methods such as random forest (RF), which are an ensemble of decision trees leveraging strategies designed to prevent overfitting [50-52]. Another conventional ML method is the k-nearest neighbors algorithm (k-NN) which assigns observations to classes based on the calculation of their distances from each other within the feature space [53].

The detection of AMD using ML has been primarily dominated by two imaging modalities namely, fundus imaging and OCT. ML approaches to AMD detection involving OCTA images are currently lacking. Fundus imaging consists of a color photograph of the retina obtained using a camera. As such, it precedes OCT and remains widely used often as an integral part of clinical interventions in ophthalmology [48, 54]. As with OCT and as part of clinical interventions, biomarkers of disease can be identified through the manual inspection of fundus images. Biomarker findings using one imaging method may not directly extend to the other. At least in the case of drusen which are quantifiable using either modalities, evidence suggests that measurements agree only partially [42, 55].

It can be useful to further distinguish between two broad categories of approaches to the generation of ML models associated with the detection of AMD. ML models can be generated more broadly as part of a local approach to the characterization of disease, i.e., with supervision towards the isolation of clinically meaningful biomarkers [56]. The isolated biomarkers can then be used to assess the condition of the eye. A second broad category, the global approach to the generation of ML models associated with the detection of AMD, is concerned with a more direct classification of images without the intermediate step of extracting clinically meaningful biomarkers [56]. The classification of images using image representations derived from CNNs constitute an example of

the global approach. A ML model building strategy informed by current trends in AMD management [1] would consist of seeking the classification of eAMD and iAMD instead of advanced AMD, at stages where monitoring or treatment to prevent progression remain an option. Consideration to this preferred strategy is given in the present evaluation of applications of ML methods to AMD detection from fundus and OCT images.

In the case of fundus images, it is reported that local approaches to AMD detection are generally aimed at the identification of drusen [57]. The aim is consistent with the need to prevent AMD progression to the advanced stage as drusen are a hallmark of eAMD and iAMD. A pioneering application of ML to fundus image drusen detection used a k-NN classifier and linear discriminant analysis to classify pixels from color fundus photographs as either drusen, exudates or cotton-wool spots [58]. Following a similar trajectory, FCN architectures have been used for the classification of targeted fundus image areas [56, 59]. The developed algorithms provide a segmentation map of red lesions (haemorrhages and microaneurysms) and bright lesions (hard and soft exudates, drusen and cotton-wool spots). State of the art global approaches to AMD detection have involved the generation of image representations through CNNs [60-63] or ensembles of CNNs [64] which are combined with the standard fully connected layer for classification. Closely related architectures have utilized CNNs and ensembles of CNNs and integrated them with conventional machine learning algorithms (instead of the standard fully connected layer) for classification including SVM [65] and RF [66], respectively. A notable exception to other global approach architectures fuses CNN image representations with additional non-visual patient data as input to a RF classifier [67]. State of the art global approaches using fundus images feature eAMD detection or AMD severity assessment, demonstrating consistency with the goal of monitoring progression.

In the case of OCT images and in line with a local approach, DL algorithms using standard CNN and modified CNN architectures have achieved state-of-the-art OCT drusen segmentation [68, 69]. A different local approach involved the extraction of texture features from a manually delineated choroid region on B-scan images. The features were then fed to SVM, RF and basic neural network conventional ML models to classify B-scans as normal, dry or wet AMD [70]. Setting a precedent in computer aided diagnostics, a more comprehensive local implementation of DL involved a 3D ensemble of FCNs architecture which classified targeted regions of OCT volumes into segmented tissue maps [71]. Each output map from individual FCN consisted of fifteen classes including drusenoid pigment epithelium detachment and the RPE. The framework then fed the segmentation

maps as input features to an ensemble of CNNs for multi-label classification. The resulting clinically applicable classification labels included a multi-class referral suggestion and diagnosis labels including normal and drusen. ML models have been designed as part of a global approach to the detection of AMD using OCT images [72-74]. Echoing the previously described informed AMD detection strategy, biomarkers which are associated with the progression of AMD to the neovascular stage [41] were identified as part of a study [72]. Notably, experts labelled B-scans as non-exudative AMD based on the presence of either hyperreflective foci, hyporeflective foci within drusen or subretinal drusenoid deposits. The B-scans were likewise labelled by the experts as normal in the absence of the same biomarkers. A standard CNN architecture was used for classification.

A drawback of global approaches to using CNNs for AMD detection tasks is the difficulty associated with issuing an interpretation of findings [72] as defined in the context of ML [75]. The literature suggests that locally driven ML approaches can generate models and frameworks with good interpretability. With measures derived from known biomarkers as input, tree-based conventional ML models such as RF could be viewed as very interpretable and arguably more easily operated than neural network-based DL methods. Perhaps owing to these advantages and others, methods have been developed to combine several forest models into a layered, deep forest (DF) model [46, 76]. The resulting tools have been used sometimes in combination with other deep learning models [77-79]. In addition to involving OCTA, the literature suggests that there remain opportunities to explore the construction of DF models towards AMD detection.

2.5 Detailed research project objectives

Several key steps were undertaken, and detailed objectives are outlined below.

i.   Frontal plane subfields separation

First, the development of an algorithm which segregates regions of the back of the eye into distinct areas according to the ETDRS (Early Treatment Diabetic Retinopathy Study) grid was sought. The grid was introduced by the ETDRS group [80] and divides the macula into subfields. Grid-based analysis can allow the identification of subtle and spatially restricted changes which can be present in eye conditions [81]. The ETDRS grid is commonly used to divide retinal thickness measurements and has been exploited in the context of AMD research [82, 83]. All methods were

developed using the 3 × 3 mm OCT field of view. As a result, the grid features only the innermost and second circles of the original grid, encompassing five subfields.

ii.   Layers segmentation and retinal thickness map

The research project also required leveraging previously developed software allowing segmentation of retinal layers of the eye namely the BM, the top and bottom (RPEb) of the RPE and the RVI. The segmentations serve as a foundation from which the development of other methods becomes possible. A comparison of retinal thickness and retinal volume between controls and non-exudative AMD subjects is provided.

iii.   Retinal capillaries plexus (RCP) network graph

The neovascular form of AMD is responsible for the majority of severe central visual acuity loss [1]. Therefore, it was desired to devise a method which makes possible the automated 3D reconstruction and quantitative evaluation of normal and diseased retinal flow signal patterns (and indirectly, of retinal microvasculature) using OCTA. Through a network graph representation of segmented retinal flow signal patterns, the number of structural links and nodes are obtained. The quantity of links and the quantity of nodes reflect the presence of vasculature segments and their intersections, respectively. A comparison of the number of links and nodes between controls and non-exudative AMD subjects is provided. It was also intended to demonstrate the developed method's repeatability and the quantification of flow signal resulting from new vascularisation in the case of a late AMD (exudative) subject.

iv.   Choriocapillaris (CC) flow voids quantification

Research findings suggest that AMD is associated with noticeable changes to the small vessels located just below the retina and collectively named CC [37]. It was desired to implement the automation of CC flow voids quantification from images obtained using OCTA. Targeted features consisted of parameters from a trendline derived from the distribution of flow void sizes, as well as the fraction of flow voids exceeding 10,000 μm^2. Statistical tests were performed to identify the most robust discriminator.

v.   Drusen segmentation methods

Drusen are a defining feature of AMD. They are localised abnormal accumulations of material found between the BM and the basal lamina of the RPE (RPEb) [84]. Their type and quantity are

used clinically to evaluate AMD progression. Two different methods of drusen segmentation were pursued. The first uses the segmentation of the retinal layers of the eye. A thickness map of the difference between the RPEb layer and the BM layer is obtained and drusen is defined as locations which exceed a specified elevation threshold. The second required only BM segmentation [23] from OCT cross-sectional images. It was sought to evaluate the area and volume of drusen in comparison with controls and to validate area coverage against manual segmentation using common segmentation performance metrics.

vi.   Spectral analysis

The project aimed for the implementation of an available ML approach to normal and grouped eAMD and iAMD stage classification at the cross-sectional level. Drusen defined as a thresholded RPEb-BM thickness map and a binarized image representative of CC flow voids were identified as measures which provided significant differences at eye level between the control and non-exudative AMD groups. In both instances the unprocessed data are generally well represented across the whole frontal plane of the eye. As such, it was anticipated that deriving B-scan level features from the unprocessed data was feasible. Fourier transformation of the OCT and OCTA measures derived from the RPEb-BM space and CC level flow signal was sought.

vii.   Classification

It was intended to build a RF classifier and a cascade DF classifier. RF is a ML method which can be used to build classification models. It uses a combination of decision trees and statistical strategies designed to maximize the model's ability to generalise from trends in a given dataset [50-52, 85]. An advantage of RF models is their interpretability [52, 85]. Cascade DF combines multiple RF models and a similar model in parallel and in a series of layers in order to increase performance [76]. The project sought to determine whether spectral measures derived from the RPEb-BM space and CC level flow signal could be used to provide new AMD biomarker insight. The objective was also to assess the viability of classification based on spatial frequency features as a disease detection method. A schematic of the project workflow is detailed in Figure 2-6 below. A more complete diagram is provided in Appendix A.
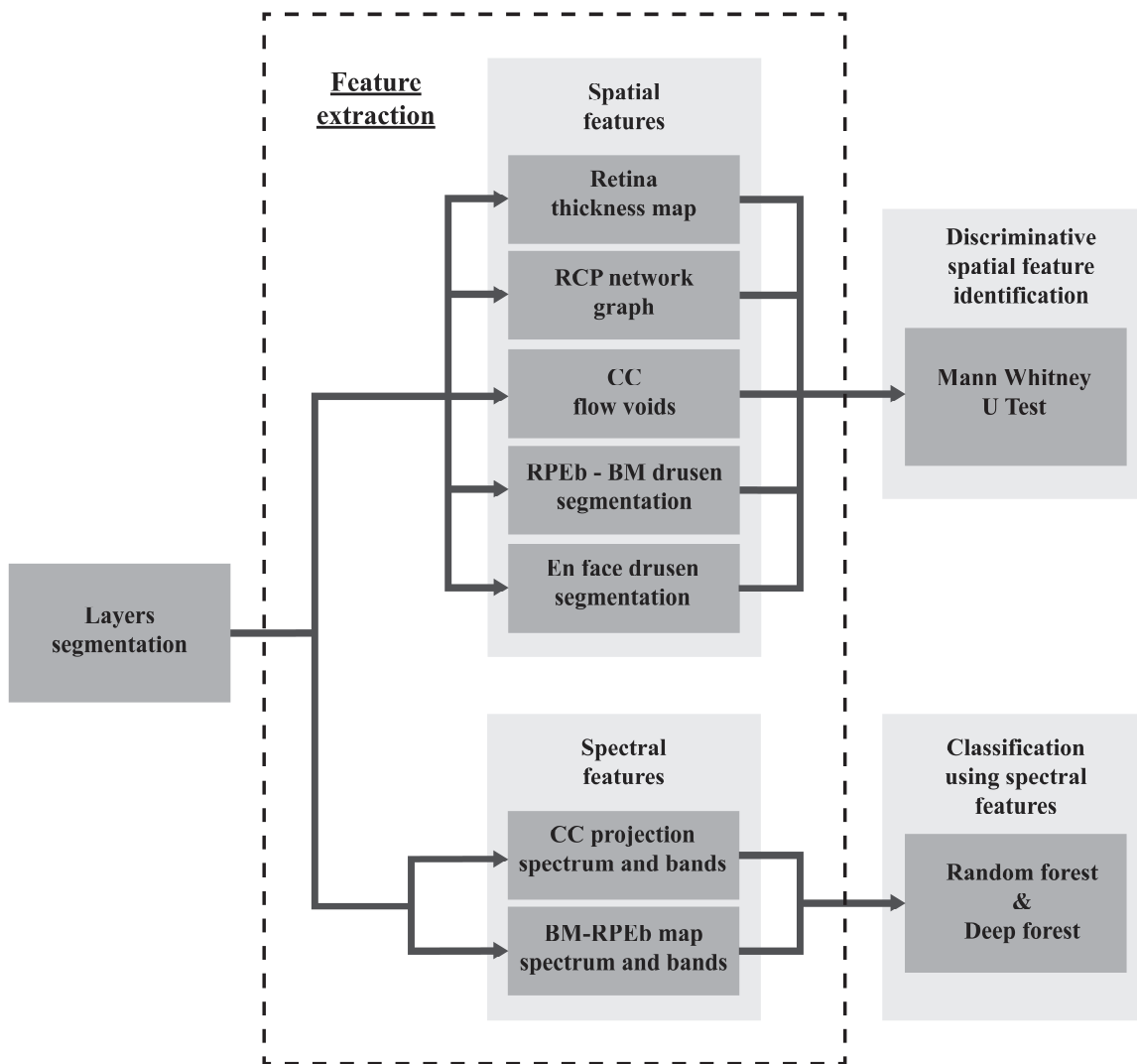
Figure 2-6 Simplified schematic of the research project workflow.

CHAPTER 3   METHODOLOGY

The methods which were used to produce and analyze the results are provided. First, a description of the experimental design up to and including the imaging protocols and software is provided. Then, as laid out in the introduction and Figure 2-6, the methodology is divided into the key objectives.

3.1 Experimental design

3.1.1 Study sample

The informed consent of the participants was obtained. Eyes from normal controls, eAMD and iAMD (non-exudative) subjects, and a case of neovascular AMD (exudative) subject were imaged using a Swept-Source OCT device. The project was carried out in conformity with the tenets of the Declaration of Helsinki. In total, 33 eyes were scanned, and study participants were between 21 and 86 years of age. Subjects without an AMD diagnosis were defined as controls of similar age to AMD subjects if they were over the age of 50 years old (mean and variance were not matched between similar age controls and AMD subjects). Scans include 12 eyes from similar age controls with an average age of 59.2 years old. They also include 11 eyes from non similar age, younger controls with an average age of 29 years old and which were recruited initially for prototyping of the different methods. In addition to the exudative AMD eye, the AMD scans include 10 eyes from subjects with eAMD and iAMD, who were diagnosed with non-exudative AMD in both eyes or have had at least one anti-VEGF injection in the contralateral eye. The eAMD and iAMD subjects had an average age of 75.9 years old. Clinical and demographical characteristics of the eAMD and iAMD subjects and the control subjects are detailed in Table 3-1 below.

Table 3-1 Characteristics of subjects who participated in the project.

	eAMD & iAMD	control G2, over 50	control G3, under 50
Images, no.	6000	7200	6600
Eyes, no.	10	12	11
Sex, no. (%)			
Male	5 (50)	3 (25)	5 (45.5)
Female	5 (50)	9 (75)	6 (54.5)
Age (yrs), mean (SD)	75.9 (6.2)	59.2 (5.7)	29 (6.1)
Eye, no. (%)			
Right	8 (80)	6 (50)	6 (54.5)
Left	2 (20)	6 (50)	5 (45.5)
Central macular thickness, mean (SD), μm	270 (35.5)	245.4 (21.2)	262.7 (25)

SD = standard deviation

3.1.2 Selection criteria

The exclusionary criteria were selected primarily in line with previous work seeking CC flow voids quantification [37]. As such, they included gross eye movements which can result in motion artifact in OCT images [86, 87]. Also included were ocular diseases and histories which could have a severe impact on scan quality or have resulted in characteristics which would greatly overshadow biomarkers of AMD. As indicated in [37], such eye conditions and histories were central serous chorioretinopathy, retinal or macular surgery, previous ocular laser photocoagulation or photodynamic therapy, previous retinal vascular occlusion and center-involving geographic atrophy. Subjects were required to have sufficient visual acuity or ability to fixate in order to follow the imaging device operator's instructions and ensure that scans were well-centered. Eyes with large drusen were included (drusen > 125 μm diameter, en-face view) despite shadowing of the CC (as can be seen in Figure 2-5), as the discriminative strength of measures was sought over the accurate representation of subretinal microvasculature.

3.1.3 Imaging protocols and software

All scans were conducted at the Maisonneuve-Rosemont Hospital Research Centre. The imaging of all participants was performed using the 3 × 3 mm field of view from a ZEISS PLEX Elite 9000

Swept-Source imaging device (PLEX Elite 9000; Carl Zeiss Meditec, Inc, Dublin, CA). The imaging device features a Swept-Source laser with a specified central wavelength between 1040 nm-1060 nm and with a scanning rate of 100,000 A-scans/s. At the selected field of view, pre-processed individual A-scans provide 3 mm depth with a 1.953 µm/px resolution (3000 µm / 1536 px). The same 3 × 3 mm field of view offers 300 A-scans per single B-scan. The device has a specified transverse resolution (along the eye's naso-temporal and vertical axes) of 20 µm which does not directly translate into the distance covered by the number of acquisition pixels. The images were resized to be true to physical proportions while also maximizing antero-posterior axis resolution, with consideration given to computational resources. For all feature extraction methods volumes were resized to 600 × 600 px, and 600 px depth (reducing depth resolution to 5 µm/px). Image processing was performed in the MATLAB computing environment (R2018a, The MathWorks Inc., Natick, MA, USA). The ORS dragonfly software was used to provide 3D rendered images, and several figures were created and arranged using Adobe Illustrator.

3.2 Frontal plane subfields separation

The ETDRS grid divides the eye along the frontal plane and into five subfields. The Figure 3-1 below shows the full ETDRS grid with labelled and abbreviated subfields. To determine the center of the grid, an algorithm finds the lowest retinal thickness location in the foveal region. As the 3 × 3 mm images generated from the OCT device are aimed at the fovea, the lowest retinal thickness point is searched within a circular indexed region with a diameter of 1 mm placed at the center of the image itself. If more than one low point is identified within the region, the median of the x and y-coordinates of all identified candidates is obtained and defines the center. The grid subfields then consist of two concentric circles centered at the lowest retinal thickness location and four radial lines spanning from the innermost to the outermost circle. The radial lines extend in the 45°, 135°, 225°, and 315° meridians and the innermost and outermost circles have diameters of 1 mm and 3 mm respectively. In comparison, the umbo, foveola, fovea, parafovea and the macula concentric circles are defined as having diameters of 0.15 mm, 0.35 mm, 1.5 mm, 2.5 mm and 5.5 mm, respectively [88]. To capture measurements in 3D space, the ETDRS grid masks are binary volumes which represent the projection of the original 2D masks along the antero-posterior axis of the eye.

a

Superior 2

Superior 1

Temporal 2

Temporal 1

Center

Nasal 1

Nasal 2

Inferior 1

Inferior 2

Central ring, 1mm

Pericentral ring, 3mm

Peripheral ring, 6mm

b

S2

S1

T2

T1

C1

N1

N2

I1

I2
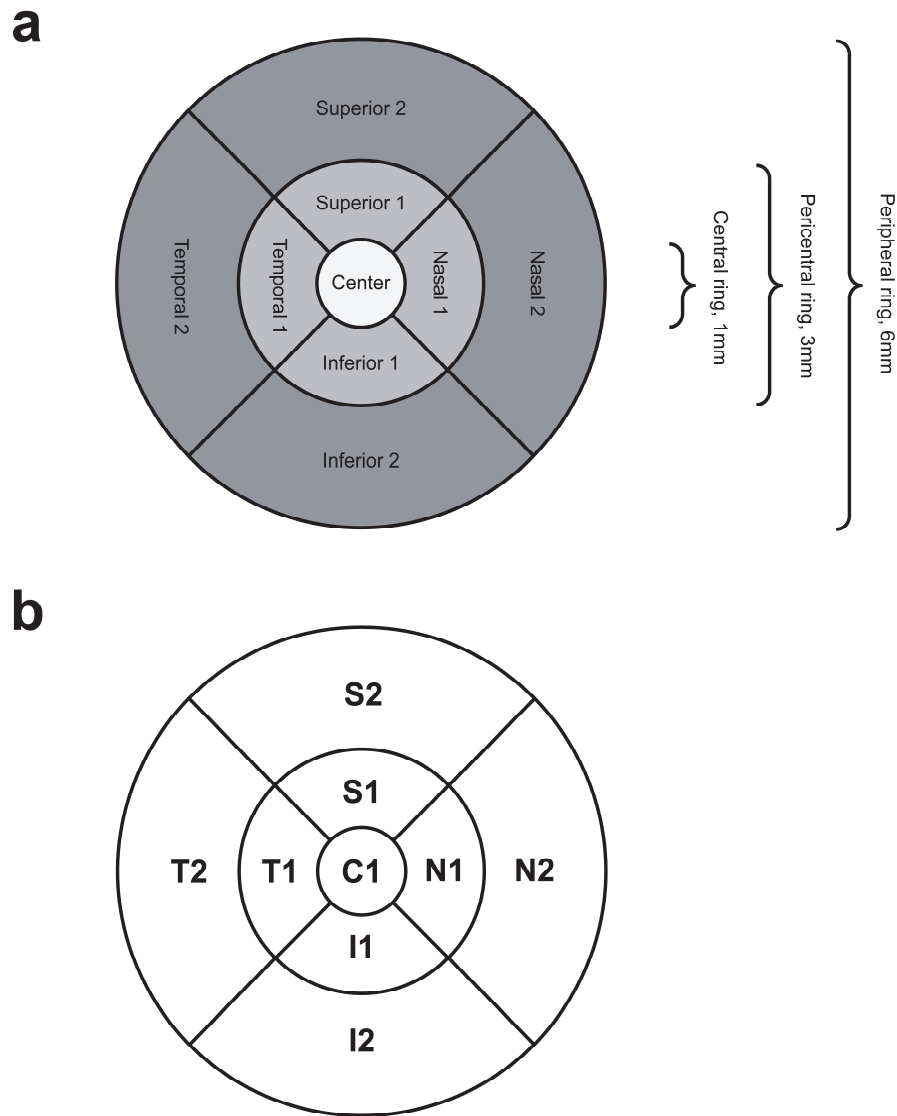
Figure 3-1 Full ETDRS grid with labelled and abbreviated subfields. Only subfields encompassed within the pericentral ring were used throughout the present research project. (a) Full grid with labelled subfields (modified from [81]). (b) Full grid with abbreviated subfields.

3.3 Layers segmentation and retinal thickness map

The isolation of the volume of interest from the OCT data was achieved using a series of two image segmentation algorithms as previously described and implemented on images generated using a different device [89].   The first consists of a cross-sectional pre-segmentation using A-scan gradients and an implementation of Dijkstra's shortest path algorithm [90], and provides the

location of the Bruch's membrane (BM), the high and the low boundaries of the retinal pigment epithelium (RPE), and the interface between the retina and the vitreous body (RVI). The first segmentation is less complex and less computationally expensive than the second. The second approach is a refinement of the pre-segmentation and involves a graph-cuts algorithm described by Li et al [91]. The graph-cuts algorithm is based on specific geometric constraints and provides improved segmentation results.

3.4 Retinal capillaries plexus (RCP) network graph

Superficial and deep retinal vascular plexuses were imaged. Retinal layers segmentation, flow projection artifacts correction, vessels segmentation and network graph algorithms were implemented over a 3 × 3 mm field of view and across the depth of the retinal space. 2D retinal vessels quantification measures were extended to 3D.

3.4.1 Region of interest extraction

Techniques have been developed to isolate choroid vessels from structural OCT images [92]. In contrast with structural OCT, in OCTA images the choroid and particularly the CC of healthy eyes are regions of high signal density. Volume rendering of retinal angiography data necessitates removal of the underlying high signal density choroidal region. The isolation of the volume of interest from the OCTA data was made possible through a series of two image segmentation algorithms described in section 3.3 concerning the retinal thickness map.

3.4.2 Flow projection artifacts correction

Shadowgraphic flow projection artifacts appear on OCTA images as signal intensity which trails in the antero-posterior axis direction, from retinal vessels into deeper regions. The artifacts can prevent or impair the ability to see deeper vascular networks as well as the generation of retinal volume rendering which reflects ground truth. The projections were corrected using the combination of an approach described by Zhang et al [93] and morphological operations. Zhang et al have found that the normalized projection artifact OCTA signals have progressively lower intensities than in-situ signals. The phenomenon can be exploited by first dividing the OCTA decorrelation signal value by the value of the structural OCT signal, S, which has a logarithmic relationship with the reflectance of the imaged tissues. In practice, an arbitrary constant was added

to the value of the structural OCT signal to prevent division by zero. Equations 3-1 and 3-2 below show how the projected flow (decorrelation) values, D, are normalized by dividing them by the log amplitude OCT signal, S. The variable, k, is an added proportionally low constant to avoid division by zero and corresponds to a fraction of the maximum intensity within the structural signal volume, Vs.

$$F = \frac{D}{S+k} \tag{3-1}$$

$$k = 10^{-4} \cdot \max(V_S) \tag{3-2}$$

It is then possible to eliminate the normalized signal values which follow a maximum normalized value for each 'A-scan', as shown in equation 3-3 below. In the present implementation of the PR algorithm, a factor to account for noise, as described by Zhang et al [93] was not included. In equation 3-3, i and n represent indexes along a given A-scan.

$$C_n = \begin{cases} D_n, & if\ F_n > \max(F_n),\ 1 \le i \le n - 1 \\ 0, & otherwise \end{cases} \tag{3-3}$$

Projection removal processing steps and their outcomes are shown at the A-scan level in Figure 3-2 below and at the B-scan and volumetric level in Figure 3-3 and Figure 3-4 below.
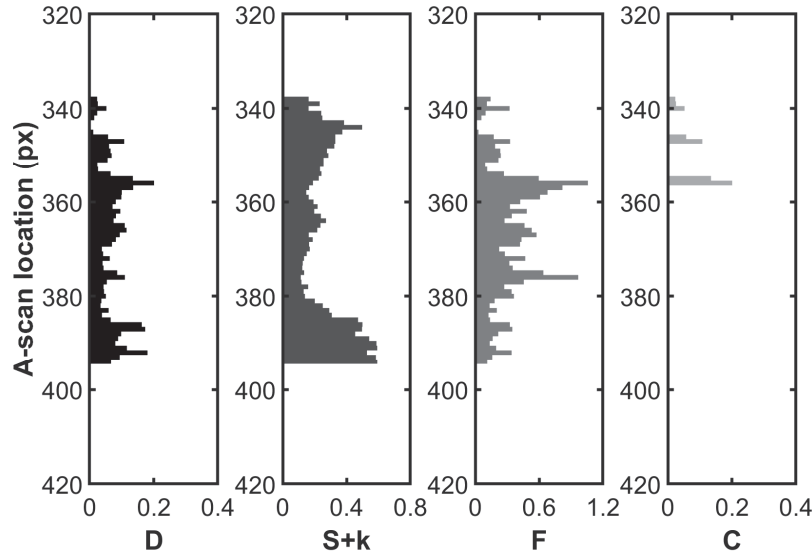
Figure 3-2 Projection removal processing steps and their outcomes.

a

b

c

d
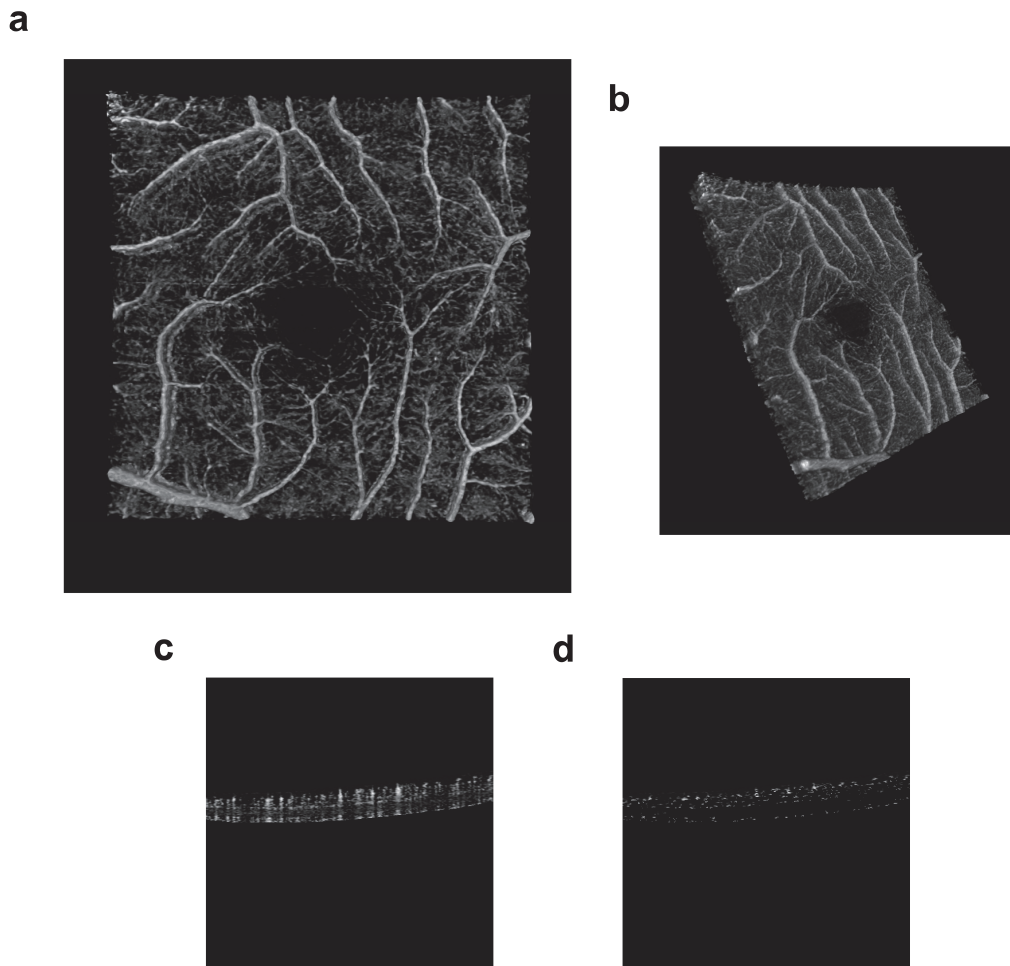
Figure 3-3 Retinal OCTA and implementation of the projection resolved (PR) algorithm (a) 3D rendered en-face view before implementation (b) 3D rendered side view before implementation (c) In situ flow signal before implementation (d) Flow signal after implementation.

3.4.3 Vessels segmentation

Following isolation of the region containing retinal vessels and the correction of shadowgraphic flow projection artifacts, the vessels themselves are segmented. It was determined that while the implementation of projection suppression maintains the in-situ signals, the remaining data are sparse and do not lend themselves well to further image processing. To recover the appearance of retinal vessels, the remaining pixels were morphologically dilated according to the known average physical dimensions of retinal vessels [94]. A morphologically dilated B-scan is shown in Figure

3-4(c) below. As can be seen along the BM in Figure 3-4(c), projections are not completely removed using the correction method. In the interest of isolating retinal vessels, the BM boundary was raised and all artifacts below it were cropped.

a

b

c

d
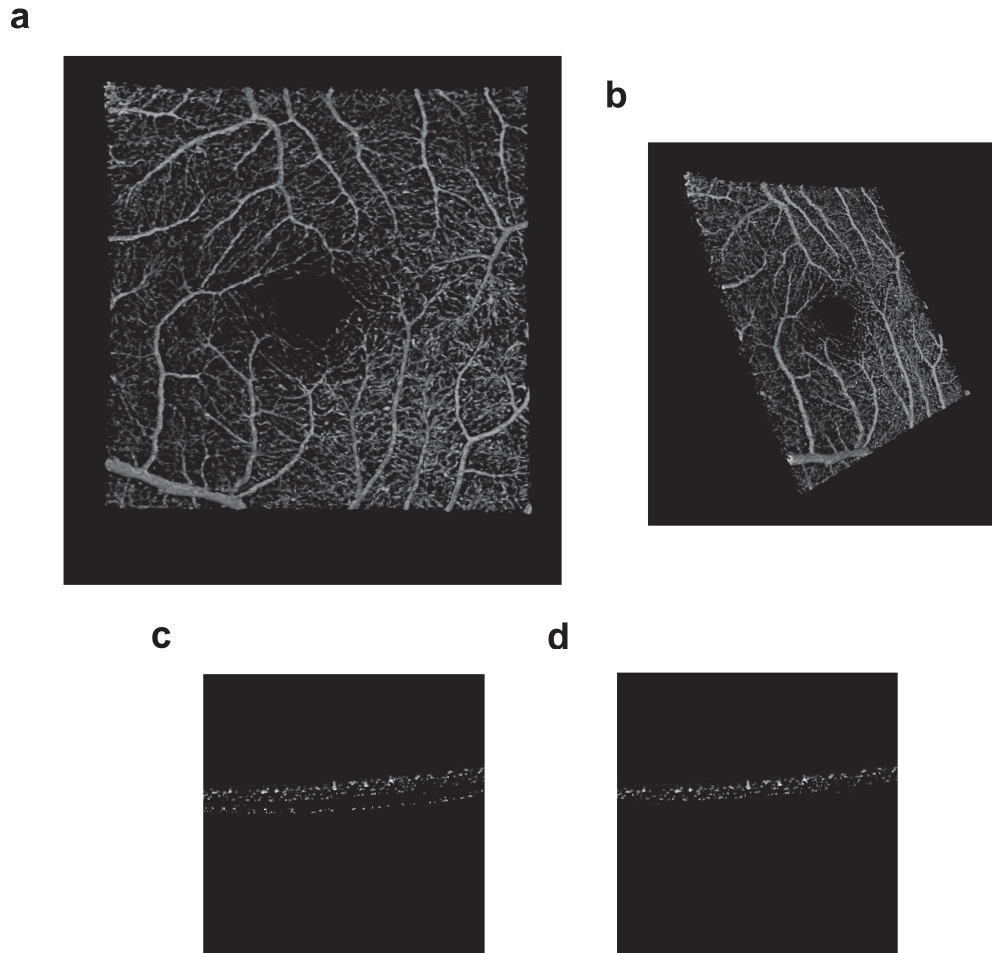
Figure 3-4 Retinal OCTA and implementation of the projection resolved (PR) algorithm (a) 3D rendered en-face view after implementation and dilation (b) 3D rendered side view after implementation and dilation (c) Flow signal after dilation (d) Flow signal after outer retinal artifact removal.

An open-source algorithm for the segmentation of retinal blood vessels from fundus images is provided by Coye [95] and is based on iterative thresholding [96]. Fundus images are similar to en-face OCT and OCTA images, and optimal en-face OCTA images can be generated through

maximum value projection [97]. The fundus image-based algorithm was adapted to allow the vessels segmentation of en-face OCTA images. Towards extending the 2D approach and achieving volume segmentation of the retinal angiography data, the adapted segmentation algorithm was applied iteratively to each en-face plane (along the antero-posterior axis) of the extracted region of interest. Additional morphological operations and binarization enabled 3D rendering of retinal vasculature. As part of the algorithm, a function permitted the removal of objects below the selected threshold of 300 pixels (for each iteration along the antero-posterior axis).

a   **b**   **c**
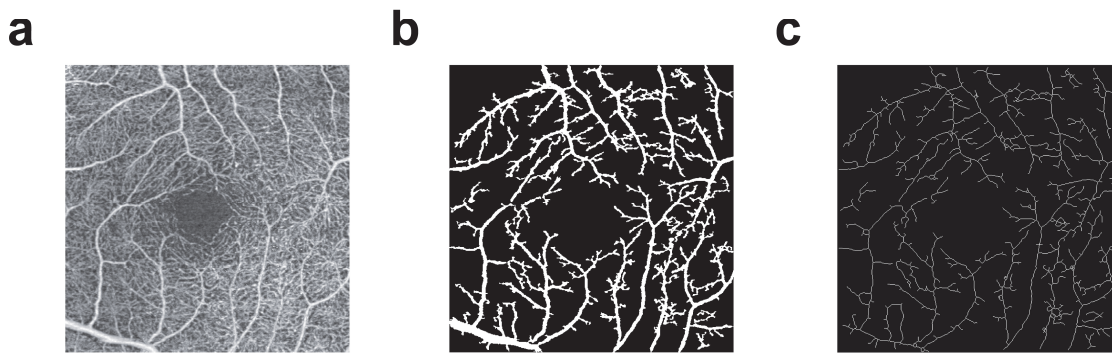
Figure 3-5 En-face view of the steps of the projection resolved algorithm and network graph representation (a) En-face flow signal after implementation of the projection resolved algorithm and dilation. (b) Segmentation and binarization of the projection resolved and dilated vessels. (c) Skeletonization of the vessels.

3.4.4 3D quantification

An angiography quantification approach involves the processing of a 3D binary voxel skeleton into a network graph described by nodes, endnodes, links and branches (links connected to endnodes) [98, 99]. The approach in [98] was applied to the skeletonized vessels for each OCTA scan, and the total number of nodes, links and branches were obtained from the network graphs.

3.5 Choriocapillaris (CC) flow voids quantification

To obtain measures from the CC, a 10 μm thick en-face CC slab was first isolated starting 8 μm deep into the choroid (posterior to the BM) and a maximum projection image of the slab was obtained. Even though it has been recommended to begin sampling the CC slab at greater depths

using a different device, the shallower selected depth offered CC images which visually most closely matched CC en-face images automatically generated by the device used. An algorithm capable of applying a Phansalkar adaptive local thresholding binarization filter [100] to the en-face maximum projection image from within the MATLAB environment was developed. The MATLAB Phansalkar function was adapted from the MATLAB implementation of the Sauvola binarization method [101]. The Sauvola local threshold is obtained over windows of a specified size using equation 3-4 below, where m(x, y) is the mean and s(x,y) the standard deviation of the pixel intensities with x and y as image coordinate. The variable R is the maximum standard deviation within a given window, and k is a constant.

$$T(x,y) = m(x,y)\left[1 + k\left(\frac{s(x,y)}{R}\right) - 1\right] \qquad (3\text{-}4)$$

Equation 3-5 below is used to obtain the Phansalkar local threshold. In the present implementation the threshold is computed over a window approximately 20 times smaller than the en-face image (consistent with the literature [37]). Unlike the ImageJ software Phansalkar filter used by Spaide [37] which features a circular window, the present MATLAB implemented filter derived from the Sauvola filter uses a square window. The added terms p and q were assigned the recommended values of 2 and 10 respectively, and the constant k the recommended value of 0.25 [100].

$$T(x,y) = m(x,y)\left[1 + pe^{-q \cdot m(x,y)} + k\left(\frac{s(x,y)}{R}\right) - 1\right] \qquad (3\text{-}5)$$

Like Phansalkar adaptive local thresholding, logarithmic binning of signal void sizes and the log number versus log size plotting were programmed directly into MATLAB. The fraction of signal voids greater than 10,000 μm^2 was calculated. The fraction of signal voids greater than 40,000 μm^2 was not used as it was found that most flow voids from non-exudative AMD eyes did not exceed that size. The slope, m, and the intercept, b, were obtained from the trendline of the log number versus log size plot. While the appearance of more continuous vessel segments may be realised and averaging may grant the possibility of studying alterations more precisely [38], a considerable number of scans are used to obtain superior results and there remains a risk of removing information. Owing to the lower feasibility of obtaining a fairly large number of scans (9 scans) per subject in a clinical setting, and yet unresolved uncertainty with regard to intrasubject en-face maximum projection images frame to frame changes after registration, averaging was not carried.

3.6 Drusen segmentation RPEb-BM and en face methods

As an implementation of the RPEb-BM drusen segmentation method, a thickness map was obtained as the difference between the BM and the RPEb. Then the value of each element of the resulting 2D array was compared with a threshold value corresponding to the addition of an absolute threshold of 12 µm and half the standard deviation of the 2D array values. Scan locations within the space between the RPE bottom and the BM where thickness values exceeded the threshold were given a value of 1, and in this way a volumetric binary drusen mask was obtained. The volumetric binary mask provided drusen volume measurements. A maximum projection of the volumetric binary mask into a 2D mask was used to provide drusen area measurements.

The en face drusen segmentation method using only the BM boundary [23] requires the application of several image processing steps. MATLAB implementations of the steps described in literature are available including top-hat filtering, median filtering and Jaccard similarity coefficient computation. A diagram of the modified pipeline is provided below.

Pre-processing

1. BM segmentation
2. Retinal flattening
3. Move up 8-35 µm from BM respectively
4. Move up 82-110 µm from BM respectively

Drusen segmentation

5. 3D mean filter & normalization
6. Inversion of outer slab
7. Dual-scale white Top-Hat transform
8. Thresholding

Post-processing

9. Continuity detection
10. Opening operation
11. Logical OR
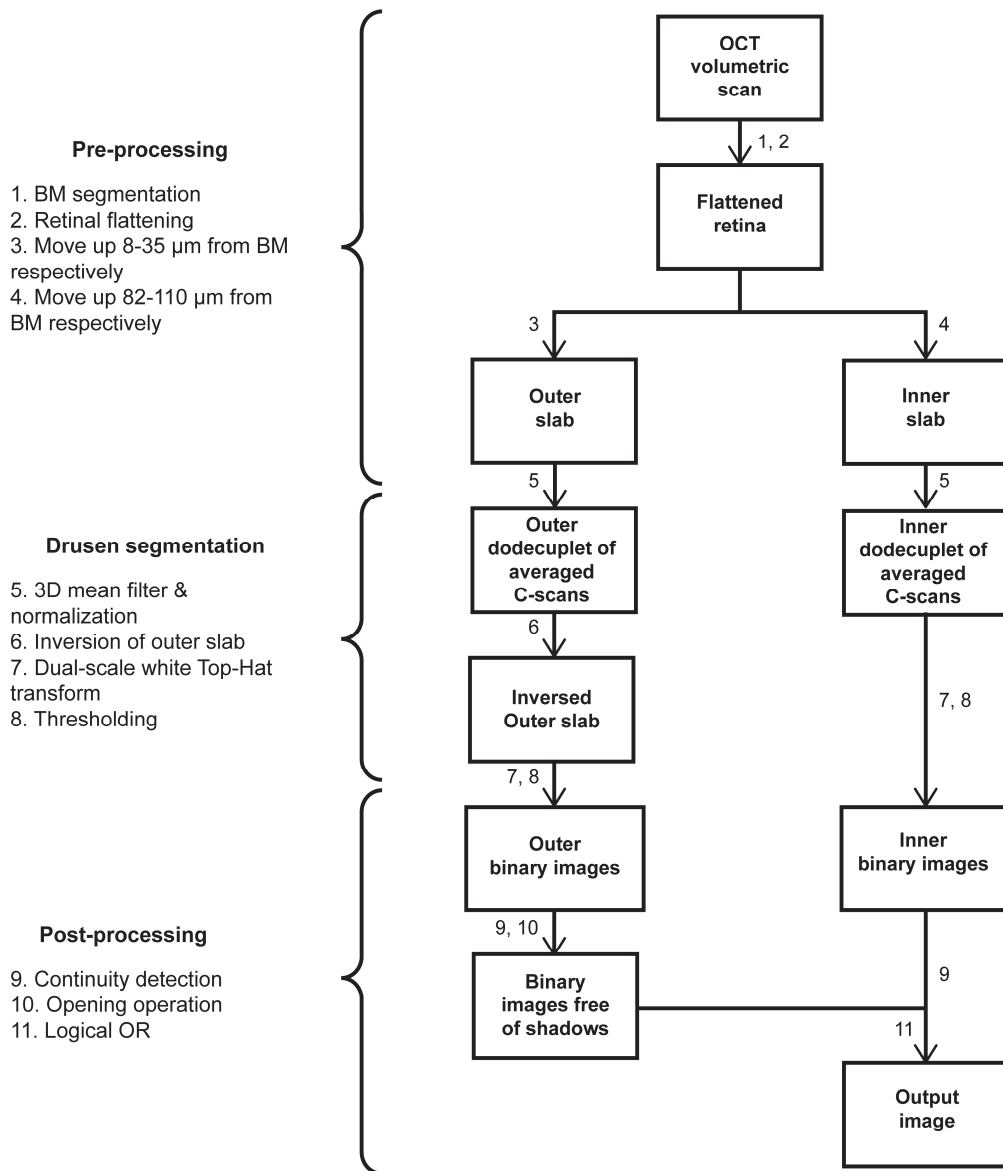
Figure 3-6 Diagram of the modified en face drusen segmentation method pipeline.

Owing to the greater resolution available with the device used, a greater number of C-scans were averaged than in the original method (dodecuplets instead of quintets, as shown in Figure 3-6 above). Otsu thresholding resulted in false positives when applied to control images. A set binarization threshold aimed at minimizing false positives in control images was chosen to replace Otsu binarization. Morphological operations were also added immediately after binarization and before the logical OR and median filtering steps to provide a more conservative segmented drusen area coverage.

Performance metrics were used to validate the segmentation methods against expert ground truth, namely the Jaccard index, J, and the Sørensen–Dice coefficient, D. Equations for the two metrics are provided below, where A and B are binary images evaluated for similarity.

$$J(A, B) \;=\; \frac{|A \cap B|}{|A \cup B|} \qquad\qquad (3\text{-}6)$$

$$D(A, B) \;=\; 2 \cdot \frac{|A \cap B|}{|A| + |B|} \qquad\qquad (3\text{-}7)$$

3.7 Spectral analysis

As the eye level (whole individual scan) quantification of the RPEb-BM space and CC flow voids showed significance with regard to discriminating control from AMD eyes and were represented most evenly across the frontal plane of subject eyes, a method to extract similar measures at the B-scan level was sought. Fourier transformation of spatial series was appealing due to the nature of the biomarkers of interest. Single line spatial series sampled along frontal plane images representative of the RPEb-BM space and CC were transformed into their frequency domain equivalent. For the RPEb-BM space, single line spatial series from the thickness map were used. For CC, single line spatial series from the maximum projection of the slab previously described (see section 3.5) were used.

The fast Fourier transform (FFT) is an algorithm which rapidly computes the discrete Fourier transform (DFT) [102] and a short explanation of Fourier transformation is provided in Appendix B. A MATLAB implementation of FFT was used to obtain the transform of spatial series representative of single lines along the RPEb-BM thickness map and CC.

In addition to smaller drusen, early and intermediate AMD eyes have been described as demonstrating medium drusen with widths of 63 μm and above [15]. As such, it was anticipated that for a given B-scan, drusen would manifest as a concentration of higher amplitudes than control in the lower frequency range of the spectrum. Likewise, it was expected that abnormalities such as flow voids, which vary greatly in size, would be represented across a broad frequency range of the spectrum representative of the CC.

3.8 Classification

Classification ML problems can be defined in terms of their typical workflow components. Initially, observations containing the information of interest have been gathered, and each observation has been labelled as belonging to one of the possible classes. In the project, observations are individual B-scans for each class as shown in the first row of Table 3-1. Observations from early and intermediate AMD B-scans were collectively labelled as AMD, and observations from normal B-scans were labelled as control. The class labels constitute ground truth.

Features are engineered from the observations and selected based on their ability to discriminate between classes (for example, using statistical methods as in the present project). For the project, RPEb-BM space and CC spectral data obtained using fast Fourier transform were combined into a joint feature space. Once features have been selected, the ones belonging to a small fraction of the observations are set aside. The remaining majority of observations including both classes of a dataset are fed to a ML algorithm and a classification model is generated. For validation, the generated model is then used to predict classes from features belonging to the smaller fraction of observations that was previously set aside. These last predictions are then compared against the ground truth classes corresponding to the same observations using a number of metrics. A typical classification ML workflow is shown in Figure 3-7 below.

Figure 3-7 Typical classification ML workflow.

3.8.1 Principal component analysis (PCA) dimensionality reduction

A low number of features belonging to each observation can be preferable to a high number of features. Reducing the number of features can help prevent error associated with using a number

of features which exceeds a critical value, a phenomenon known as the peaking phenomenon [103, 104]. The critical point beyond which error increases is believed to occur when the number of features is greater than half the number of observations. Thus, as part of a separate classification ML workflow to be evaluated, spectral data were allocated into frequency bands using PCA. The analysis of explained variance as a function of frequency revealed that in the instance of both drusen and CC representative spectrums, the percentage of explained variance diminishes as frequency increases. Plots of cumulative explained variance as a function of frequency are shown in Figure 3-8 below.
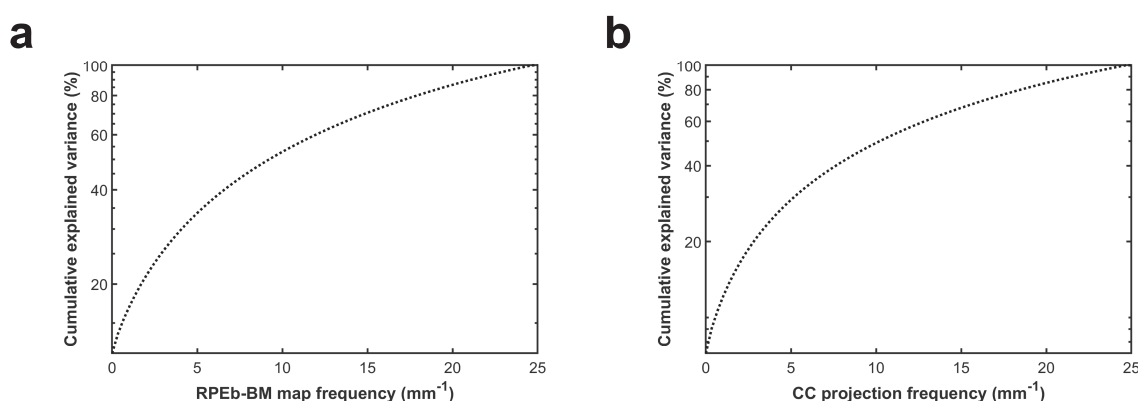
Figure 3-8 PCA cumulative explained variance as a function of frequency (a) RPEb-BM thickness map frequency dataset. (b) CC projection frequency dataset.

A strategy was developed to help maximize explained variance reflected in each band and to ensure that they collectively account for at least 95 percent of total explained variance [105]. A set of equations provided in Appendix C was used as part of an algorithm which allocates the average of a progressively greater number of frequencies into each band as frequency increases along the spectrum.

3.8.2 Random forest (RF)

The biomarker spectrums and constructed bands were used as input for training RF classification models. RF designates a type of ML algorithm which combines several decision trees into an ensemble model [50-52]. The trees are constructed in such a way as to maximize the model's ability to generalise from trends in a given dataset. Example diagrams of decision tree

representations with five classes are shown in Figure 3-9 below. The Pythagoras tree representation shown in Figure 3-9(b) is a type of fractal geometry [106] which can be useful for visualising hierarchies [107].
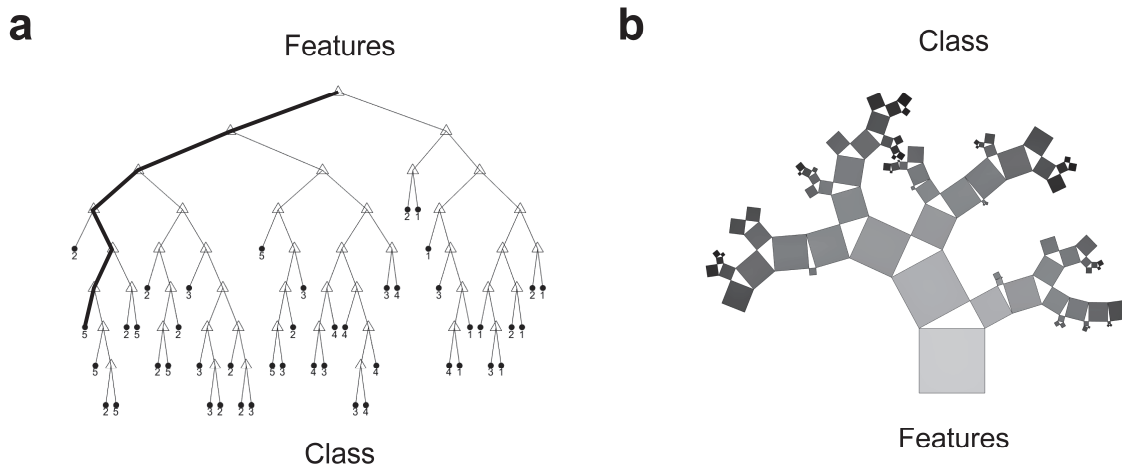
Figure 3-9 Hierarchical tree representations with five classes. (a) Node-link decision tree representation. (b) Pythagoras tree representation.

As shown in Figure 3-9, for a single tree trained model a prediction is made first by presenting the feature space corresponding to an observation at the entry node of the model. At each node of the tree, the feature space is subjected to a rule, e.g. P(5 mm^{-1}) $\geq$ 2 dB/mm^{-1}. Whether the features satisfy the rule determines the path down to the next level of the hierarchy and either one of two subsequent nodes until an end node (also called a leaf node) is reached and a class is assigned.

Rules are determined at tree construction during training with the majority of observations (assuming a small fraction has been set aside for validation). To construct a single tree, at the first node possible rules to split observations into two sub-groups are iterated until a rule is found which maximizes a measure of impurity gain. In the MATLAB implementation, the default impurity measure is Gini's diversity index, i_t. Equation 3-8 below defines Gini's diversity index. The term p_j represents the fraction of items labeled with value j in the set of C classes. The index takes a small value if p_j are near zero or one, indicating low impurity.

$$i_t = 1 - \sum_{j=1}^{C} p_j^2, \quad j \in 1, 2, \dots, C \qquad (3\text{-}8)$$

Impurity gain, ΔI, is calculated as,

$$\Delta I = i_t - \frac{N_L}{N} i_{t,L} - \frac{N_R}{N} i_{t,R} \qquad (3\text{-}9)$$

The terms $i_{t,L}$ and $i_{t,R}$ are the values of Gini's indexes for the left and right child nodes, respectively. The term N is the total number of observations in the parent node and N_L and N_R are the number of observations in each child node. The process is repeated at each node of a given tree until remaining observations are pure as defined by the index, or a specified maximum tree depth is reached. The Pythagoras tree, Figure 3-9(b), provides insight as to how trees are constructed. As squares around each node form a Pythagorean triple, the proportions of the two smaller sides of the right triangle reflect the optimal split. Optimal splitting paths along Pythagorean trees also indicate the course which any given input is most likely to undertake through to an end node. One such high probability path is drawn onto the node-link tree in Figure 3-9(a) for comparison.

In addition to aggregating trees into an ensemble model and yielding a consensus prediction, RF leverages tools which help prevent overfitting [85]. Bagging consists of sampling a subset of observations to construct each tree. In addition to bagging, as part of constructing a RF model only a subset of features is selected to determine how best to split observations at each node. A generic RF model structure is shown in Figure 3-10 below.
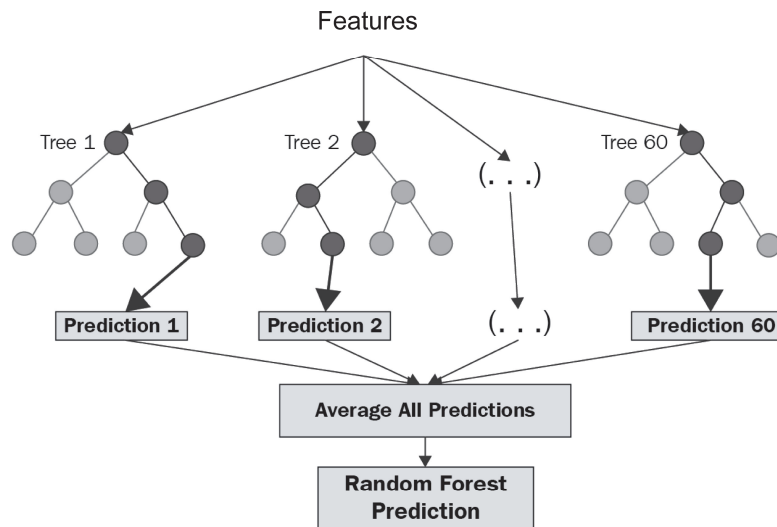
Figure 3-10 A generic random forest model featuring 60 trees (modified from [108]).

A hyperparameter is a model parameter with a value that is set before model training begins. By default, the MATLAB RF implementation grows deep trees and a maximum level after which splitting is prohibited was not specified. A number of 60 trees was specified for each model and it was determined that additional trees would not increase classification performance appreciably [109]. Unlike many other ML approaches, RF models provide a measure of predictor importance, and plots of predictor importance as a function of frequency and frequency bands were generated.

An implementation of an algorithm capable of generating Pythagorean forests in the MATLAB computing environment was also developed. The Pythagorean forest leverages the Pythagoras tree representation and offers a convenient means of displaying the structure of RF learned models [110].

3.8.3 Deep forest (DF)

In an effort to maximize classification performance, the cascade DF model [76, 111] was implemented in MATLAB and explored in addition to the simpler RF model. Deep forest models were designed to leverage characteristics of deep neural networks namely, layer-by-layer processing, in-model feature transformation and complexity, and combining those characteristics with forest models. A schematic of the DF cascade structure which was implemented is shown in Figure 3-11 below. As can be seen in the figure, the structure integrates forests in parallel, and in a series of layers. The cascade features both RF and a similar model called extremely randomized trees (ET) [112, 113]. Like RF, the ET model is an ensemble which joins together decision trees. However, unlike RF, all observations are used to grow each tree in the ensemble and the cut-point of candidate features at each node split is selected completely randomly before a rule is established which maximizes the measure of impurity gain. For the project, deep ETs were grown, and specified parameters were 60 trees per model and 20 features randomly selected at each node. As shown in Figure 3-11, the DF cascade is trained by feeding features as input to each forest in the first layer. In subsequent layers, the class distribution output array from each forest sub-model, which would normally be used to determine the output class, is concatenated with the original features and fed as input. Following the last level of parallel forests, an averaged class distribution array is obtained from individual sub-model outputs. The maximum of individual elements in the averaged class distribution array is used as the final classification. In the present implementation, three levels, N, were used.
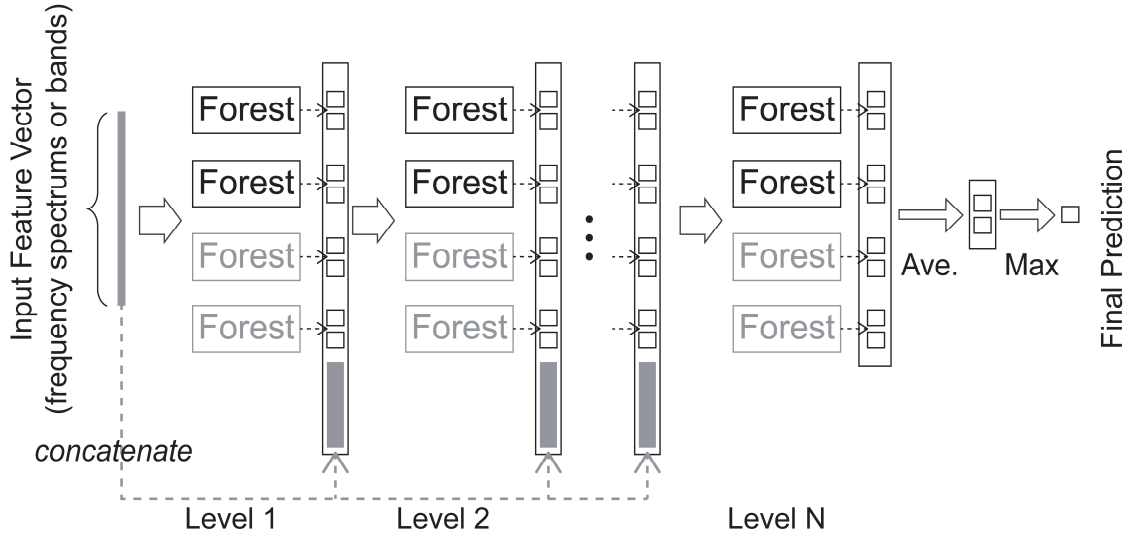
Figure 3-11 DF cascade structure. The model features both RF (represented in black) and ET (represented in grey).

3.8.4 Models performance evaluation

Performance metrics were used to evaluate the classification approaches namely sensitivity, specificity, precision, accuracy and F1-score. The different performance metrics are functions of the number of true and false positives (abbreviated TP and FP, respectively) and true and false negatives (abbreviated TN and FN, respectively).

$$sensitivity \ = \ \frac{TP}{TP+FN} \qquad\qquad (3\text{-}10)$$

$$specificity \ = \ \frac{TN}{FP+TN} \qquad\qquad (3\text{-}11)$$

$$precision \ = \ \frac{TP}{TP+FP} \qquad\qquad (3\text{-}12)$$

$$accuracy \ = \ \frac{TP+TN}{TP+TN+FP+FN} \qquad\qquad (3\text{-}13)$$

$$F1-score \ = \ 2 \cdot \frac{precision \cdot sensitivity}{precision+sensitivity} \qquad\qquad (3\text{-}14)$$

The metrics were evaluated on datasets corresponding to two conditions. The first datasets were folds of a k-fold cross validation scheme (ten-fold for RF and three-fold for DF). In the k-fold

cross validation, 10 % of observations were determined randomly and set aside iteratively for testing. The datasets associated with the second condition were obtained by iteratively leaving all B-scans belonging to all eyes from a given subject (an augmented 600-1200 B-scans) out of the training dataset, and then testing the models on those same B-scans.

CHAPTER 4   RESULTS

In this section the results for key steps of the research project as outlined in section 2.5 are provided. In the first part, results are displayed and described at eye level for each of the five feature extraction methods. Eye level results are followed by a comparison between the extracted features for early and intermediate AMD subjects against control subjects. For each feature, strip charts are used to compare the two groups, with lines at the means and Mann-Whitney U test outcomes above the data points using a p-value star system (* = $p \leq 0.05$, ** = $p \leq 0.01$, *** = $p \leq 0.001$) [114, 115]. The strip charts are accompanied by a 3D bar plot which summarizes test results across ETDRS subfields. The second part is concerned with spectral analysis applied to measures representative of drusen and CC flow void, and ML using the extracted features. The generated models and their performance are described.

4.1 Retinal thickness map

Results from the RVI and BM segmentation for a control subject and an AMD subject are shown in Figure 4-1 below. The figure shows B-scans with segmentation lines and a thickness map with pink indicating a relatively greater retinal space and blue a relatively narrower retinal space. At eye level, distinctions can be observed between the control subject and the AMD subject's results. Notably, the control subject's thickness map suggests a thicker retina along the pericentral annulus and an overall flatter retina in the case of the AMD subject. For the AMD subject, the scan is slightly lower quality which is reflected in the rough appearance of the thickness map's surface and the presence of straight lines parallel to the slow scan direction.

The strip charts showing retinal thickness and retinal volume data between the two groups is shown in Figure 4-2. For the present dataset, thickness highest significance was found at the superior subfield, and volume highest significance was found at the temporal subfield ($p \leq 0.01$, Mann-Whitney U test). Central measures were similar across groups. Perhaps, structural changes associated with AMD such as the presence of drusen are a contributing factor to the similar central measures.
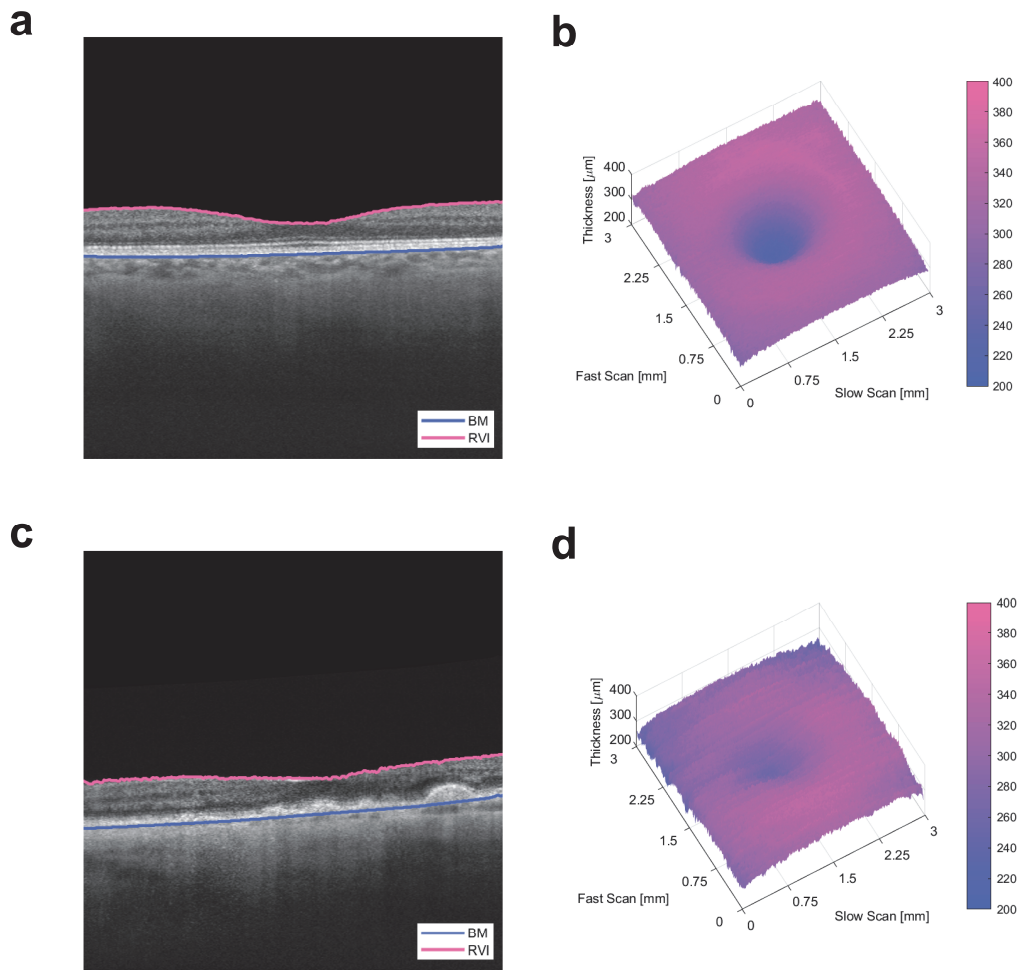
Figure 4-1 B-scan RVI segmentation and BM segmentation at macula and whole eye thickness map for a control subject (top) and an AMD subject (bottom). (a, c) B-scan image. A pink segmentation line is traced along the RVI and a blue segmentation line is traced along the BM. (b, d) Thickness map. For all locations along the plane and according to the range of the scale, pink indicates a greater retinal space and blue a narrower retinal space.
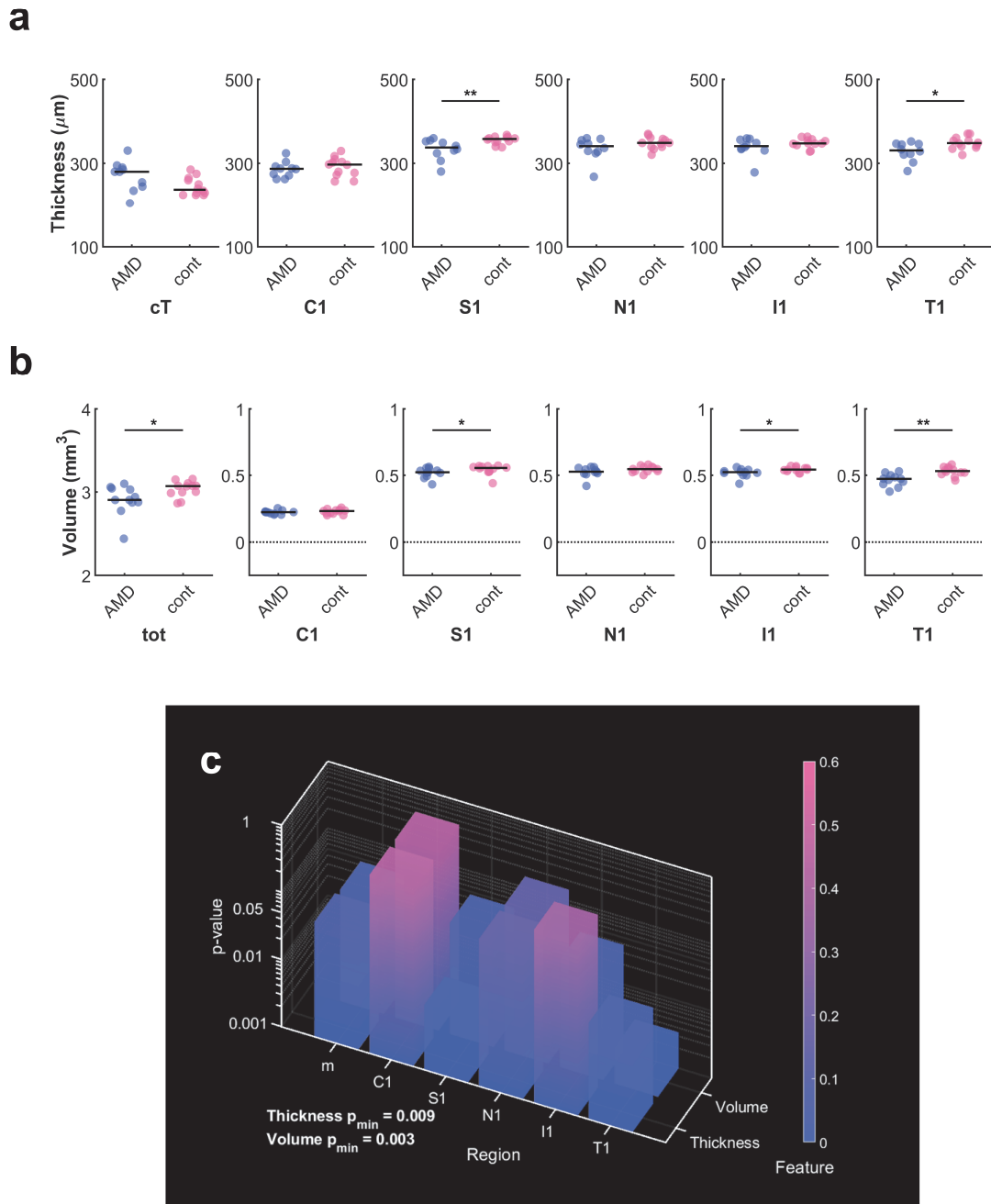
Figure 4-2 (a) Retinal thickness distributions versus ETDRS regions for AMD and control subjects (b) Retinal volume distributions versus ETDRS regions for AMD and control subjects (c) Comparison of p-values from Mann–Whitney U test for retinal thickness and volume, and between AMD and control distributions

4.2 Retinal capillaries plexus (RCP) network graph

A set of 3D rendered images corresponding to the RCP in situ flow signal, shadowgraphic flow projection artifacts correction, larger vessels segmentation and skeletonization for one eye of a control subject are shown in Figure 4-3(a-d). Results from the network graph generation for the same eye are shown in Figure 4-3(e). At eye level, it can be seen from Figure 4-3(b) that relatively smaller retinal vessels are not well resolved even after shadowgraphic flow projection artifacts correction. As seen in Figure 4-3(c) and also in en face Figure 3-5(b), vessels segmentation results suggest that the isolation of relatively larger vessels for subsequent skeletonization was successful. As Figure 4-3(d) and other individual skeletonization images suggested, morphological dilation of the projection resolved flow signal is not enough for overcoming data sparsity especially with regard to larger vessels. This resulted in areas with artificially higher skeleton density or duplication of skeletons along larger vessels. The network graph in Figure 4-3(e) successfully shows nodes and links corresponding to the skeleton.

The strip charts showing node and links data between the two groups are shown in Figure 4-4. For the dataset, the number of nodes and links and test significance levels were very similar across subfields. Notably, the temporal subfield showed highest significance for both links and nodes (p ≤ 0.001 and p ≤ 0.01, respectively, Mann-Whitney U test). Interestingly, center measurements of links and nodes represent a similar yet alternative measure to foveal avascular zone. A recent investigation found no significant difference in foveal avascular zone measurements between intermediate AMD subjects and control eyes [116], which does not appear consistent with the central subfield results.

To test repeatability of the method repeated scans from both eyes were obtained from a subject with a prior ocular surgery for retinal detachment in the right eye and otherwise normal eyes, and one eye from a subject with neovascular AMD. Strip charts showing node and links data for repeated scans of the control eyes and the neovascular AMD eye are shown in Appendix D. Retinal thickness and volume data, as well as raw OCTA en-face images and network graphs for the control's left eye and the neovascular AMD eye are also provided.
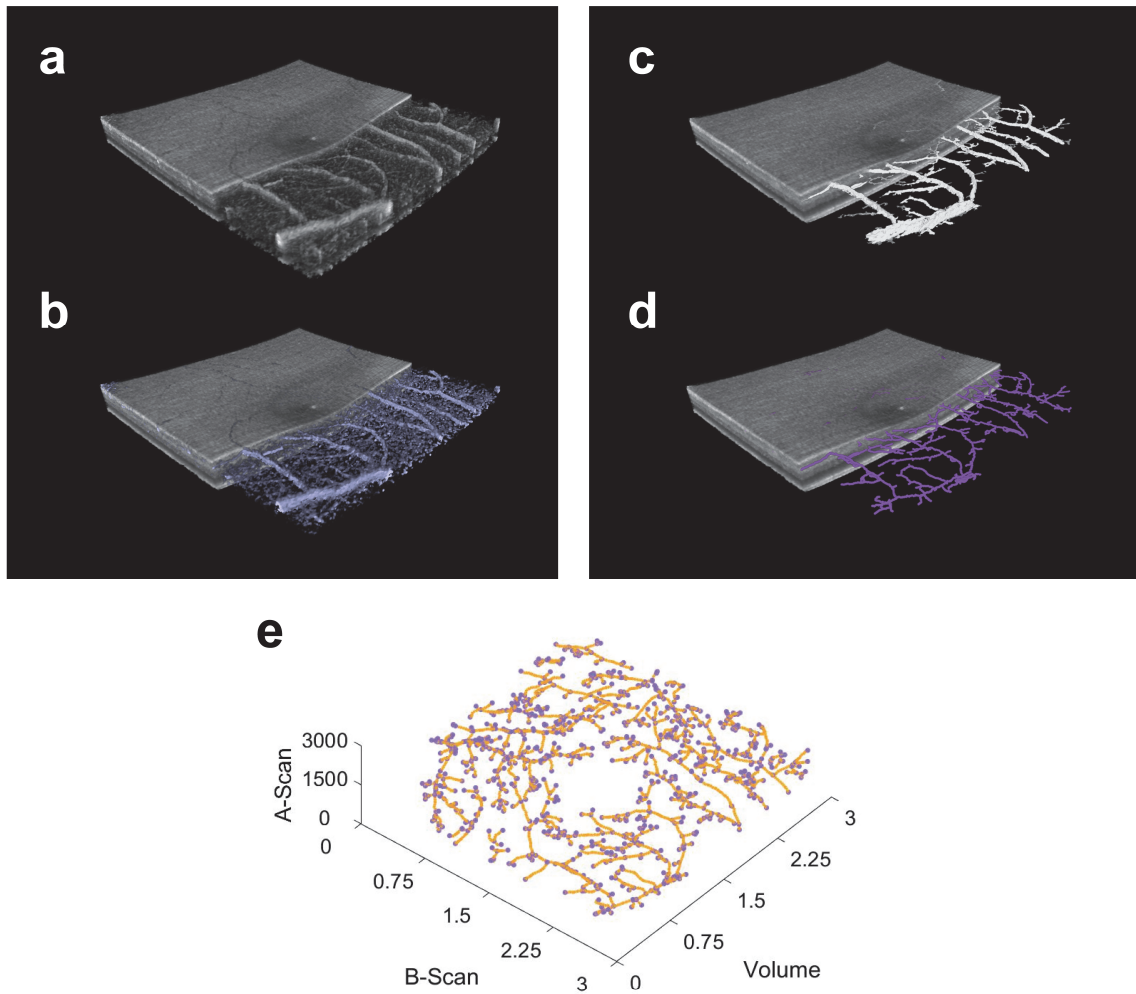
Figure 4-3 Vessels network graph construction steps with superimposed structural signal volume and isolation of the retinal space. (a) 3D rendered in situ decorrelation signal volume. (b) Decorrelation signal volume after implementation of the projection resolved algorithm and dilation. (c) Projection resolved vessels following segmentation and binarization. (d) Skeletonization of the segmented binary vessels. (e) Vessels network graph.
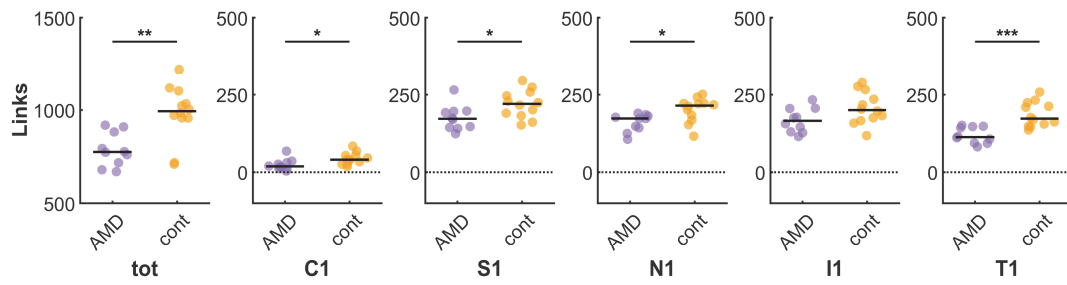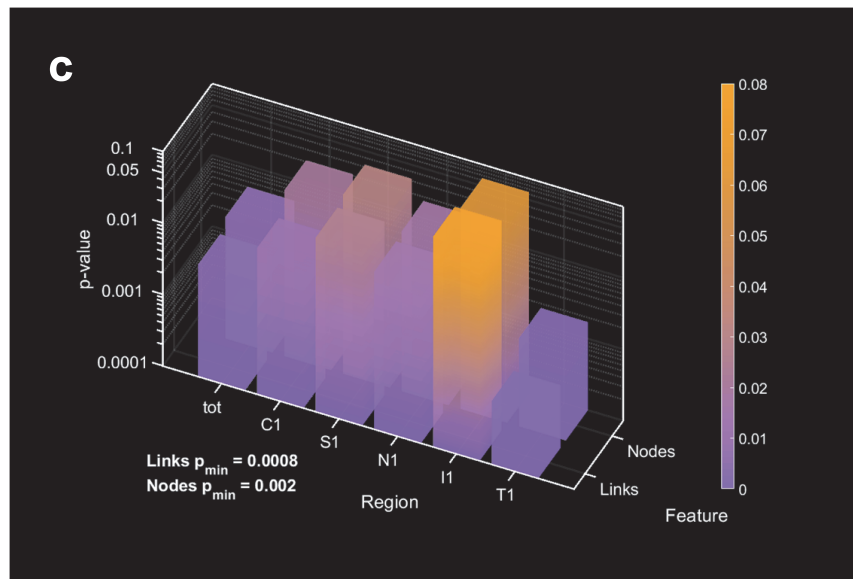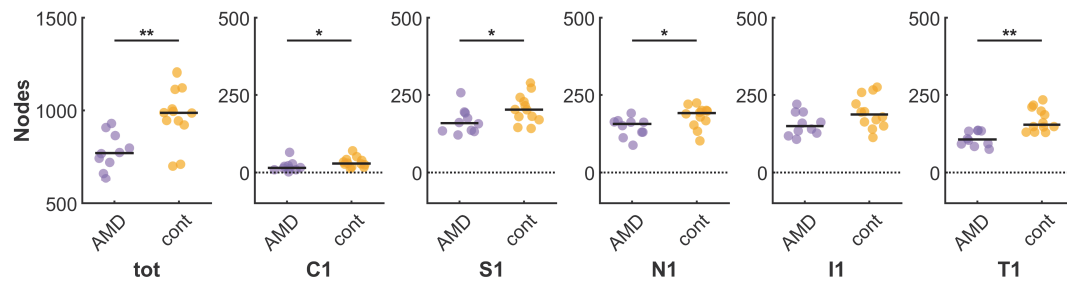
Figure 4-4 (a) Network graph links distributions versus ETDRS regions for AMD and normal subjects (b) Network graph nodes distributions versus ETDRS regions for AMD and normal subjects (c) Comparison of p-values from Mann–Whitney U test for network graph links and nodes, and between AMD and normal distributions.

4.3 Choriocapillaris (CC) flow voids analysis

Results from the isolation of a CC slab, its maximum projection image and the corresponding Phansalkar adaptive local thresholding binary mask are shown for a control subject and an AMD subject in Figure 4-5(a) below. Bar and log-log plots featuring the number of flow voids against area size for the same subjects are also shown in Figure 4-5(b) and Figure 4-5(c), respectively. As shown in Figure 4-5(a), localised darkened areas are readily visible across the surface of the AMD CC slab maximum projection image in comparison with the control image. Likewise, larger flow voids, as represented by white areas are clearly visible and widespread on the AMD eye's Phansalkar binary mask when compared with the control eye. The bar plots suggest a power distribution for both subjects as anticipated. Trendline parameters reflect the relationship between the number of flow voids corresponding to each area size. In the case of the AMD eye, a lower number of small voids and a greater number of larger voids translates to a trendline with a slope that is less steep, and a lower trendline intercept.

The strip charts showing trendline intercept, slope and fraction of flow voids exceeding 10,000 μm^2 (FV10000) over the total eye surface for eyes belonging to the two groups are shown in Figure 4-6(a) below. The 3D bar plot in Figure 4-6(b) provides additional significance values for the remaining subfields. As the strip charts shows, all features showed significant differences between the two groups ($p \leq 0.05$, Mann-Whitney U test). In addition to being uniformly represented across the frontal plane of the eye, the 3D bar plot indicates that for FV10000 there remains significant differences across most subfields, further suggesting that CC quantification methods are a good candidate for B-scan level feature extraction. Results of flow voids quantification suggest that as had been demonstrated in literature, CC images can provide measurements which allow discrimination between diseased and healthy eyes.
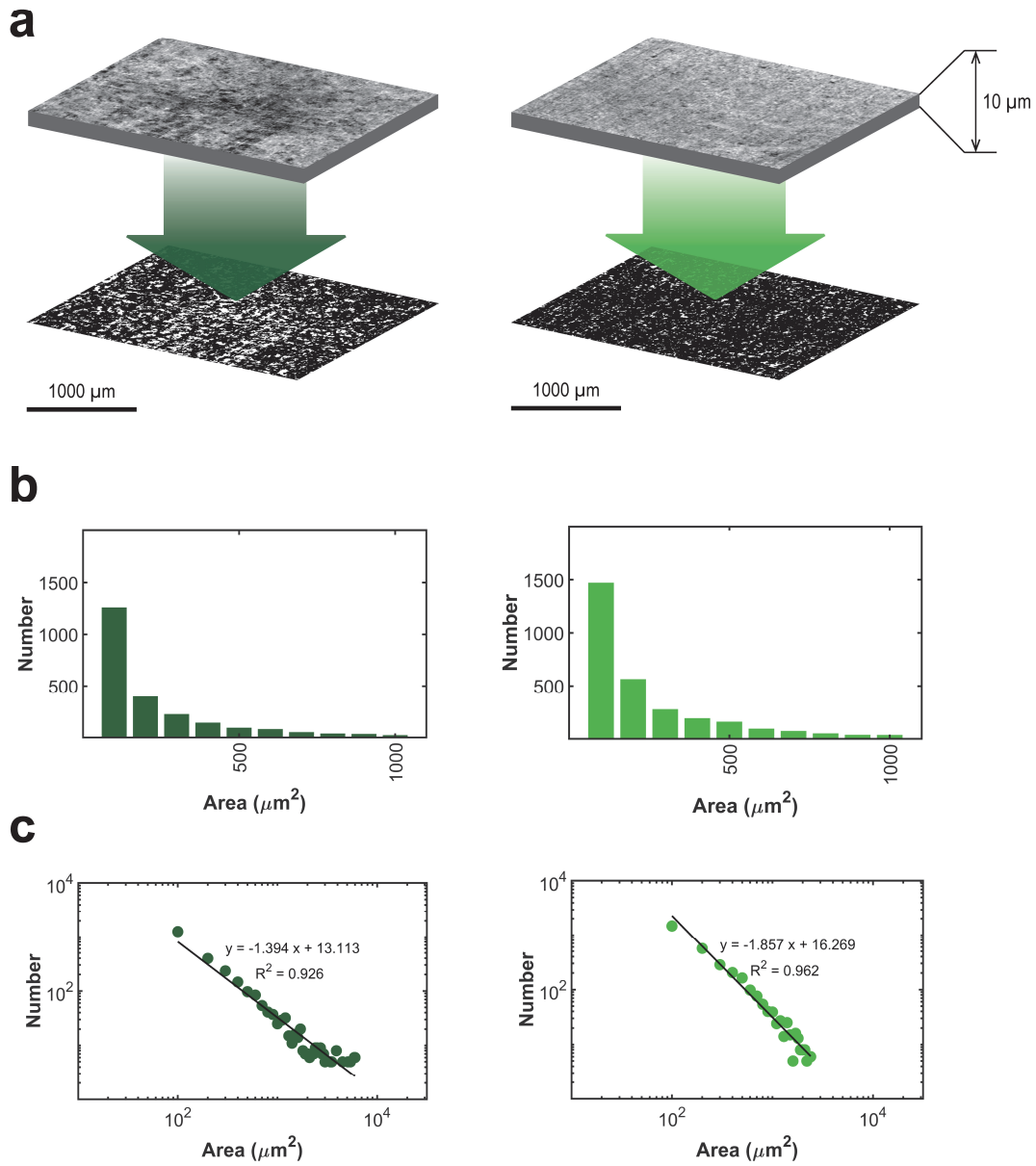
Figure 4-5 (a) AMD (left side) and control (right side) subjects flow voids parameters extraction steps; en-face CC slab maximum projection and Phansalkar local thresholding. (b) Bar plot showing number of flow voids binned into area sizes; the number flow voids with respect to area size follows a power distribution (c) Log-log plot of flow voids binned as a function of area; trendlines and parameters to be evaluated as biomarkers are shown.

a
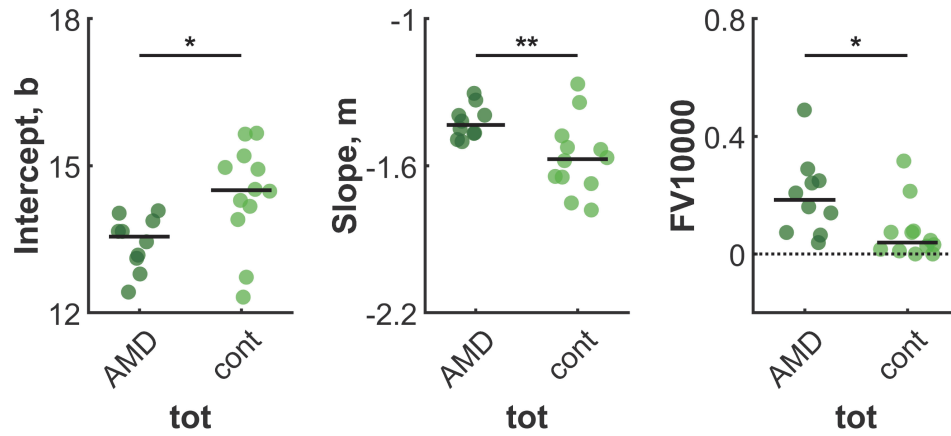
b
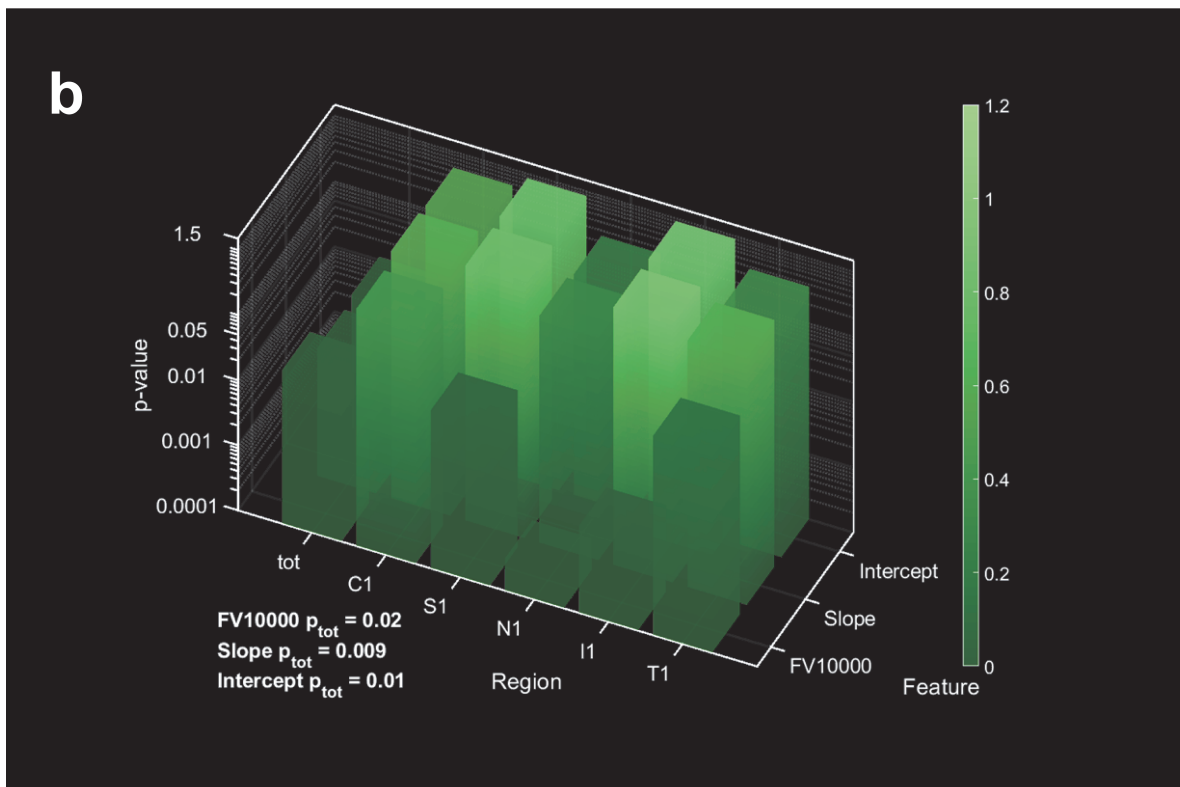
Figure 4-6 (a) Slope, m, intercept, b and signal voids greater than 10,000 μm² (FV10000) distributions for AMD and normal subjects and over the total area of the en-face binary image. (b) Comparison of p-values from Mann–Whitney U test for intercept, slope and FV10000 and between AMD and normal distributions.

4.4 RPEb-BM drusen segmentation method

The Figure 4-7(a) below shows a structural OCT B-scan with the BM (blue) and RPE (pale blue) segmentation lines for an AMD eye. In Figure 4-7(b), a closeup of the drusen segmentation mask of the space resulting from the subtraction of the RPE bottom layer from the BM layer is provided. Finally, a 3D rendering of the drusen map and the nasal projected ETDRS subfield are shown in Figure 4-7(c). The closeup of the binary mask suggests that for the given AMD eye, the thresholding strategy allowed keeping only regions where the RPE bottom was abnormally elevated. The drusen map in blue appears to correspond to visible areas of drusen along the lower boundary of the superimposed structural signal volume in Figure 4-7(c). For the AMD eye and as can be seen on the B-scan in Figure 4-7(a), drusen limits are not well defined and segmentation lines do not match the elevations exactly.

The strip charts showing drusen area and volume over the total eye surface for eyes belonging to the two groups are shown in Figure 4-8(a) below. The 3D bar plot in Figure 4-8(b) provides additional significance values for the remaining subfields. As the strip charts indicate, all features showed significant differences between the two groups ($p \leq 0.001$, Mann-Whitney U test). Like with flow voids quantification, the 3D bar plot indicates that for both area and volume, significance remains low across almost all subfields, suggesting that the first drusen method is a good candidate for B-scan level feature extraction.
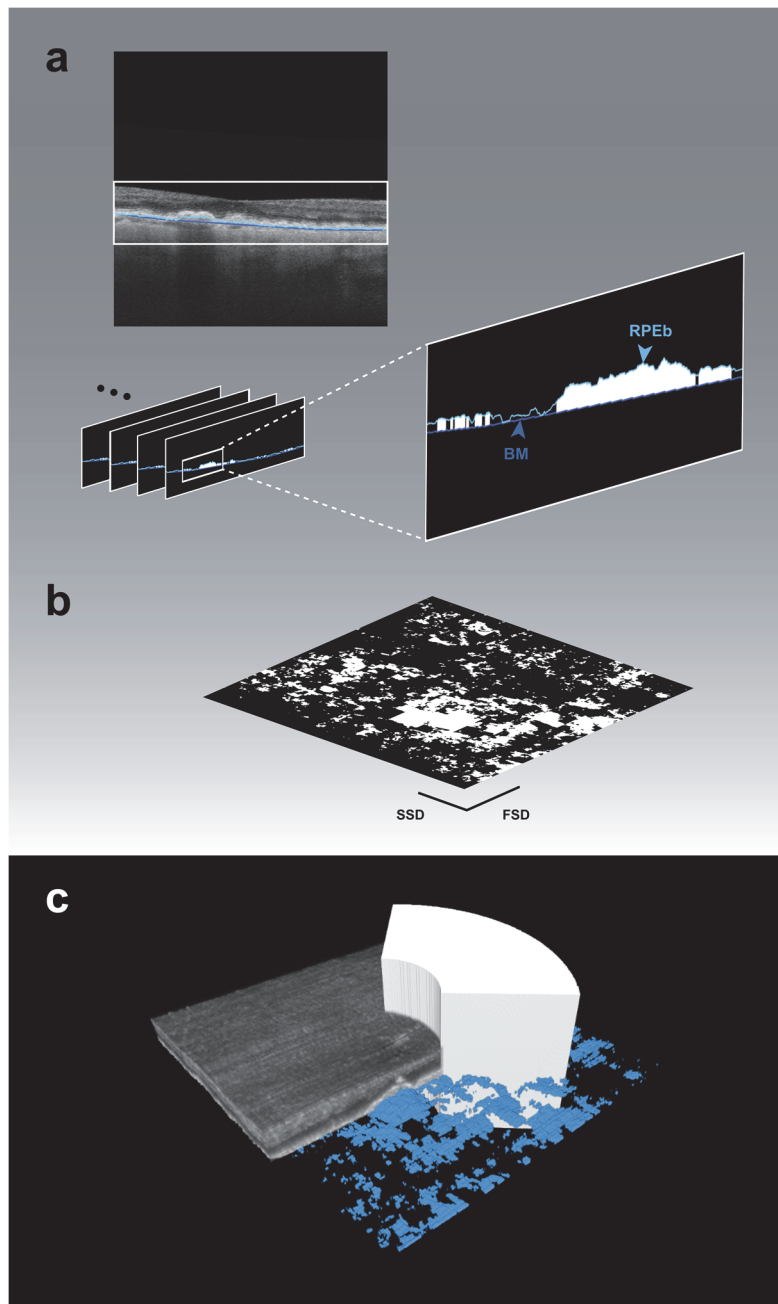
Figure 4-7 (a, top) B-scan structural OCT, BM (blue) and RPE (pale blue) segmentation lines for a female AMD subject. (a, bottom) RPEb subtracted from BM drusen segmentation mask with BM (blue) and RPE (pale blue) segmentations; closeup of BM subtracted from RPEb drusen segmentation mask. (b) Binary drusen segmentation mask en-face view. (c) 3D rendering of drusen map and ETDRS region.
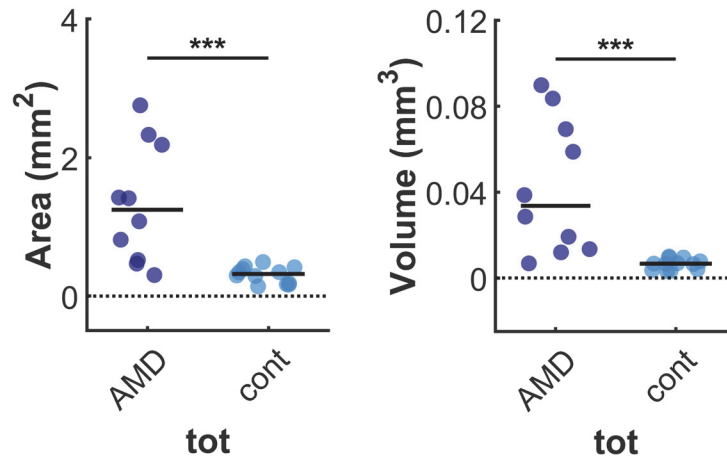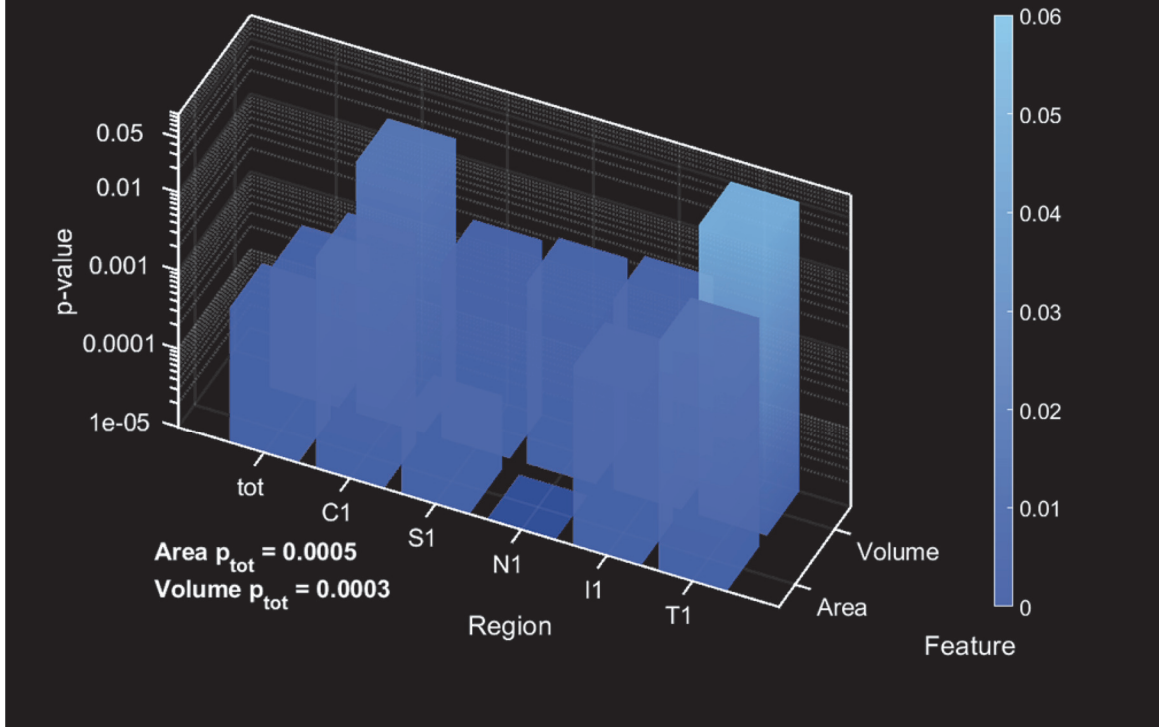
Figure 4-8 (a) Drusen area and volume distributions for AMD and control subjects and over the total area of the en-face binary image. (b) Comparison of p-values from Mann–Whitney U test for drusen area and volume and between AMD and control distributions.

4.5 En face drusen segmentation method

A diagram showing different types of drusen is shown in Figure 4-9(a) below. Underneath it in Figure 4-9(b), a B-scan belonging to an AMD eye is shown for comparison, with drusen segmentation inner slab boundaries represented as pink lines, and outer slab boundaries represented as red lines. A closeup of the boundaries corresponding to the white frame in the B-scan image is also provided.

The strip chart in Figure 4-10(a) shows drusen area over the total eye surface for eyes belonging to the two groups. The 3D bar plot in Figure 4-10(b) provides additional significance values for the remaining subfields. As indicated by the strip chart and 3D bar plot, results suggest that drusen area measurements in AMD eyes obtained trough the second drusen segmentation are generally not significantly different from those corresponding to control eyes. Despite the trend, significance was found in the nasal subfield ($p \leq 0.05$, Mann-Whitney U test). Lack of significant differences between groups for the method are attributed to the observation that by its nature the method is susceptible to segmenting vessels as they appear in OCT structural images. In the absence of further processing, vessels were occasionally wrongly included in the drusen area measurements. In addition to vessels, slightly raised RPE inner boundary in AMD and control eyes occasionally crossed inner slab limits and were also wrongly included in the drusen area measurements. Because of lower performance likely caused in part by vessels and raised RPE inner boundaries, the en face drusen segmentation method was deemed inferior to the RPEb-BM method.

A figure showing segmentation results as en face binary masks and a table providing segmentation performance for both drusen segmentation methods compared with two expert ground truth segmentations is provided in Appendix E for eight AMD eyes. Full tabulated results for the RPEb-BM drusen segmentation method are also provided. To generate ground truth images, experts identified drusen on C-scans structural OCT images extracted from the inner and outer slabs of each of the eight AMD eyes.
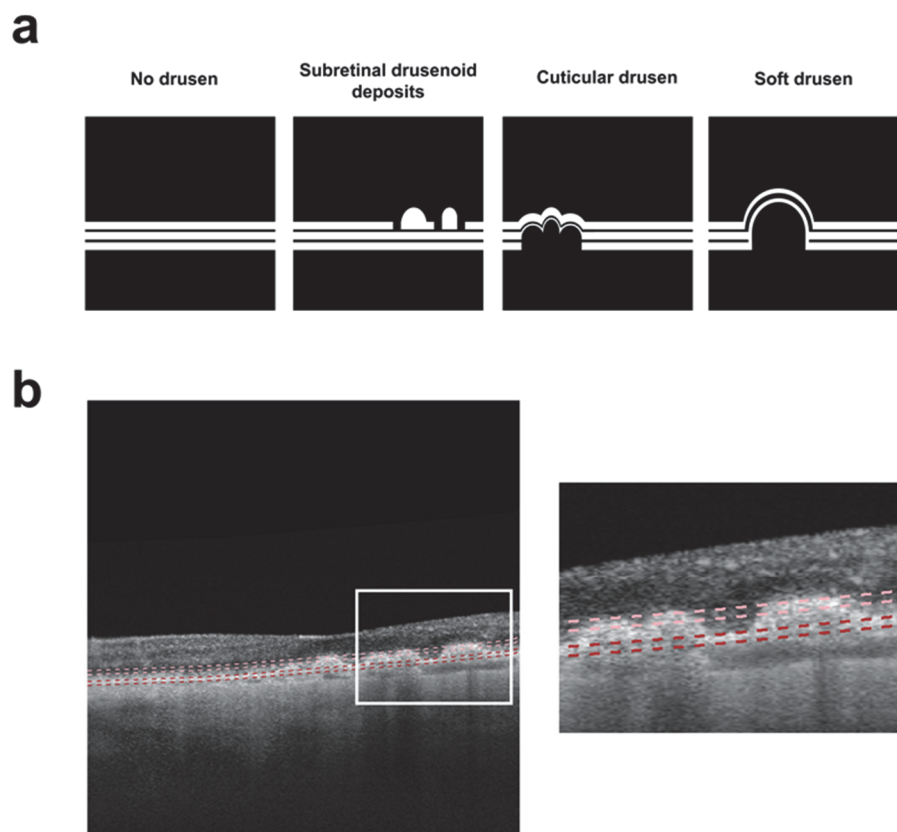
Figure 4-9 (a) Schematics of drusen types and their morphologies in the outer retina (modified from [11]) (b, left) B-scan with drusen segmentation inner slab boundaries represented as pink lines, and outer slab boundaries represented as red lines. (b, right) Closeup of the boundaries corresponding to the white frame in the B-scan image.
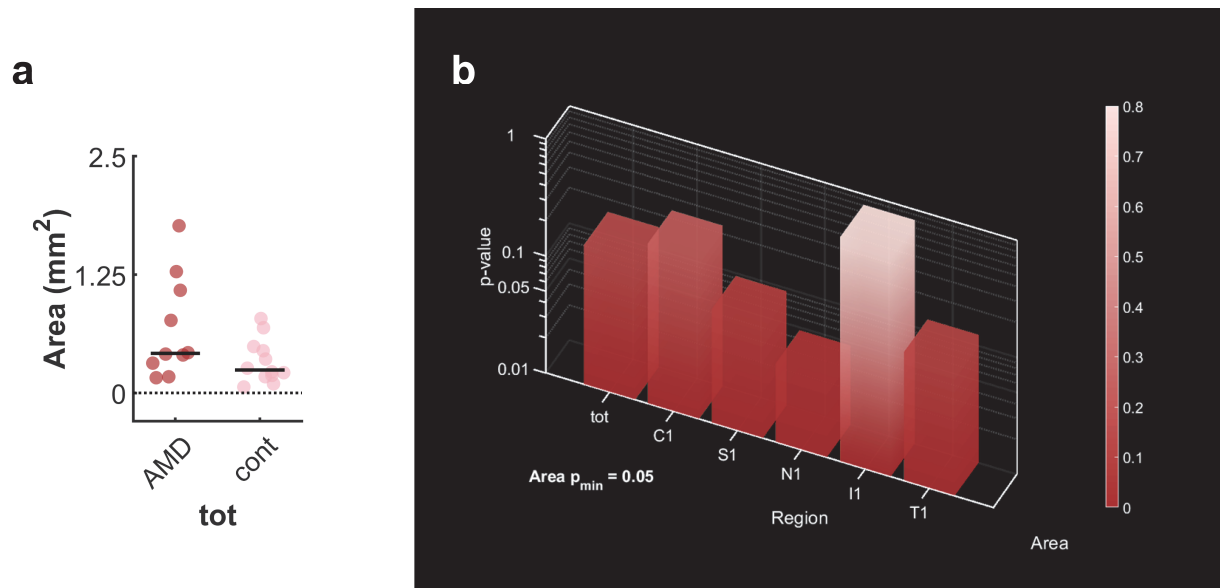
Figure 4-10 (a) Drusen area distributions for AMD and control subjects and over the total area of the en-face binary image. (b) Comparison of p-values from Mann–Whitney U test for drusen area between AMD and control distributions.

4.6 Spectral analysis and dimensionality reduction

Steps for splitting the RPEb-BM drusen thickness map and the CC slab flow signal maximum projection from an AMD eye into individual spatial series corresponding to each B-scan location along the fast scan direction are shown in Figure 4-11 below. As can also be seen beneath the spatial series belonging to each biomarker representative image, the Fourier transform of each series is obtained before it is converted to log scale for convenient visualisation.

The combination of the spectrums corresponding to both spatial series in the feature space is illustrated for one B-scan of the same AMD eye in Figure 4-12. For consistency with the transverse resolution of the device of 20 μm, the upper limit of the frequency spectrums was set to 25 mm^{-1}. Under the combined spectrums and as informed by PCA, the bands resulting from averages of a progressively greater number of frequencies as frequency increases along the spectrums are also shown. Spectrums from the CC slab flow signal maximum projection have lower amplitudes than those from the RPEb-BM drusen thickness map. In both instances the amplitude of the first element of the spectrum array is relatively higher than that of the other frequency terms, and is a reflection of the zero frequency term which does not vary with space [117].

The Figure 4-13 shows 2-D embedding plots of the transforms of the series representative of drusen and CC for both the control and AMD groups obtained using t-distributed stochastic neighbor embedding. As the name implies, t-distributed stochastic neighbor embedding is a ML technique which allows the visualisation of high dimensional data into a lower dimensional space. The average of all spectrums from all drusen thickness maps and all CC flow voids projection images of AMD and controls are shown in Figure 4-14(a) and Figure 4-14(c), respectively. In both figures, average spectrums belonging to controls are displayed in a lighter color, and average spectrums belonging to AMD eyes are in a darker color. Limits corresponding to the first and third quartiles are also shown as bounded lines. Similarly, bands distribution for the full control and AMD datasets are shown separately for each group in Figure 4-14(b) and Figure 4-14(d) as violin plots [118] with a consistent color scheme.

As anticipated, spectrums representative of the RPEb-BM in Figure 4-14(a) appear to diverge in the low frequency range. This is also observable when comparing the first few bands distribution between the AMD group and the control group. In the case of the CC average spectrums in Figure 4-14(c), differences between the spectrums are less noticeable and more evenly spread across the

frequency range which is likely a reflection of the presence of flow voids of various sizes. The slightly more apparent divergence in the lower frequency range of CC representative spectrums and bands is likely at least partly a result of drusen shadowing over the CC layer.
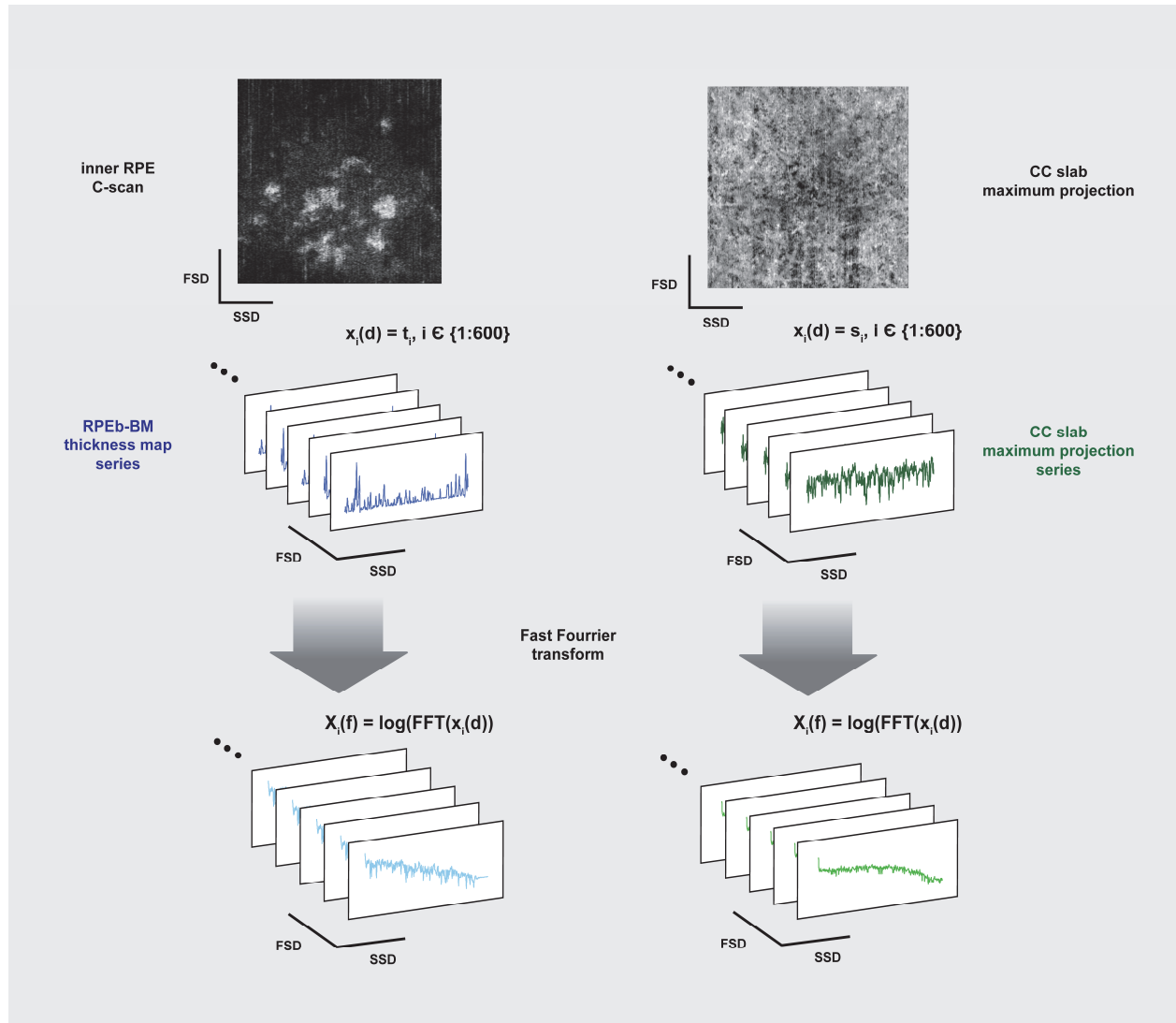
Figure 4-11 (top left) Inner RPE C-scan. (top right) CC slab flow signal maximum projection (middle) Biomarker representative images (RPEb-BM in blue, CC in green) are split into individual spatial series corresponding to each B-scan location along the fast scan direction. (bottom) The Fourier transform of each spatial series is obtained before it is converted to log scale for convenient visualisation.
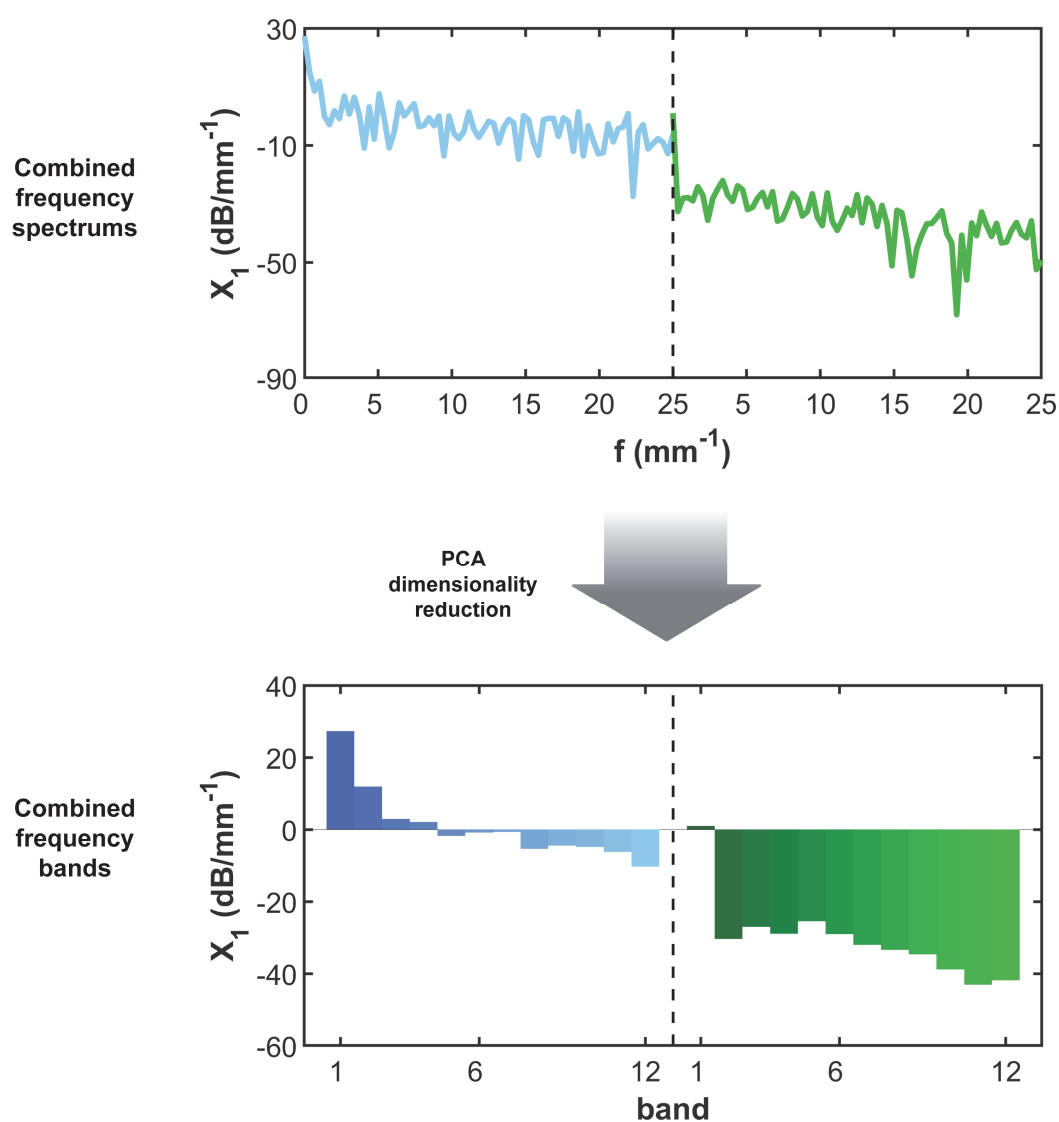
Figure 4-12 (top) Feature space for one spatial series which consists of the spectrums for both the series from the drusen thickness map and flow voids projection image (bottom) Principal component analysis was used to split each spectrum into 12 individual representative bands, with the goal of maximizing explained variance.
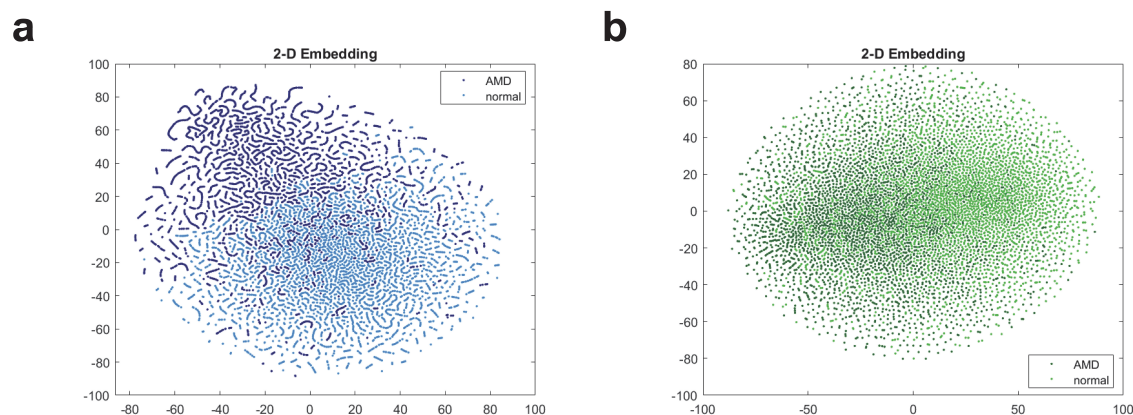
Figure 4-13 t-distributed stochastic neighbor embedding (t-SNE) of spectrums representative of biomarkers belonging to AMD and control groups (darker and lighter dots, respectively). (a) For series from the RPEb-BM thickness map in blue and (b) from the CC projection image in green.
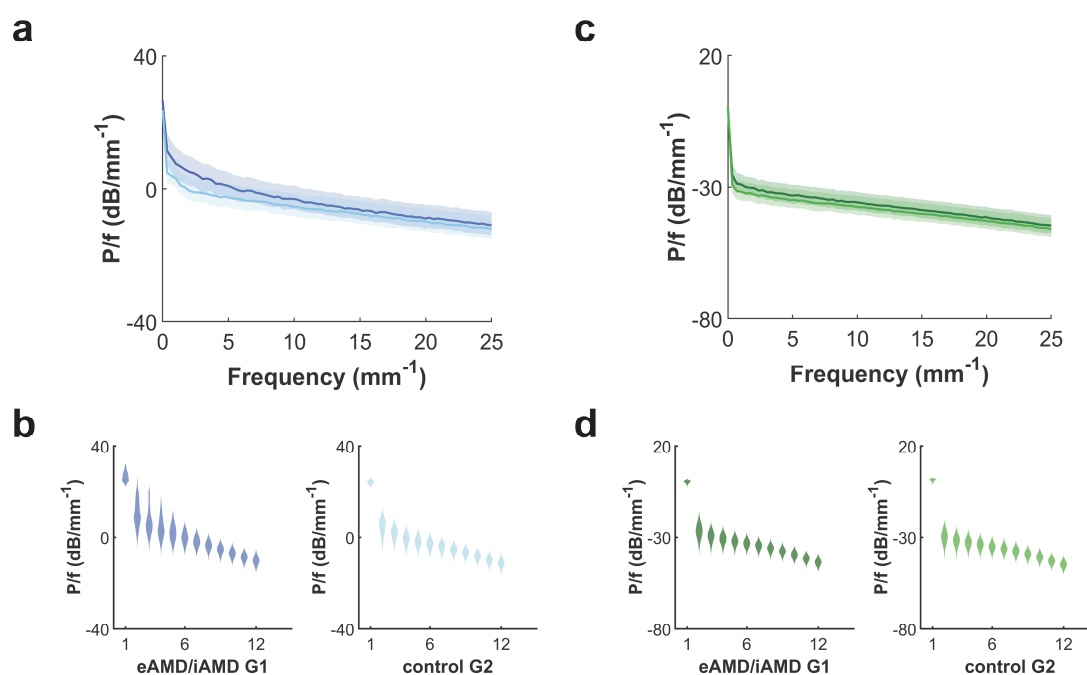
Figure 4-14 RPEb-BM thickness map and CC flow voids projection image spectrums from spatial series, and PCA optimized bands dataset representations shown in blue and green respectively. (a, c) Average spectrums for the full AMD (darker color) and control (lighter color) datasets with first and third quartiles shown as bounded lines. (b, d) Bands distribution for the full AMD and control datasets.

4.7 Classification

The Table 4-1 and Table 4-2 below provide performance evaluations of AMD classification based on frequency spectrums and bands, respectively. The tables include DF three-fold and RF ten-fold cross-validation average performance metrics and leave-one-subject-out per eye performance metrics. The AMD classification models were generated with data from similar age controls (labelled G2, over the age of 50) for DF and RF and also controls under the age of 50 (labelled G3) for RF. Results from spectrum and bands-based classification of AMD versus similar age controls suggest that good B-scan level performance was achieved, with a maximum accuracy of 95.51 % for spectrum-based classification and 93.23 % for bands-based classification. In both spectrum and bands-based classification with similar age controls, a lower performance is observed for leave-one-out validation (maximum accuracy of 77.27 %).

Full RF bands-based classification leave-one-subject-out validation results, as well as RPEb-BM drusen segmentation method and flow voids quantification results for AMD and similar age controls are provided in Appendix F. Looking at the leave-one-subject-out validation results more closely, three eyes in the AMD group and two eyes from the control group were misclassified (by B-scan accuracy rounding to whole scan binary classification). Drusen segmentation and flow voids quantification results suggest that the misclassified eyes represent subtypes within each group. The three misclassified eyes in the AMD group have the lowest drusen area (little to no drusen) when compared to other AMD eyes. The two misclassified eyes in the similar age control group show the highest fraction of flow voids exceeding 10,000 μm^2 when compared to the other control eyes (which all show relatively low fractions). As anticipated, results from spectrum-based and bands-based classification of AMD versus controls under the age of 50 years old indicate that the models could successfully distinguish B-scans and eyes belonging to each group.

Plots of predictor importance as a function of frequency for one-fold of the ten-fold cross-validation for both spectrum-based and bands-based classifications using RF are shown in Figure 4-15. As could have been expected based on the bounded line plots in Figure 4-14, the predictor importance plots for the drusen thickness map frequency spectrum and bands indicate that lower frequencies (especially in the < 10 mm^{-1} range) were the most important predictors for reaching a classification. Predictor importance for CC flow voids projection image frequency spectrum and bands show that importance is spread almost evenly across the spectrum.

Hierarchical representations of the random forest models for spectrums and bands are provided in Figure 4-16 and Figure 4-17, respectively. As can be visualised in the figures, dimensionality is reflected in tree morphologies. The average lower probability split at each node, $\bar{s}_L$, of the high dimensional trees in Figure 4-16 is less than the average for low dimensional trees. The average depth, $\bar{d}$, of the high-dimensional trees is greater than the average depth of the PCA optimised low-dimensional trees.

Table 4-1 Performance evaluation for spectrum-based early and intermediate AMD classification. DF three-fold cross-validation and RF ten-fold cross-validation average performance metrics and leave-one-subject-out per eye performance.

Subject groups (Model)	Number of observations (Type)	Frequency spectrum-based results (%)				
		Sensitivity	Specificity	Precision	Accuracy	F1-score
AMD-cont G2 (DF)	13200 (B-scan)	92.61	97.92	97.40	95.51	94.92
AMD-cont G2 (DF)	22 (Eye)	70.00	83.33	77.78	77.27	73.68
AMD-cont G2 (RF)	13200 (B-scan)	90.92	96.58	95.68	94.01	93.24
AMD-cont G2 (RF)	22 (Eye)	70.00	83.33	77.78	77.27	73.68
AMD-cont G3 (RF)	12600 (B-scan)	98.12	98.72	98.60	98.44	98.35
AMD-cont G3 (RF)	21 (Eye)	100.00	100.00	100.00	100.00	100.00

Table 4-2 Performance evaluation for bands-based early and intermediate AMD classification. DF three-fold cross-validation and RF ten-fold cross-validation average performance metrics and leave-one-subject-out per eye performance.

Subject groups (Model)	Number of observations (Type)	Frequency bands-based results (%)				
		Sensitivity	Specificity	Precision	Accuracy	F1-score
AMD-cont G2 (DF)	13200 (B-scan)	89.94	95.97	94.91	93.23	92.35
AMD-cont G2 (DF)	22 (Eye)	70.00	83.33	77.78	77.27	73.68
AMD-cont G2 (RF)	13200 (B-scan)	87.68	93.18	91.46	90.68	89.53
AMD-cont G2 (RF)	22 (Eye)	70.00	83.33	77.78	77.27	73.68
AMD-cont G3 (RF)	12600 (B-scan)	97.33	98.35	98.17	97.87	97.75
AMD-cont G3 (RF)	21 (Eye)	100.00	100.00	100.00	100.00	100.00
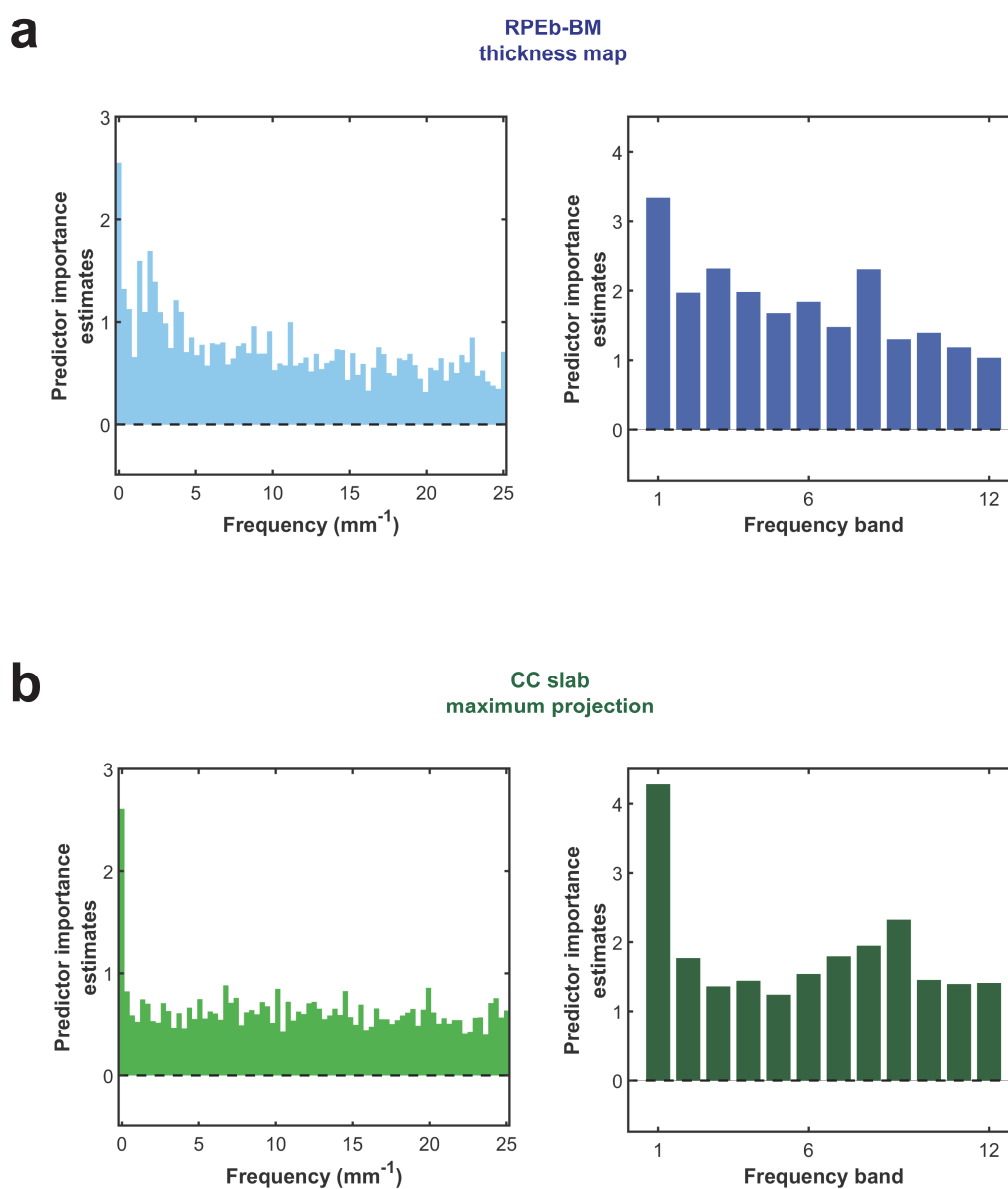
Figure 4-15 Predictor importance for one-fold of the ten-fold cross-validation for both spectrum-based and bands-based classifications using RF. (a, left) RPEb-BM thickness map frequency spectrum predictor importance. (a, right) RPEb-BM thickness map PCA-optimized bands predictor importance. (b, left) CC flow voids projection image frequency spectrum predictor importance. (b, right) CC flow voids projection image PCA-optimized bands predictor importance.

$\bar{\bar{s}}_L = 0.0029$
$\bar{d} = 32.9$ levels
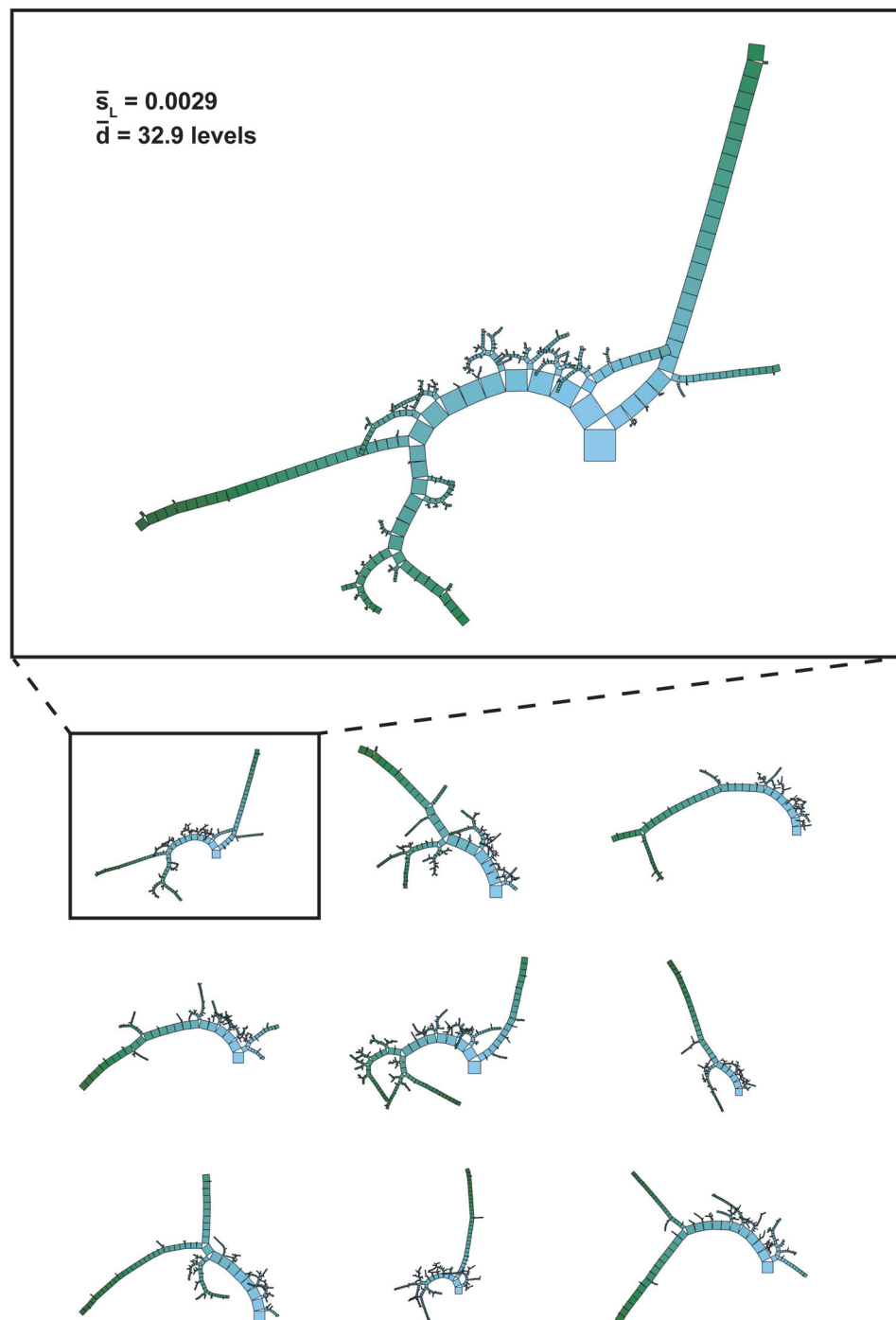
Figure 4-16 RF hierarchical representations (Pythagorean forest) generated from spectrum-based classification.

$$\bar{s}_L = 0.0038$$
$$\bar{d} = 25.3 \text{ levels}$$
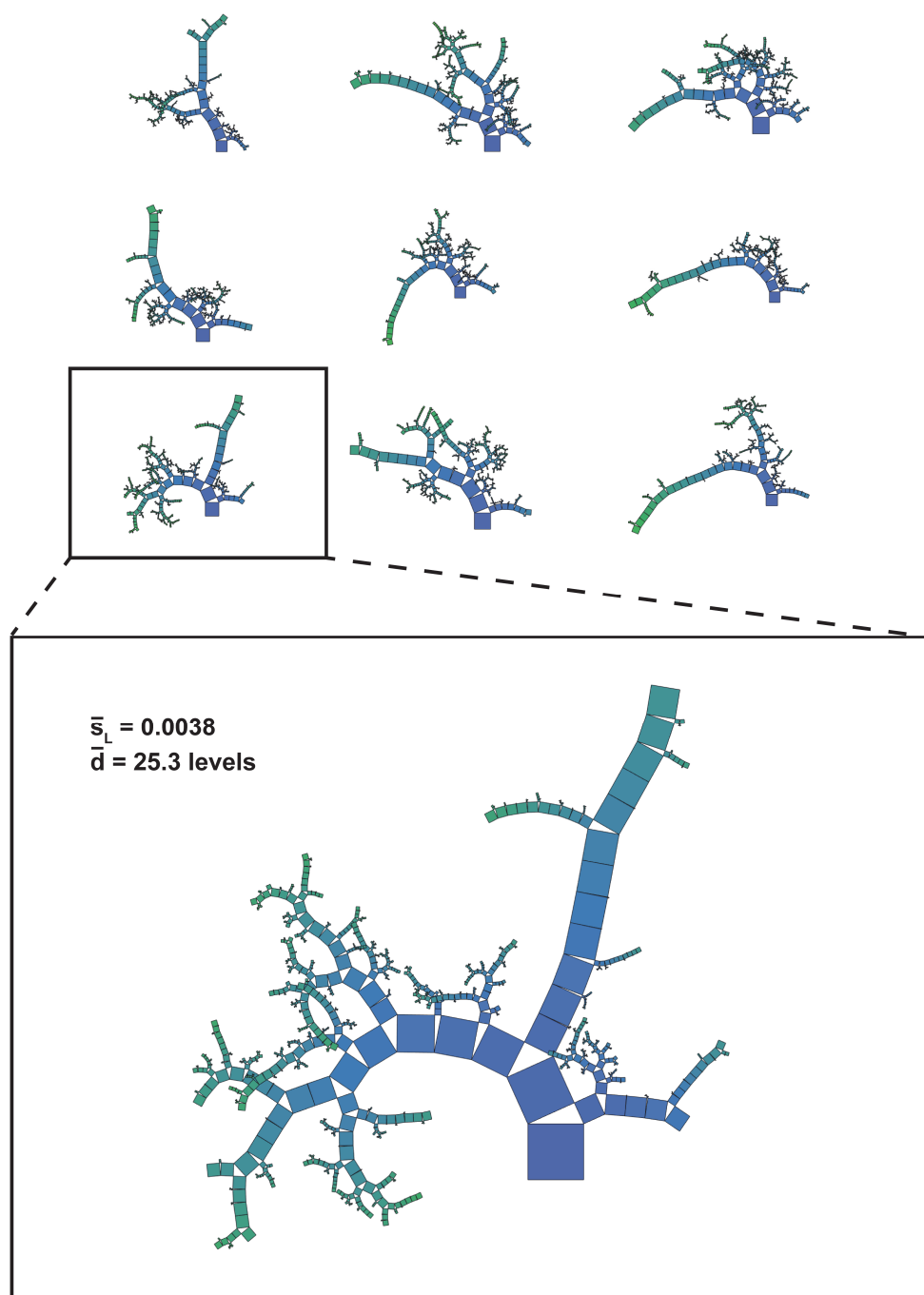
Figure 4-17 RF hierarchical representations (Pythagorean forest) generated from bands-based classification.

CHAPTER 5   DISCUSSION

The generated retinal thickness maps were useful as a means of ensuring the quality of the segmentation of each eye in the dataset. Differences between groups were not as significant as with RPEb-BM drusen segmentation quantifications and centering could have had an impact on measurements. When comparing measurements between AMD and similar age control subjects, the thickness Mann-Whitney U test significance was highest in the superior subfield, with a mean thickness of 332.9 μm for AMD subjects versus 354.8 μm for control subjects ($p \leq 0.01$). The test significance for volume was highest in the temporal subfield, with a mean volume of 0.465 mm^3 for AMD subjects versus 0.523 mm^3 for control subjects ($p \leq 0.01$). Data seem to indicate that AMD eyes are flatter, as evidenced by more similarly distributed central thickness measures, with means of 270 μm and 245.4 μm for AMD and controls respectively, and thinner AMD pericentral annulus thickness measures.

In the case of RCP network graph measurements, Mann-Whitney U tests revealed highest significance between AMD and controls links at the temporal subfield with a mean of 109.5 links for AMD subjects and 169.8 links for control subjects ($p \leq 0.001$). Highest significance was also found in the temporal subfield when comparing AMD and controls nodes with a mean of 119.1 nodes for AMD subjects and 185.6 nodes for control subjects ($p \leq 0.01$). While significant differences between groups were observed, challenges remain with regard to the method's validity. For example, it is possible that remaining sparsity artefacts contributed to a large fraction of the number of links and nodes observed in both groups. Despite the fact that morphological operations showed some success in reducing the effect of sparsity, they also result in segmentation errors. Even if there remain shortcomings, the comparison of repeatability measurements of controls with neovascular AMD measurements suggest that the method can be used for CNV or retinal angiomatous proliferation quantification. Seeing as CNVs originate from the choroid, elevating the BM to crop remaining PR algorithm artefacts is likely to represent an obstacle to reliable CNV detection.

Results suggest that the RPEb-BM space drusen quantification method is useful for discriminating between healthy and non-exudative AMD eyes. The distributions of the RPEb-BM space total area values for AMD and control subjects were found to be significantly different, with a mean value of 1.330 mm^2 for AMD subjects and 0.305 mm^2 for control subjects ($p \leq 0.001$). The distributions

of the RPEb-BM space total volume values for AMD and control subjects were also significantly different, with a mean value of $4.197 \cdot 10^{-2}$ mm^3 for AMD subjects and $6.461 \cdot 10^{-3}$ mm^3 for control subjects ($p \leq 0.001$). While not as significant, CC flow voids quantification still proved useful as the differences observed were also spread more evenly across the frontal plane of the eye. This is reflected in the FV10000 measurements. The distributions of the total FV10000 values for AMD and control subjects were significantly different, with a mean value of 0.195 for AMD subjects and 0.074 for control subjects ($p \leq 0.05$).

Using spectral counterparts to the spatial RPEb-BM space and CC flow voids measurements, the B-scan based classification models offer an approach to eye condition assessment. The model building approach assumes that B-scans from eyes with exudative AMD in the contralateral eyes can be discriminated from B-scans from undiagnosed eyes on the basis of measures that are believed to be representative of disease biomarkers. The RF and DF models k-fold cross validation results are promising although they are likely partially driven by characteristics present only in individual eyes. In particular, when classifying between AMD and similar age controls, highest accuracies were obtained for both RF and DF models using the full spectrums. The DF models demonstrated the best classification performance with ten-fold cross-validation accuracy of 95.51 %. At the current representation of eyes and B-scans with features that reflect the presence or absence of drusen or CC flow voids, results suggest that the models succeed in separating the two labelled classes.

Results also suggest that leaving one subject's eyes out of the training set had a significant impact on the model's ability to predict that certain eyes belong to individuals with non-exudative or neovascular AMD in the contralateral eye and should also be considered eyes with non-exudative AMD. Leaving one subject's eyes out of the training set also had a significant impact on the model's ability to predict that certain eyes are undiagnosed with non-exudative AMD. Indeed, accuracy was lower for leave-one-out validation with a maximum accuracy of 77.27 %. In both instances, looking at results more closely revealed that eyes in the AMD group which were misclassified had low drusen area compared to other AMD eyes, and eyes in the control group which were misclassified had a high fraction of flow voids exceeding 10,000 μm^2 compared to other control eyes (see results section 4.7 and Appendix F). The leave-one-subject-out validation therefore suggests that not all eyes which coexist with non-exudative or neovascular AMD in the contralateral eye show RPEb-BM space or CC level abnormalities. A different approach would

have been to label B-scans based on whole individual scans RPEb-BM drusen segmentation and CC flow voids quantifications. In that case, performance may have been more consistent with the presence of RPEb-BM space or CC level abnormalities rather than the more arbitrary scheme expecting abnormalities in eyes which coexist with non-exudative or neovascular AMD in the contralateral eye. The resulting models would have been directly designed as RPEb-BM space and CC abnormalities detectors rather than intended as non-exudative AMD detectors.

Keeping exactly the same approach, it is anticipated that as a greater number of eyes would be added to the training dataset, classification would be increasingly driven by feature profiles reflected in whole classes (AMD or control) rather than those present at individual eye level [119]. As such and in a similar way as it was observed in the case of the present models, it is anticipated that a model trained on a larger dataset would classify AMD B-scans increasingly on the basis of abnormal RPEb-BM space and CC level features which are shared by all or most AMD B-scans (belonging to an eye diagnosed with non-exudative AMD or with neovascular AMD in the contralateral eye).

In summary, B-scan and individual eye classification behaviour is expected to become progressively less dependent on individual eye training data as the size of the dataset increases. As the results support and as may have been achieved more conclusively using a slightly different approach, the models still behaves as B-scan level RPEb-BM space and CC level abnormalities detectors. Individual eyes can be classified, and whole eye scan level performance can be measured and interpreted using the method. Perhaps more importantly, the approach to B-scan classification allows grading eyes for abnormality severity not only on the basis of measures believed to be representative of drusen but also CC flow voids. While methods for the quantification of CC flow voids have been proposed [37], unlike the present approach they are not designed to provide B-scan level quantification or classification.

CHAPTER 6   CONCLUSION AND RECOMMENDATIONS

Several feature extraction methods were pursued. At whole eye volume level, a pipeline was constructed which allows the ETDRS grid-based joint assessment of retinal and choroidal features in health and disease. Results show that a novel method was developed which allows automated 3D reconstruction of retinal flow signal patterns (and indirectly, of retinal microvasculature) from OCTA images, followed by their quantitative evaluation. The method demonstrates the viable application of a network graph algorithm to projection resolved OCTA images of human retinas. Additionally, the automated analysis of RPEb-BM space and signal void sizes quantified from OCT and OCTA scans were implemented in the MATLAB environment and there is basic agreement of measurements with observations obtained using different OCT devices. Spectral features derived from measures representative of the RPEb-BM thickness map and CC were used to achieve automated spectral analysis and classification of early and intermediate AMD. The resulting classification models are interpretable and provides relatively promising non-exudative AMD B-scan level classification performance.

A limitation of the research project is that only the 3×3 mm field of view of the imaging device was exploited. The device itself allows up to a 9×15 mm field of view. The layers segmentation algorithms described in section 3.3 which served as a foundation for the other feature extraction methods were optimised for the 3×3 mm field of view. Modifications to the design of the layers segmentation algorithms would be necessary for implementation of the spatial and spectral features extraction methods to greater fields of view. The pipeline would benefit from implementation on a greater number of subjects. It was intended to recruit the greatest possible number of participants within the timeframe and the available resources to conduct the project. With more time and resources available, the sample sizes required to achieve ideal statistical power for the tests performed should be determined. Greater sample sizes would increase statistical power, reducing the risk of committing Type II errors towards the identification of novel biomarkers of disease and disease progression. A greater number of participants would also help ensure repeatability of the explored methods. The sample size limitation could be resolved by recruiting more subjects into the study.

Concerning the RCP network graph, methods have been described which could have improved the correction of flow projections [120]. Using the reflectance-based projection-resolved (rbPR)

OCTA algorithm, the in situ flow signal at deeper layers is better maintained and more of the projection artifacts are removed [120]. It would be beneficial to perform intensity-based 3D registration of the flow volumes towards assessing the pixel-level repeatability of segmented vessels and their skeletonizations, and to better quantify the progression of vascular anomalies in the retinal space. While the RPEb-BM drusen segmentation method proved useful in highlighting significant differences between groups, a layers-based approach is susceptible to segmentation error. The approach may also overlook small drusen and drusen that grow beyond the inner limits of the RPE. The limitations of layers-based drusen segmentation could be solved using state-of-the-art OCT drusen segmentation based on DL. Downsides of DL-based methods of drusen segmentation include the need for labelled data towards successful model training. However, the classification of targeted image areas makes DL less amenable to wrongly identifying abnormal elevation of the RPEb due to other causes (such as the accumulation of fluid) as drusen. Layers segmentation was completed in batches of B-scans in order to preserve depth resolution and minimize segmentation errors. As such, the first drusen segmentation method produces maps with visible transitions between batches. Results could be improved by reducing the size of the segmentation input scans thereby minimizing the required computational resources. B-scan level features extraction and classification could be improved using spectrogram images, wavelet transform, and other deep learning methods involving neural networks.

The research project required a basic understanding of several areas of scientific study and the application of a number of data processing and analysis techniques. With sustained development, OCT technologies are likely to become increasingly portable and affordable [121, 122], feature improved resolution [123] and offer live acquisition capabilities [124]. In addition to the potential for assisting clinicians as part of the AMD diagnostic process, the methods proposed could automate and provide remote access to interpretable eye health assessment and monitoring.

BIBLIOGRAPHY

[1]   C. J. Flaxel *et al.*, "Age-Related Macular Degeneration Preferred Practice Pattern®," *Ophthalmology,* vol. 127, no. 1, pp. P1-P65, 2020.

[2]   R. R. Bourne *et al.*, "Causes of vision loss worldwide, 1990–2010: a systematic analysis," *The lancet global health,* vol. 1, no. 6, pp. e339-e349, 2013.

[3]   K. L. Pennington and M. M. DeAngelis, "Epidemiology of age-related macular degeneration (AMD): associations with cardiovascular disease phenotypes and lipid factors," *Eye and vision,* vol. 3, no. 1, p. 34, 2016.

[4]   M. M. Brown, G. C. Brown, J. D. Stein, Z. Roth, J. Campanella, and G. R. Beauchamp, "Age-related macular degeneration: economic burden and value-based medicine analysis," *Canadian journal of ophthalmology,* vol. 40, no. 3, pp. 277-287, 2005.

[5]   A. R. Rudnicka *et al.*, "Incidence of late-stage age-related macular degeneration in American whites: systematic review and meta-analysis," *American journal of ophthalmology,* vol. 160, no. 1, pp. 85-93. e3, 2015.

[6]   H. C. Howland and M. Howland, "A standard nomenclature for the axes and planes of vertebrate eyes," *Vision research,* vol. 48, no. 18, pp. 1926-1927, 2008.

[7]   D. Ferrara, N. K. Waheed, and J. S. Duker, "Investigating the choriocapillaris and choroidal vasculature with new optical coherence tomography technologies," *Progress in retinal and eye research,* vol. 52, pp. 130-155, 2016.

[8]   A. P. Schachat, C. P. Wilkinson, D. R. Hinton, S. R. Sadda, and P. Wiedemann, *Ryan's Retina E-Book.* Elsevier Health Sciences, 2017.

[9]   R. F. Spaide, "Choriocapillaris signal voids in maternally inherited diabetes and deafness and in pseudoxanthoma elasticum," *Retina,* vol. 37, no. 11, pp. 2008-2014, 2017.

[10]   A. H. Kashani *et al.*, "Optical coherence tomography angiography: a comprehensive review of current methods and clinical applications," *Progress in retinal and eye research,* vol. 60, pp. 66-100, 2017.

[11]   J. Kur, E. A. Newman, and T. Chan-Ling, "Cellular and physiological mechanisms underlying blood flow regulation in the retina and choroid in health and disease," *Progress in retinal and eye research,* vol. 31, no. 5, pp. 377-406, 2012.

[12]   A. Reiner, M. E. Fitzgerald, N. Del Mar, and C. Li, "Neural control of choroidal blood flow," *Progress in retinal and eye research,* vol. 64, pp. 96-130, 2018.

[13]   J. L. Lauermann, N. Eter, and F. Alten, "Optical coherence tomography angiography offers new insights into choriocapillaris perfusion," *Ophthalmologica,* vol. 239, no. 2-3, pp. 74-84, 2018.

[14]   J. R. de Oliveira Dias *et al.*, "Natural history of subclinical neovascularization in nonexudative age-related macular degeneration using swept-source OCT angiography," *Ophthalmology,* vol. 125, no. 2, pp. 255-266, 2018.

[15]   F. L. Ferris III *et al.*, "Clinical classification of age-related macular degeneration," *Ophthalmology,* vol. 120, no. 4, pp. 844-851, 2013.

[16]   L. A. Yannuzzi *et al.*, "Retinal angiomatous proliferation in age–related macular degeneration," *Retina,* vol. 32, pp. 416-434, 2012.

[17]   J. Ambati, B. K. Ambati, S. H. Yoo, S. Ianchulev, and A. P. Adamis, "Age-related macular degeneration: etiology, pathogenesis, and therapeutic strategies," *Survey of ophthalmology,* vol. 48, no. 3, pp. 257-293, 2003.

[18]   P. J. Rosenfeld, "Optical coherence tomography and the development of antiangiogenic therapies in neovascular age-related macular degeneration," *Investigative ophthalmology & visual science,* vol. 57, no. 9, pp. OCT14-OCT26, 2016.

[19]   N. M. Bressler *et al.*, "Estimated cases of legal blindness and visual impairment avoided using ranibizumab for choroidal neovascularization: non-Hispanic white population in the United States with age-related macular degeneration," *Archives of ophthalmology,* vol. 129, no. 6, pp. 709-717, 2011.

[20]   S. Rofagha, R. B. Bhisitkul, D. S. Boyer, S. R. Sadda, K. Zhang, and S.-U. S. Group, "Seven-year outcomes in ranibizumab-treated patients in ANCHOR, MARINA, and HORIZON: a multicenter cohort study (SEVEN-UP)," *Ophthalmology,* vol. 120, no. 11, pp. 2292-2299, 2013.

[21]   M. G. Nittala, H. Ruiz-Garcia, and S. R. Sadda, "Accuracy and reproducibility of automated drusen segmentation in eyes with non-neovascular age-related macular degeneration," *Investigative ophthalmology & visual science,* vol. 53, no. 13, pp. 8319-8324, 2012.

[22]   A. C. Tan *et al.*, "Calcified nodules in retinal drusen are associated with disease progression in age-related macular degeneration," *Science translational medicine,* vol. 10, no. 466, p. eaat4544, 2018.

[23]   R. Zhao *et al.*, "Automated drusen detection in dry age-related macular degeneration by multiple-depth, en face optical coherence tomography," *Biomedical optics express,* vol. 8, no. 11, pp. 5049-5064, 2017.

[24]   C. Balaratnasingam *et al.*, "Cuticular drusen: clinical phenotypes and natural history defined using multimodal imaging," *Ophthalmology,* vol. 125, no. 1, pp. 100-118, 2018.

[25]   P. H. Tomlins and R. K. Wang, "Theory, developments and applications of optical coherence tomography," *Journal of Physics D: Applied Physics,* vol. 38, no. 15, p. 2519, 2005.

[26]   D. Huang *et al.*, "Optical coherence tomography," *science,* vol. 254, no. 5035, pp. 1178-1181, 1991.

[27]   M. F. Kraus *et al.*, "Motion correction in optical coherence tomography volumes on a per A-scan basis using orthogonal scan patterns," *Biomedical optics express,* vol. 3, no. 6, pp. 1182-1199, 2012.

[28]   C.-L. Chen and R. K. Wang, "Optical coherence tomography based angiography," *Biomedical optics express,* vol. 8, no. 2, pp. 1056-1082, 2017.

[29]   T. E. De Carlo, A. Romano, N. K. Waheed, and J. S. Duker, "A review of optical coherence tomography angiography (OCTA)," *International journal of retina and vitreous,* vol. 1, no. 1, p. 5, 2015.

[30]   K. Chalam and K. Sambhav, "Optical coherence tomography angiography in retinal diseases," *Journal of ophthalmic & vision research,* vol. 11, no. 1, p. 84, 2016.

[31]   Z. Chu *et al.*, "Quantitative assessment of the retinal microvasculature using optical coherence tomography angiography," *Journal of biomedical optics,* vol. 21, no. 6, p. 066008, 2016.

[32]   S. G. Gadde *et al.*, "Quantification of vessel density in retinal optical coherence tomography angiography images using local fractal dimension," *Investigative ophthalmology & visual science,* vol. 57, no. 1, pp. 246-252, 2016.

[33]   S. S. Gao *et al.*, "Quantification of choroidal neovascularization vessel length using optical coherence tomography angiography," *Journal of biomedical optics,* vol. 21, no. 7, p. 076010, 2016.

[34]   M. Alam, D. Thapa, J. I. Lim, D. Cao, and X. Yao, "Quantitative characteristics of sickle cell retinopathy in optical coherence tomography angiography," *Biomedical optics express,* vol. 8, no. 3, pp. 1741-1753, 2017.

[35]   C. Leahy, H. Radhakrishnan, G. Weiner, J. L. Goldberg, and V. J. Srinivasan, "Mapping the 3D connectivity of the rat inner retinal vascular network using OCT angiography," *Investigative ophthalmology & visual science,* vol. 56, no. 10, pp. 5785-5793, 2015.

[36]   F. Coscas *et al.*, "Quantitative optical coherence tomography angiography biomarkers for neovascular age-related macular degeneration in remission," *PloS one,* vol. 13, no. 10, 2018.

[37]   R. F. Spaide, "Choriocapillaris flow features follow a power law distribution: implications for characterization and mechanisms of disease progression," *American journal of ophthalmology,* vol. 170, pp. 58-67, 2016.

[38]   A. Uji, S. Balasubramanian, J. Lei, E. Baghdasaryan, M. Al-Sheikh, and S. R. Sadda, "Choriocapillaris imaging using multiple en face optical coherence tomography angiography image averaging," *JAMA ophthalmology,* vol. 135, no. 11, pp. 1197-1204, 2017.

[39]   R. F. Spaide, "Ising model of choriocapillaris flow," *Retina,* vol. 38, no. 1, pp. 79-83, 2018.

[40]   Q. Chen *et al.*, "Automated drusen segmentation and quantification in SD-OCT images," *Medical image analysis,* vol. 17, no. 8, pp. 1058-1072, 2013.

[41]   H. Bogunović *et al.*, "Machine learning of the progression of intermediate age-related macular degeneration based on OCT imaging," *Investigative ophthalmology & visual science,* vol. 58, no. 6, pp. BIO141-BIO150, 2017.

[42]   Z. Yehoshua *et al.*, "Comparison of drusen area detected by spectral domain optical coherence tomography and color fundus imaging," *Investigative ophthalmology & visual science,* vol. 54, no. 4, pp. 2429-2434, 2013.

[43]   N. Jain *et al.*, "Quantitative comparison of drusen segmented on SD-OCT versus drusen delineated on color fundus photographs," *Investigative ophthalmology & visual science,* vol. 51, no. 10, pp. 4875-4883, 2010.

[44]   Y. LeCun, Y. Bengio, and G. Hinton, "Deep learning," *nature,* vol. 521, no. 7553, pp. 436-444, 2015.

[45]   I. Goodfellow, Y. Bengio, and A. Courville, *Deep learning*. MIT press, 2016.

[46]   L. V. Utkin, A. A. Meldo, and A. V. Konstantinov, "Deep Forest as a framework for a new class of machine-learning models," *National Science Review,* vol. 6, no. 2, pp. 186-187, 2019.

[47]   Y. Guo, Y. Liu, A. Oerlemans, S. Lao, S. Wu, and M. S. Lew, "Deep learning for visual understanding: A review," *Neurocomputing,* vol. 187, pp. 27-48, 2016.

[48]   S. Sengupta, A. Singh, H. A. Leopold, T. Gulati, and V. Lakshminarayanan, "Ophthalmic Diagnosis Using Deep Learning with Fundus Images-A Critical Review," *Artificial Intelligence in Medicine,* p. 101758, 2019.

[49]   N. Cristianini and J. Shawe-Taylor, *An introduction to support vector machines and other kernel-based learning methods*. Cambridge university press, 2000.

[50]   T. K. Ho, "Random decision forests," in *Proceedings of 3rd international conference on document analysis and recognition*, 1995, vol. 1, pp. 278-282: IEEE.

[51]   T. K. Ho, "The random subspace method for constructing decision forests," *IEEE transactions on pattern analysis and machine intelligence,* vol. 20, no. 8, pp. 832-844, 1998.

[52]   L. Breiman, "Random forests," *Machine learning,* vol. 45, no. 1, pp. 5-32, 2001.

[53]   R. O. Duda, P. E. Hart, and D. G. Stork, *Pattern classification*. John Wiley & Sons, 2012.

[54]   R. Besenczi, J. Tóth, and A. Hajdu, "A review on automatic analysis techniques for color fundus photographs," *Computational and structural biotechnology journal,* vol. 14, pp. 371-384, 2016.

[55]   G. Gregori *et al.*, "Change in drusen area over time compared using spectral-domain optical coherence tomography and color fundus imaging," *Investigative ophthalmology & visual science,* vol. 55, no. 11, pp. 7662-7668, 2014.

[56]   C. Playout, R. Duval, and F. Cheriet, "A novel weakly supervised multitask architecture for retinal lesions segmentation on fundus images," *IEEE transactions on medical imaging,* vol. 38, no. 10, pp. 2434-2444, 2019.

[57]   M. Braović, D. Božić-Štulić, and D. Stipaničev, "A review of image processing and deep learning based methods for automated analysis of digital retinal fundus images," in *2018 3rd International Conference on Smart and Sustainable Technologies (SpliTech)*, 2018, pp. 1-6: IEEE.

[58]   M. Niemeijer, B. van Ginneken, S. R. Russell, M. S. Suttorp-Schulten, and M. D. Abramoff, "Automated detection and differentiation of drusen, exudates, and cotton-wool spots in digital color fundus photographs for diabetic retinopathy diagnosis," *Investigative ophthalmology & visual science,* vol. 48, no. 5, pp. 2260-2267, 2007.

[59]   C. Playout, R. Duval, and F. Cheriet, "A multitask learning architecture for simultaneous segmentation of bright and red lesions in fundus images," in *International Conference on Medical Image Computing and Computer-Assisted Intervention*, 2018, pp. 101-108: Springer.

[60] P. M. Burlina, N. Joshi, M. Pekala, K. D. Pacheco, D. E. Freund, and N. M. Bressler, "Automated grading of age-related macular degeneration from color fundus images using deep convolutional neural networks," *JAMA ophthalmology,* vol. 135, no. 11, pp. 1170-1176, 2017.

[61] P. Burlina, K. D. Pacheco, N. Joshi, D. E. Freund, and N. M. Bressler, "Comparing humans and deep learning performance for grading AMD: a study in using universal deep features and transfer learning for automated AMD analysis," *Computers in biology and medicine,* vol. 82, pp. 80-86, 2017.

[62] A. Govindaiah, M. A. Hussain, R. T. Smith, and A. Bhuiyan, "Deep convolutional neural network based screening and assessment of age-related macular degeneration from fundus images," in *2018 IEEE 15th International Symposium on Biomedical Imaging (ISBI 2018)*, 2018, pp. 1525-1528: IEEE.

[63] J. H. Tan *et al.*, "Age-related macular degeneration detection using deep convolutional neural network," *Future Generation Computer Systems,* vol. 87, pp. 127-135, 2018.

[64] A. Govindaiah, R. T. Smith, and A. Bhuiyan, "A new and improved method for automated screening of age-related macular degeneration using ensemble deep neural networks," in *2018 40th Annual International Conference of the IEEE Engineering in Medicine and Biology Society (EMBC)*, 2018, pp. 702-705: IEEE.

[65] P. Burlina, D. E. Freund, N. Joshi, Y. Wolfson, and N. M. Bressler, "Detection of age-related macular degeneration via deep learning," in *2016 IEEE 13th International Symposium on Biomedical Imaging (ISBI)*, 2016, pp. 184-188: IEEE.

[66] F. Grassmann *et al.*, "A deep learning algorithm for prediction of age-related eye disease study severity scale for age-related macular degeneration from color fundus photography," *Ophthalmology,* vol. 125, no. 9, pp. 1410-1420, 2018.

[67] A. Horta *et al.*, "A hybrid approach for incorporating deep visual features and side channel information with applications to amd detection," in *2017 16th IEEE International Conference on Machine Learning and Applications (ICMLA)*, 2017, pp. 716-720: IEEE.

[68] S. G. Zadeh *et al.*, "CNNs enable accurate and fast segmentation of drusen in optical coherence tomography," in *Deep Learning in Medical Image Analysis and Multimodal Learning for Clinical Decision Support*: Springer, 2017, pp. 65-73.

[69] L. Fang, C. Wang, S. Li, H. Rabbani, X. Chen, and Z. Liu, "Attention to lesion: Lesion-aware convolutional neural network for retinal optical coherence tomography image classification," *IEEE transactions on medical imaging,* vol. 38, no. 8, pp. 1959-1970, 2019.

[70] J. Deng *et al.*, "Age-related macular degeneration detection and stage classification using choroidal oct images," in *International Conference on Image Analysis and Recognition*, 2016, pp. 707-715: Springer.

[71] J. De Fauw *et al.*, "Clinically applicable deep learning for diagnosis and referral in retinal disease," *Nature medicine,* vol. 24, no. 9, pp. 1342-1350, 2018.

[72] S. Saha, M. Nassisi, M. Wang, S. Lindenberg, S. Sadda, and Z. J. Hu, "Automated detection and classification of early AMD biomarkers using deep learning," *Scientific reports,* vol. 9, no. 1, pp. 1-9, 2019.

[73] C. S. Lee, D. M. Baughman, and A. Y. Lee, "Deep learning is effective for classifying normal versus age-related macular degeneration OCT images," *Ophthalmology Retina,* vol. 1, no. 4, pp. 322-327, 2017.

[74] M. Treder, J. L. Lauermann, and N. Eter, "Automated detection of exudative age-related macular degeneration in spectral domain optical coherence tomography using deep learning," *Graefe's Archive for Clinical and Experimental Ophthalmology,* vol. 256, no. 2, pp. 259-265, 2018.

[75] F. Doshi-Velez and B. Kim, "Towards a rigorous science of interpretable machine learning," *arXiv preprint arXiv:1702.08608,* 2017.

[76] Z.-H. Zhou and J. Feng, "Deep forest," *arXiv preprint arXiv:1702.08835,* 2017.

[77] Y. Guo, S. Liu, Z. Li, and X. Shang, "BCDForest: a boosting cascade deep forest model towards the classification of cancer subtypes based on gene expression data," *BMC bioinformatics,* vol. 19, no. 5, p. 118, 2018.

[78] R. Su, X. Liu, L. Wei, and Q. Zou, "Deep-Resp-Forest: A deep forest model to predict anti-cancer drug response," *Methods,* vol. 166, pp. 91-102, 2019.

[79] Y. Boualleg, M. Farah, and I. R. Farah, "Remote sensing scene classification using convolutional features and deep forest classifier," *IEEE Geoscience and Remote Sensing Letters,* vol. 16, no. 12, pp. 1944-1948, 2019.

[80] E. R. Group, "Classification of diabetic retinopathy from fluorescein angiograms," ETDRS report1991.

[81] M. Röhlig, J. Stüwe, C. Schmidt, R. K. Prakasam, O. Stachs, and H. Schumann, "Grid-based exploration of OCT thickness data of intraretinal layers," in *Proceedings of the 14th International Joint Conference on Computer Vision, Imaging and Computer Graphics Theory and Applications*, 2019, vol. 3, pp. 129-140.

[82] M. M. Mauschitz *et al.*, "Topography of geographic atrophy in age-related macular degeneration," *Investigative ophthalmology & visual science,* vol. 53, no. 8, pp. 4932-4939, 2012.

[83] M. Beck, M. R. Munk, A. Ebneter, S. Wolf, and M. S. Zinkernagel, "Retinal Ganglion Cell Layer Change in Patients Treated With Anti–Vascular Endothelial Growth Factor for Neovascular Age-related Macular Degeneration," *American journal of ophthalmology,* vol. 167, pp. 10-17, 2016.

[84] J. Sarks, S. Sarks, and M. Killingsworth, "Evolution of soft drusen in age-related macular degeneration," *Eye,* vol. 8, no. 3, pp. 269-283, 1994.

[85] G. James, D. Witten, T. Hastie, and R. Tibshirani, *An introduction to statistical learning*. Springer, 2013.

[86] J. Chhablani, T. Krishnan, V. Sethi, and I. Kozak, "Artifacts in optical coherence tomography," *Saudi Journal of Ophthalmology,* vol. 28, no. 2, pp. 81-87, 2014.

[87] S. Ricco, M. Chen, H. Ishikawa, G. Wollstein, and J. Schuman, "Correcting motion artifacts in retinal spectral domain optical coherence tomography via image registration," in *International Conference on Medical Image Computing and Computer-Assisted Intervention*, 2009, pp. 100-107: Springer.

[88] D. Evin, A. Hadad, A. Solano, and B. Drozdowicz, "Segmentation Fusion Techniques with Application to Plenoptic Images: A Survey," in *Journal of Physics: Conference Series*, 2016, vol. 705, no. 1, p. 012026: IOP Publishing.

[89] J. Mazzaferri, L. Beaton, G. Hounye, D. N. Sayah, and S. Costantino, "Open-source algorithm for automatic choroid segmentation of OCT volume reconstructions," *Scientific reports,* vol. 7, p. 42112, 2017.

[90] G. Gallo and S. Pallottino, "Shortest path algorithms," *Annals of operations research,* vol. 13, no. 1, pp. 1-79, 1988.

[91] K. Li, X. Wu, D. Z. Chen, and M. Sonka, "Optimal surface segmentation in volumetric images-a graph-theoretic approach," *IEEE transactions on pattern analysis and machine intelligence,* vol. 28, no. 1, pp. 119-134, 2006.

[92] L. Zhang, K. Lee, M. Niemeijer, R. F. Mullins, M. Sonka, and M. D. Abramoff, "Automated segmentation of the choroid from clinical SD-OCT," *Investigative ophthalmology & visual science,* vol. 53, no. 12, pp. 7510-7519, 2012.

[93] M. Zhang *et al.*, "Projection-resolved optical coherence tomographic angiography," *Biomedical optics express,* vol. 7, no. 3, pp. 816-828, 2016.

[94] T. Rim *et al.*, "Retinal vessel structure measurement using spectral-domain optical coherence tomography," *Eye,* vol. 30, no. 1, p. 111, 2016.

[95] T. Coye, "A novel retinal blood vessel segmentation algorithm for fundus images. 2015," ed.

[96] T. Ridler and S. Calvard, "Picture thresholding using an iterative selection method," *IEEE trans syst Man Cybern,* vol. 8, no. 8, pp. 630-632, 1978.

[97] T. T. Hormel, J. Wang, S. T. Bailey, T. S. Hwang, D. Huang, and Y. Jia, "Maximum value projection produces better en face OCT angiograms than mean value projection," *Biomedical Optics Express,* vol. 9, no. 12, pp. 6412-6424, 2018.

[98] M. Kerschnitzki *et al.*, "Architecture of the osteocyte network correlates with bone material quality," *Journal of bone and mineral research,* vol. 28, no. 8, pp. 1837-1845, 2013.

[99] Y. Chen and B. Kateb, *Neurophotonics and Brain Mapping*. CRC Press, 2017.

[100] N. Phansalkar, S. More, A. Sabale, and M. Joshi, "Adaptive local thresholding for detection of nuclei in diversity stained cytology images," in *2011 International Conference on Communications and Signal Processing*, 2011, pp. 218-220: IEEE.

[101] J. Sauvola and M. Pietikäinen, "Adaptive document image binarization," *Pattern recognition,* vol. 33, no. 2, pp. 225-236, 2000.

[102] J. W. Cooley and J. W. Tukey, "An algorithm for the machine calculation of complex Fourier series," *Mathematics of computation,* vol. 19, no. 90, pp. 297-301, 1965.

[103] G. V. Trunk, "A problem of dimensionality: A simple example," *IEEE Transactions on pattern analysis and machine intelligence,* no. 3, pp. 306-307, 1979.

[104] S. Theodoridis and K. Koutroumbas, *Pattern recognition & Matlab intro*. Academic Press, Inc., 2010.

[105] J. F. Hair, W. C. Black, B. J. Babin, R. E. Anderson, and R. L. Tatham, *Multivariate data analysis* (no. 3). Prentice hall Upper Saddle River, NJ, 1998.

[106] A. Bosman, "Het wondere onderzoekingsveld der vlakke meetkunde.(Dutch)[The Wondrous Exploration Field of Plane Geometry][Электронный ресурс]/Albert E. Bosman," *Breda: NV Uitgeversmaatschappij Parcival,* pp. 84-86, 1957.

[107] F. Beck, M. Burch, T. Munz, L. Di Silvestro, and D. Weiskopf, "Generalized Pythagoras trees for visualizing hierarchies," in *2014 International Conference on Information Visualization Theory and Applications (IVAPP)*, 2014, pp. 17-28: IEEE.

[108] A. Chakure. (2019). *Random forest regression Along with its implementation in Python*. Available: https://towardsdatascience.com/random-forest-and-its-implementation-71824ced454f

[109] T. M. Oshiro, P. S. Perez, and J. A. Baranauskas, "How many trees in a random forest?," in *International workshop on machine learning and data mining in pattern recognition*, 2012, pp. 154-168: Springer.

[110] P. G. Poličar, "Pitagorejska drevesa za vizualizacijo klasifikacijskih in regresijskih dreves," Univerza v Ljubljani, 2016.

[111] S.-H. Lyu, L. Yang, and Z.-H. Zhou, "A Refined Margin Distribution Analysis for Forest Representation Learning," in *Advances in Neural Information Processing Systems*, 2019, pp. 5531-5541.

[112] P. Geurts, D. Ernst, and L. Wehenkel, "Extremely randomized trees," *Machine learning,* vol. 63, no. 1, pp. 3-42, 2006.

[113] F. T. Liu, K. M. Ting, Y. Yu, and Z.-H. Zhou, "Spectrum of variable-random trees," *Journal of Artificial Intelligence Research,* vol. 32, pp. 355-384, 2008.

[114] A. Hart, "Mann-Whitney test is not just a test of medians: differences in spread can be important," *Bmj,* vol. 323, no. 7309, pp. 391-393, 2001.

[115] J. M. Hoem, "The reporting of statistical significance in scientific journals," *Demographic Research,* vol. 18, pp. 437-442, 2008.

[116] M. Trinh, M. Kalloniatis, and L. Nivison-Smith, "Vascular Changes in Intermediate Age-Related Macular Degeneration Quantified Using Optical Coherence Tomography Angiography," *Translational vision science & technology,* vol. 8, no. 4, pp. 20-20, 2019.

[117] R. Bourne, *Fundamentals of digital imaging in medicine*. Springer Science & Business Media, 2010.

[118] J. L. Hintze and R. D. Nelson, "Violin plots: a box plot-density trace synergism," *The American Statistician,* vol. 52, no. 2, pp. 181-184, 1998.

[119] E. C. Neto *et al.*, "Detecting the impact of subject characteristics on machine learning-based diagnostic applications," *NPJ digital medicine,* vol. 2, no. 1, pp. 1-6, 2019.

[120] J. Wang *et al.*, "Reflectance-based projection-resolved optical coherence tomography angiography," *Biomedical optics express,* vol. 8, no. 3, pp. 1536-1548, 2017.

[121] G. Song *et al.*, "First clinical application of low-cost OCT," *Translational vision science & technology,* vol. 8, no. 3, pp. 61-61, 2019.

[122] C. Viehland *et al.*, "Ergonomic handheld OCT angiography probe optimized for pediatric and supine imaging," *Biomedical optics express,* vol. 10, no. 5, pp. 2623-2638, 2019.

[123] L. Ginner *et al.*, "Noniterative digital aberration correction for cellular resolution retinal optical coherence tomography in vivo," *Optica,* vol. 4, no. 8, pp. 924-931, 2017.

[124] J. P. Kolb *et al.*, "Live video rate volumetric OCT imaging of the retina with multi-MHz A-scan rates," *PloS one,* vol. 14, no. 3, 2019.

[125] M. Corinthios, *Signals, systems, transforms, and digital signal processing with MATLAB*. CRC Press, 2009.

[126] J. W. Cooley, P. A. Lewis, and P. D. Welch, "The fast Fourier transform and its applications," *IEEE Transactions on Education,* vol. 12, no. 1, pp. 27-34, 1969.

APPENDIX A – DETAILED PROJECT WORKFLOW
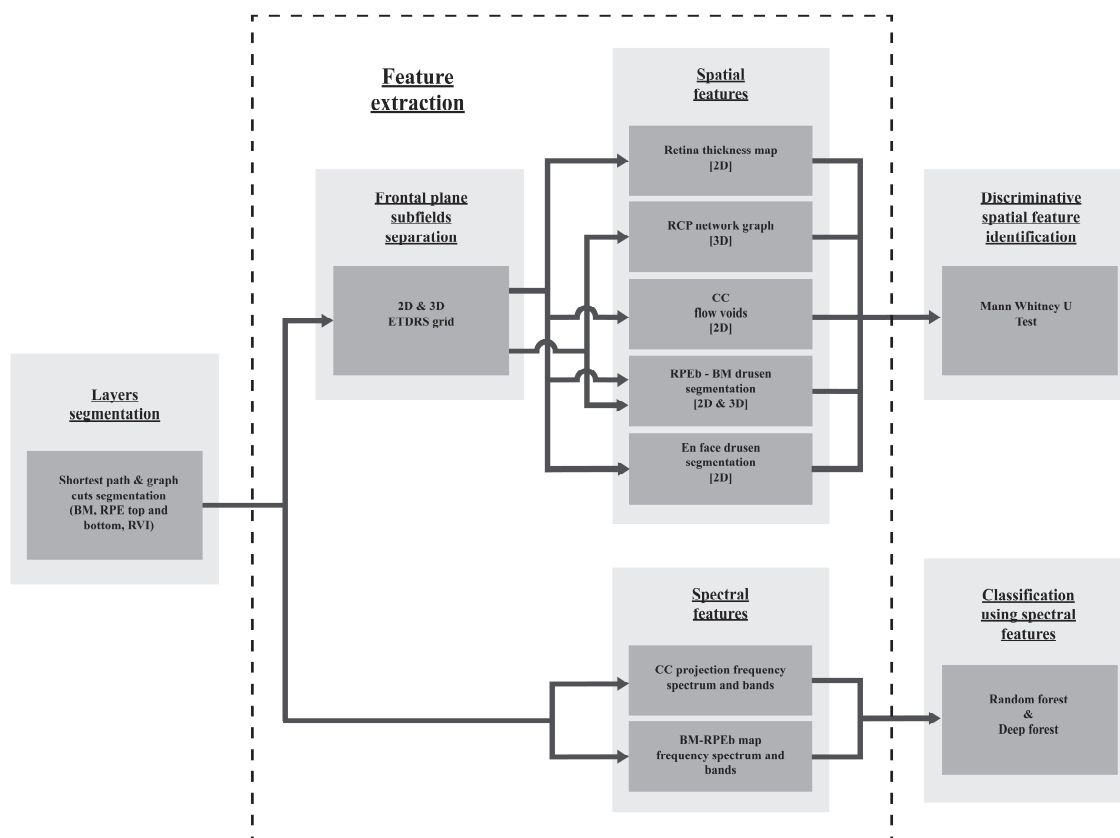
Figure A-1 Detailed schematic of the research project workflow.

APPENDIX B – FOURIER TRANSFORMATION

The Figure B-1 below shows the representation of a spatial series into its rhythmic components in the frequency domain.
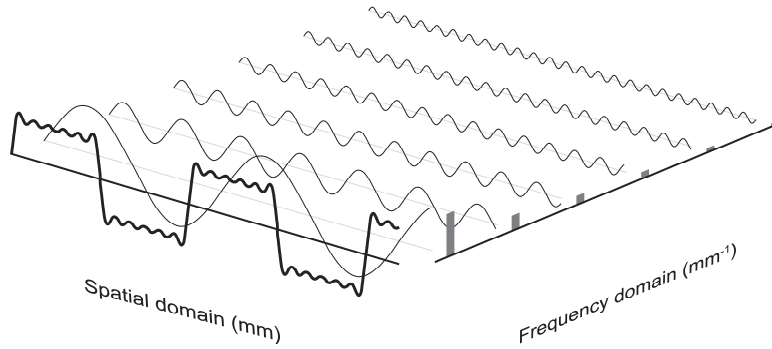
Figure B-1 Spatial domain series and the corresponding Fourier series in the frequency domain.

As illustrated above, finite duration or periodic waves can be expressed in the form of sums of trigonometric (cosines and sines waves) or complex exponential functions: Fourier series [125]. The spatial period X corresponding to a waveform's crest-to-crest repetition distance, can be inverted to find the x-domain spatial frequency, f as shown below.

$$f = \frac{1}{X} \tag{1}$$

A mathematical tool, the Fourier transformation makes it possible to move from the spatial domain to the frequency domain [126]. The equation of the continuous Fourier transform (FT) is provided below.

$$F(\omega) = \int_{-\infty}^{\infty} f(x)e^{-i\omega x}dx \tag{2}$$

In the equation above, ω is the angular frequency, $i = \sqrt{-1}$ and f(x) is the spatial series (a function of spatial location, x) to be deconstructed into the sum of cosines and sines. The function $F(\omega)$ is the Fourier transform of f(x). For discrete and periodic spatial series, the continuous FT is not needed, and the discrete Fourier transform is used [102, 126]. Equations of the discrete Fourier transform (DFT) for a given spatial series, a(n), are provided below. The spatial series, a(n) has values in the range $n = 0...N – 1$, and W is the principal Nth root of unity.

$$A(j) = \sum_{n=0}^{N-1} a(n) W^{jn}, \quad j = 0, 1, \dots, N - 1 \quad\quad (3)$$

$$W = e^{-i\frac{2\pi}{N}} \quad\quad (4)$$

The fast Fourier transform (FFT) is an algorithm which rapidly computes the DFT [126].

APPENDIX C – BANDS OPTIMISATION

The set of equations below were used as part of an algorithm which allocates the average of a progressively greater number of frequencies into each band as frequency increases along the spectrum. Figure C-1 provides a schematic description of the frequency bands optimisation process.

$$P_B = \begin{cases} P(v_0), & \text{if } v_n = v_0 \\ \langle P(v_{r_1,B} : v_{r_2,B}) \rangle, & \text{if } v_{r_1,1} \leq v_n < v_a \\ \langle P(v_a : v_b) \rangle, & \text{if } v_a \leq v_n \leq v_b \end{cases} \tag{1}$$

$$n \in 0 : v_b$$

Where,

$$v_0, \ \Delta v_0, v_{r_2,0} = 1 \tag{2}$$

$$v_b = \dim(v) \tag{3}$$

$$v_a = \text{nint}(0.893 \cdot v_b) \tag{4}$$

$$\Delta v_B = \Delta v_{B-1} + 1 \tag{5}$$

$$v_{r_1,B} = v_{r_2,B-1} + 1 \tag{6}$$

$$v_{r_2,B} = \begin{cases} v_{r_1,B} + \Delta v_B, & \text{if } v_{r_1,B} + \Delta v_B < v_a \\ v_a, & \text{if } v_{r_1,B} + \Delta v_B \geq v_a \end{cases} \tag{7}$$

$$B \in 1 : B_T$$

In the set of equations, the term P_B is the amplitude assigned to each band. The power corresponding to the first band is equivalent to the amplitude of the first element, v_0 of the spectrum array, v, of size v_b. Then, within the interval between $v_{r1,1}$ and v_a, band amplitudes correspond to the mean power, designated by chevrons $\langle \rangle$, of values between $v_{r1,B}$ and $v_{r2,B}$ within the spectrum array, v. The term v_a corresponds to the nearest integer rounded value of a specified fraction of the size v_b of the array, v. With each band iteration, B, to the total number of bands, B_T, the interval Δv_B is augmented by the nearest integer rounded value of a specified fraction of the size v_b of the spectrum array, v. The interval Δv_B is added to $v_{r1,B}$ to give $v_{r2,B}$. Once $v_{r2,B}$ exceeds v_a, the last band is assigned the mean power, designated by chevrons $\langle \rangle$, of values from v_a to v_b within the spectrum array, v.
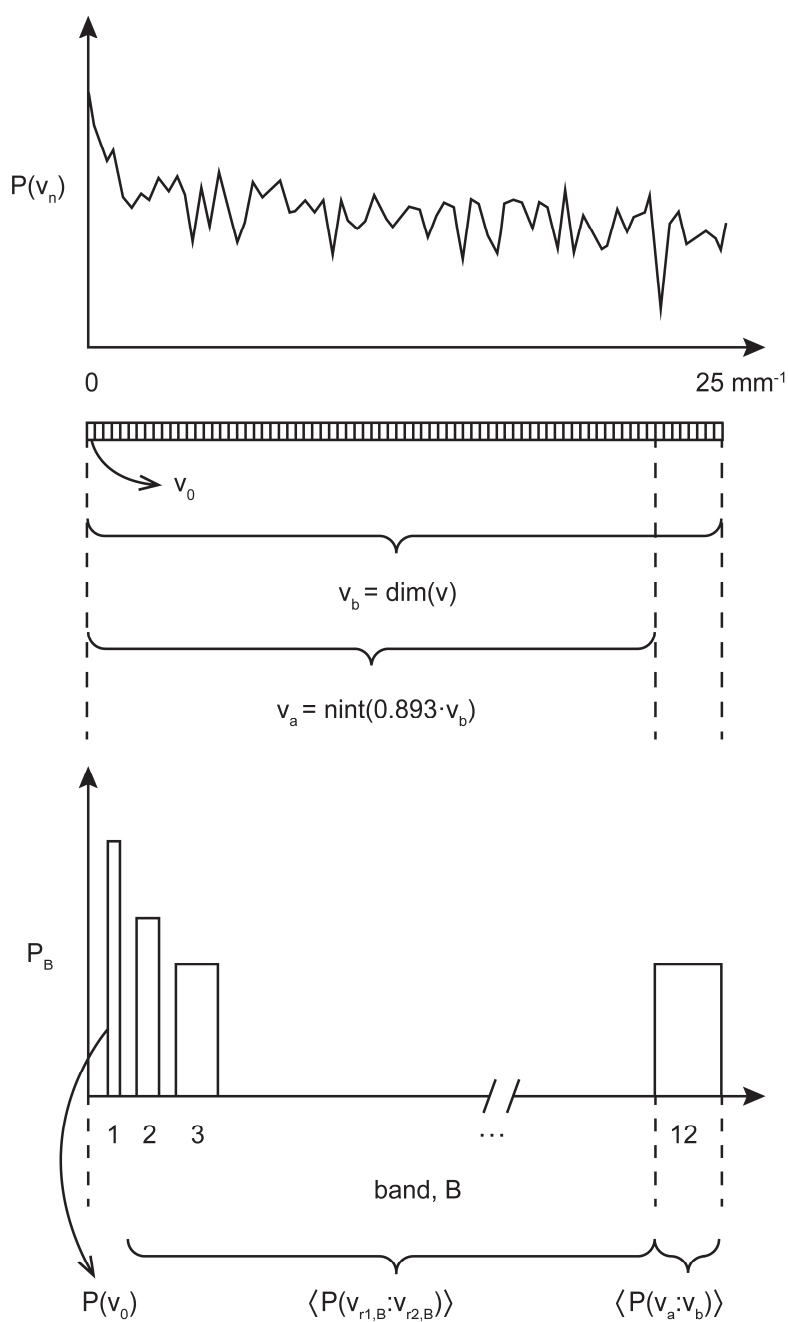
Figure C-1 Schematic description of the frequency bands optimisation process.

APPENDIX D – NETWORK GRAPH REPEATABILITY

a
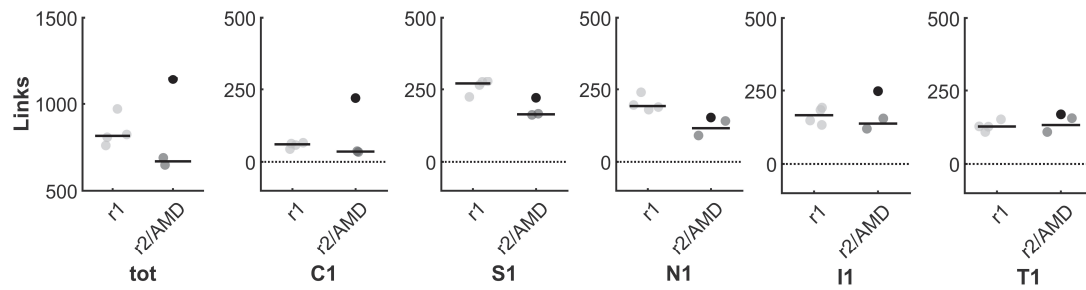
b
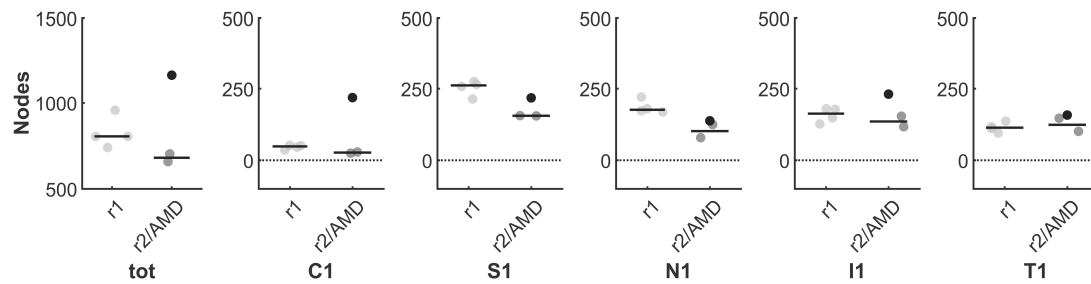
Figurer D-1 (a) Network graph links distributions versus ETDRS regions for repeated scans of both eyes from a normal subject (light and dark grey dots) and a neovascular AMD subject (black dots). (b) Network graph nodes distributions versus ETDRS regions for repeated scans of both eyes from a normal subject (light and dark grey dots) and a neovascular AMD subject (black dots).
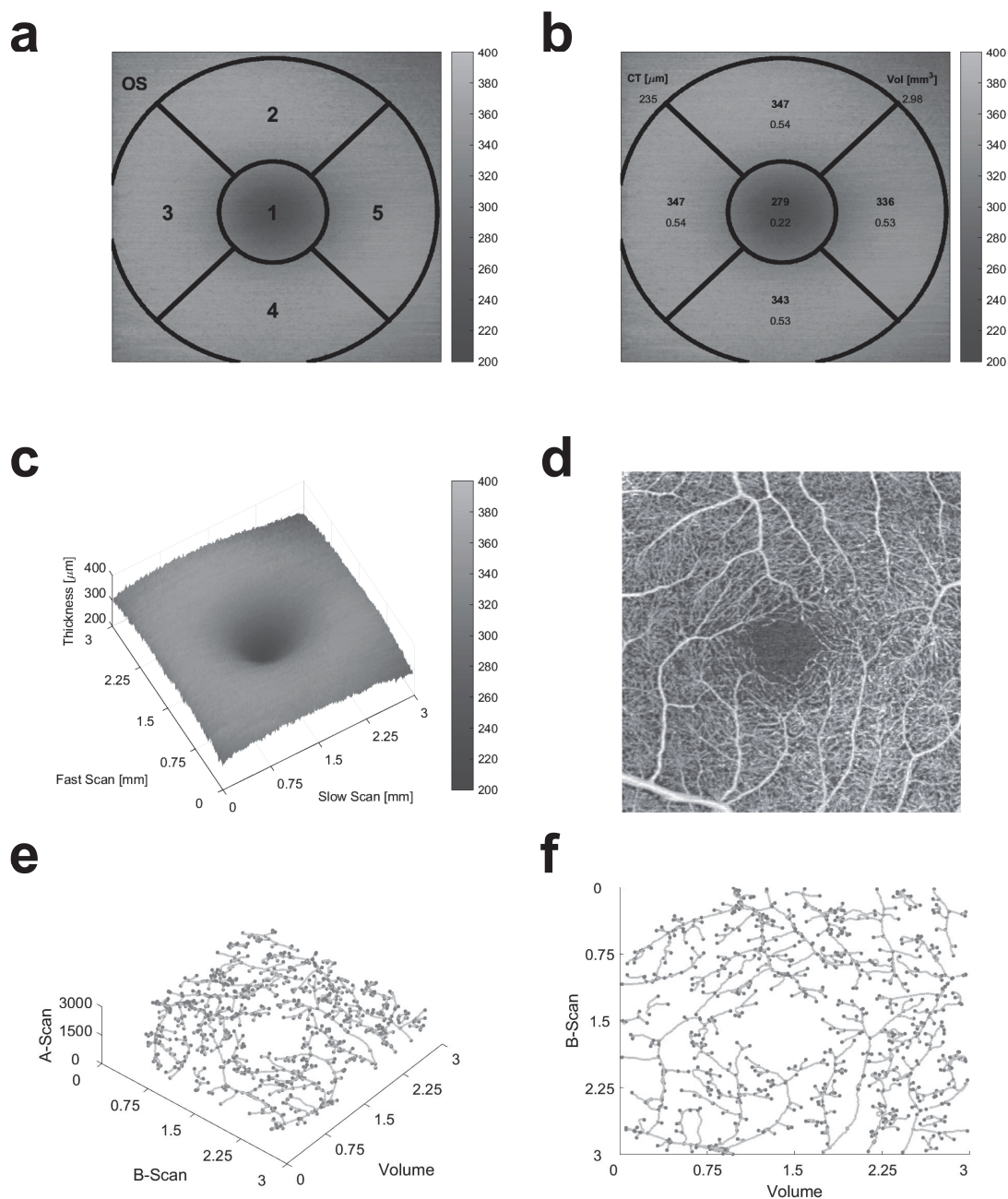
Figure D-2 Retinal thickness and volume measurements and RCP network graph for a control subject. (a) Numbered EDTRS subfields and grid over thickness map. (b) Retinal thickness and volume measurements for each subfield and overall. (c) Angled thickness map. (d) OCTA en-face image (e) Angled RCP network graph. (f) En-face view of RCP network graph.
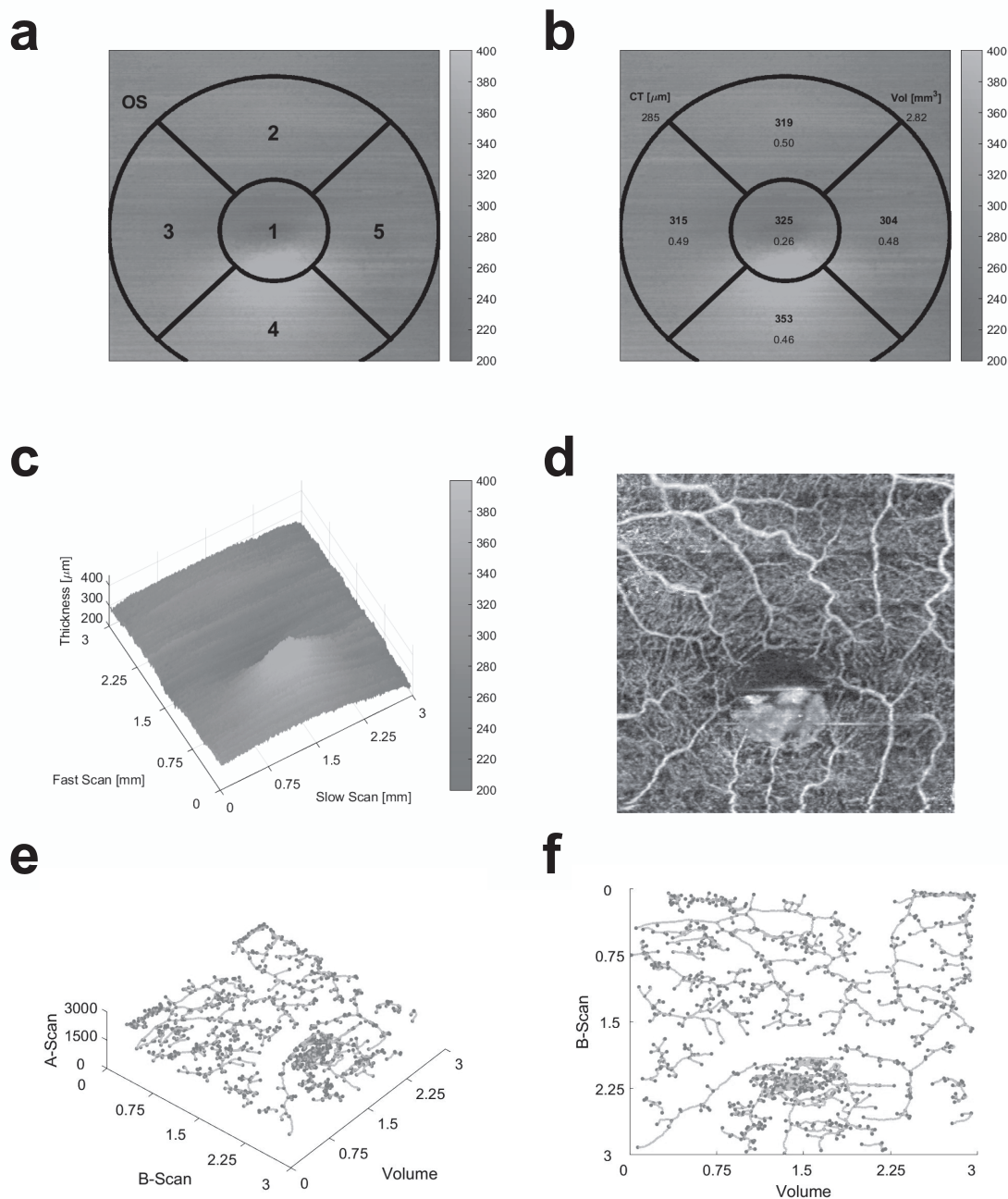
Figure D-3 Retinal thickness and volume measurements and RCP network graph for a neovascular AMD subject. (a) Numbered EDTRS subfields and grid over thickness map. (b) Retinal thickness and volume measurements for each subfield and overall. (c) Angled thickness map. (d) OCTA en-face image (e) Angled RCP network graph. (f) En-face view of RCP network graph.

APPENDIX E – DRUSEN SEGMENTATION METHODS VALIDATION
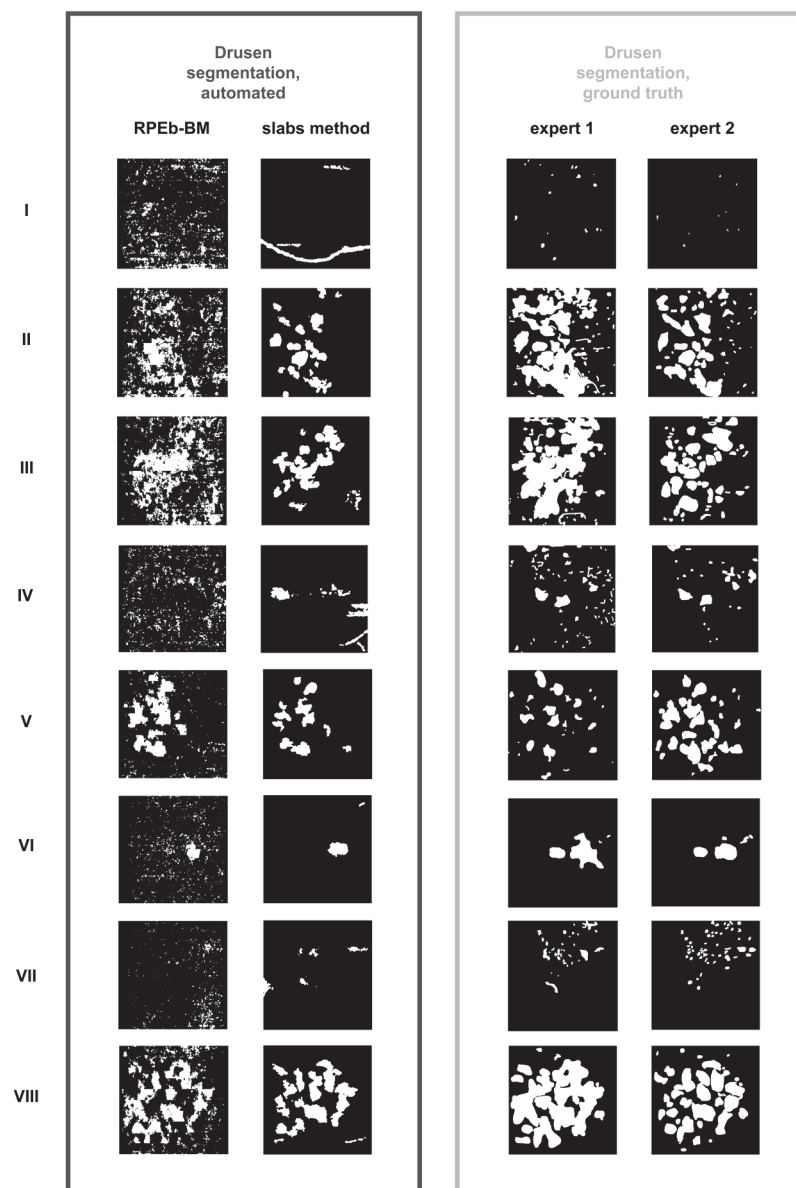
Figure E-1 Comparison of drusen segmentation masks generated through the automated drusen segmentation methods (dark grey frame; RPEb-BM and slabs method) and expert segmentations (light grey frame; expert 1 and expert 2) from aggregated selected C-scan ground truth segmentations.

Table E-1 Performance evaluation for RPEb-BM and en face drusen segmentation methods.

Method and expert	Number of images	Pixel-based results			
		Sensitivity (%)	Specificity (%)	Jaccard index	Dice coefficient
RPEb-BM method, expert 1	8	33.56	88.25	0.205	0.312
RPEb-BM method, expert 2	8	35.96	86.94	0.207	0.312
En face method, expert 1	8	31.64	97.76	0.249	0.372
En face method, expert 2	8	37.12	97.56	0.316	0.438

Table E-2 RPEb-BM drusen segmentation method, expert 1 AMD performance results.

id	sensitivity	specificity	jaccard	dice
1	24.05	81.69	0.011	0.022
2	40.16	82.71	0.292	0.451
3	47.74	83.12	0.348	0.517
4	5.69	91.56	0.040	0.077
5	63.55	82.80	0.251	0.401
6	31.46	96.00	0.203	0.337
7	2.50	98.90	0.028	0.054
8	53.31	89.22	0.468	0.638

Table E-3 RPEb-BM drusen segmentation method, expert 2 AMD performance results.

id	sensitivity	specificity	jaccard	dice
1	29.65	81.67	0.004	0.008
2	44.89	78.40	0.243	0.391
3	48.61	75.20	0.258	0.410
4	3.40	91.55	0.023	0.046
5	59.25	90.20	0.421	0.592
6	37.40	95.87	0.195	0.326
7	1.95	98.89	0.044	0.085
8	62.55	83.75	0.467	0.636

APPENDIX F – EXTENDED CLASSIFICATION VALIDATION

Table F-1 RF bands classification leave-one-out validation results.

id	sensitivity	specificity	precision	accuracy	F1
1	0.890		1.000	0.890	0.942
2-3	1.000		1.000	1.000	1.000
4	0.592		1.000	0.592	0.743
5	0.995		1.000	0.995	0.997
6	0.837		1.000	0.837	0.911
7	0.380		1.000	0.380	0.551
8	0.140		1.000	0.140	0.246
9	0.212		1.000	0.212	0.349
10	1.000		1.000	1.000	1.000
11-12		0.728	0.000	0.728	
13-14		0.999	0.000	0.999	
15		0.943	0.000	0.943	
16-17		0.028	0.000	0.028	
18-19		0.999	0.000	0.999	
20-21		0.988	0.000	0.988	
22		0.778	0.000	0.778	
per eye	70.00	83.33	77.78	77.27	73.68

Table F-2 RPEb-BM drusen segmentation method AMD area results.

id	totalArea	region1	region2	region3	region4	region5
1	1.080	0.093	0.226	0.204	0.217	0.160
2	2.185	0.323	0.574	0.275	0.484	0.166
3	2.755	0.276	0.613	0.526	0.647	0.225
4	0.814	0.077	0.129	0.167	0.123	0.107
5	1.423	0.216	0.362	0.050	0.279	0.318
6	1.414	0.114	0.244	0.290	0.284	0.183
7	0.522	0.059	0.071	0.129	0.155	0.025
8	0.304	0.011	0.017	0.141	0.027	0.005
9	0.469	0.028	0.056	0.172	0.123	0.013
10	2.329	0.276	0.413	0.273	0.571	0.492

Table F-3 Choriocapillaris flow voids AMD FV10000 results.

id	FV10000	region1	region2	region3	region4	region5
1	0.073	0.190	0.040	0.033	0.120	0.000
2	0.241	0.453	0.079	0.080	0.235	0.175
3	0.208	0.065	0.144	0.117	0.148	0.381
4	0.249	0.050	0.159	0.341	0.235	0.355
5	0.289	0.423	0.315	0.096	0.167	0.494
6	0.039	0.000	0.000	0.073	0.055	0.038
7	0.140	0.296	0.035	0.189	0.060	0.165
8	0.161	0.256	0.141	0.162	0.106	0.102
9	0.064	0.000	0.042	0.164	0.091	0.000
10	0.490	0.696	0.169	0.393	0.427	0.715

Table F-4 RPEb-BM drusen segmentation method control area results.

id	totalArea	region1	region2	region3	region4	region5
1	0.291	0.012	0.032	0.085	0.024	0.020
2	0.491	0.082	0.093	0.027	0.114	0.124
3	0.171	0.014	0.019	0.046	0.030	0.021
4	0.342	0.034	0.055	0.043	0.063	0.090
5	0.166	0.010	0.014	0.081	0.014	0.006
6	0.298	0.034	0.061	0.037	0.056	0.052
7	0.431	0.051	0.085	0.095	0.070	0.051
8	0.346	0.040	0.068	0.086	0.059	0.030
9	0.391	0.047	0.083	0.052	0.072	0.094
10	0.184	0.008	0.026	0.065	0.032	0.008
11	0.140	0.005	0.017	0.011	0.024	0.065
12	0.417	0.015	0.046	0.034	0.094	0.144

Table F-5 Choriocapillaris flow voids control FV10000 results.

id	FV10000	region1	region2	region3	region4	region5
1	0.078	0.200	0.097	0.086	0.041	0.085
2	0.073	0.201	0.000	0.128	0.047	0.044
3	0.010	0.087	0.000	0.000	0.000	0.000
4	0.074	0.142	0.000	0.044	0.082	0.162
5	0.046	0.279	0.039	0.000	0.042	0.000
6	0.213	0.323	0.173	0.177	0.248	0.264
7	0.316	0.598	0.147	0.186	0.287	0.416
8	0.000	0.000	0.000	0.000	0.000	0.000
9	0.000	0.000	0.000	0.000	0.000	0.000
10	0.016	0.000	0.000	0.000	0.000	0.000
11	0.027	0.000	0.000	0.042	0.000	0.104
12	0.032	0.099	0.000	0.083	0.000	0.000